NATIONAL TECHNICAL UNIVERSITY
OF ATHENS
School of Civil Engineering
Institute of Steel Structures

Development of a Joint without Eccentricity for Scissor-Type Deployable Structures

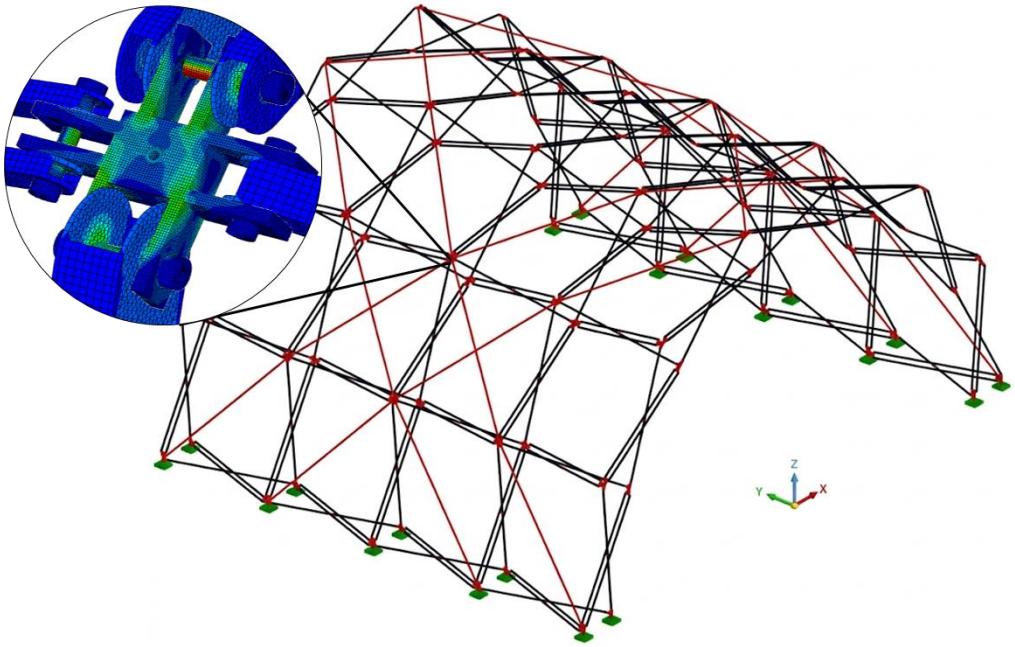

Graduate Thesis

Emmanouil-Ioannis Daktylidis

EMK ME 2026 6

Supervisor: Charis Gantes, Professor NTUA
Co-Supervisor: Georgios Pantazis, PhD Student

Athens, June 2026

ΕΘΝΙΚΟ ΜΕΤΣΟΒΙΟ ΠΟΛΥΤΕΧΝΕΙΟ
Σχολή Πολιτικών Μηχανικών
Εργαστήριο Μεταλλικών Κατασκευών

ΣΧΕΔΙΑΣΜΟΣ ΕΝΟΣ ΚΟΜΒΟΥ ΧΩΡΙΣ ΕΚΚΕΝΤΡΟΤΗΤΕΣ ΓΙΑ ΨΑΛΙΔΩΤΕΣ ΠΤΥΣΣΟΜΕΝΕΣ ΚΑΤΑΣΚΕΥΕΣ

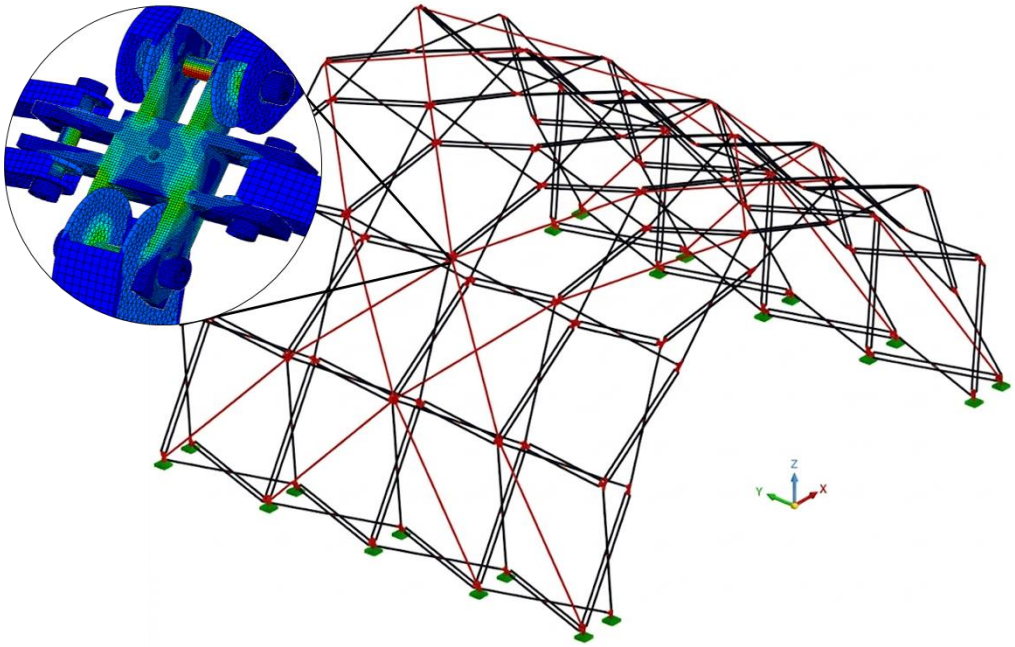

Μεταπτυχιακή Εργασία

Εμμανουήλ-Ιωάννη Δακτυλίδη

ΕΜΚ ΜΕ 2026 6

Επιβλέπων: Χάρης Γαντές, Καθηγητής Ε.Μ.Π
Συνεπιβλέπων: Γεώργιος Πανταζής, Υ.Δ.

Αθήνα, Ιούνιος 2026

Εμμανουήλ-Ιωάννης Δακτυλίδης (2026)

Σχεδιασμός Ενός Κόμβου Χωρίς Εκκεντρότητες για Ψαλιδωτές Πτυσσόμενες Κατασκευές

Μεταπτυχιακή Εργασία ΕΜΚ ΜΕ 2026 6

Εργαστήριο Μεταλλικών Κατασκευών, Εθνικό Μετσόβιο Πολυτεχνείο, Αθήνα.

Emmanouil-Ioannis Daktylidis (2026)

Development of a Joint without Eccentricity for Scissor-Type Deployable Structures

Graduate Thesis EMK ME 2026 6

Institute of Steel Structures, National Technical University of Athens, Greece

Acknowledgements

This thesis concludes my obligations towards the graduate degree. By concluding this second stage of my academic course, I would like to sincerely thank my supervisor, Professor Charis Gantes, for his valuable guidance throughout this journey, his insightful remarks during the development of this thesis, and for broadening my horizons. In the same way, I would like to sincerely thank PhD student Georgios Pantazis for entrusting me with his work on deployable structures and for his patience in helping me resolve technical issues that would otherwise have made the development of this thesis impossible.

In conclusion, I would like to express my gratitude towards my family who have always supported me in every choice I have made and will make.

Στην οικογένειά μου,

ΕΘΝΙΚΟ ΜΕΤΣΟΒΙΟ ΠΟΛΥΤΕΧΝΕΙΟ
ΣΧΟΛΗ ΠΟΛΙΤΙΚΩΝ ΜΗΧΑΝΙΚΩΝ
ΕΡΓΑΣΤΗΡΙΟ ΜΕΤΑΛΛΙΚΩΝ ΚΑΤΑΣΚΕΥΩΝ

ΜΕΤΑΠΤΥΧΙΑΚΗ ΕΡΓΑΣΙΑ
ΕΜΚ ΜΕ 2026 6

Σχεδιασμός Ενός Κόμβου Χωρίς Εκκεντρότητες για Ψαλιδωτές Πτυσσόμενες Κατασκευές

Εμμανουήλ-Ιωάννης Δακτυλίδης

Επιβλέπων: Χάρης Γαντές, Καθηγητής ΕΜΠ
Συνεπιβλέπων: Γεώργιος Πανταζής, Υ.Δ.

ΠΕΡΙΛΗΨΗ

Ένα από τα πιο καίρια ζητήματα κατά τον σχεδιασμό και την ανάλυση πτυσσόμενων κατασκευών είναι οι κόμβοι τους. Κατά τον σχεδιασμό των ψαλιδωτών στοιχείων από τα οποία θα αποτελούνται κατασκευές όπως πτυσσόμενα στέγαστρα ή θόλοι, η δημιουργία του κόμβου που θα συνδέει τα επιμέρους μέλη επιβάλλει την παρουσία εκκεντροτήτων του άξονα των μελών ως προς το κέντρο βάρους του κόμβου. Αυτές οι εκκεντρότητες συχνά επηρεάζουν τη δομική συμπεριφορά των κατασκευών.

Η παρούσα εργασία επιχειρεί τη δημιουργία ενός κόμβου σύνδεσης των επιμέρους μελών χωρίς την παρουσία εκκεντροτήτων. Αυτό επιτυγχάνεται μέσω της θεώρησης «διπλών» ψαλιδωτών στοιχείων, της προσθήκης δηλαδή ενός μέλους στα ήδη δύο που συνθέτουν ένα ψαλιδωτό στοιχείο. Με αυτόν τον τρόπο επιτυγχάνεται η απαλοιφή των εκκεντροτήτων κατά τη γεωμετρική σύλληψη του κόμβου. Η ίδια η γεωμετρία του κόμβου είναι απόλυτα εξαρτημένη από τη γεωμετρία των διατομών των συνδεόμενων μελών, για αυτόν τον λόγο ακολουθείται μια μεθοδολογία με σκοπό την εύρεση των βέλτιστων κοίλων διατομών αλουμινίου που θα χρησιμοποιηθούν στη κατασκευή.

Αρχικά γίνεται η θεώρηση άκαμπτων στοιχείων για τους κόμβους και πεπερασμένων στοιχείων δοκού για τα μέλη και διενεργούνται γραμμικές αναλύσεις εφαρμόζοντας στην κατασκευή μόνιμα φορτία και φορτία χιονιού και ανεμοπιέσεων σύμφωνα με τους ισχύοντες κανονισμούς. Η οριστικοποίηση των διατομών επιτυγχάνεται με δυό τρόπους. Σε επόμενη φάση διενεργούνται μη-γραμμικές αναλύσεις γεωμετρίας (GNA) με σκοπό τη σύγκριση των εντατικών μεγεθών με αυτά της γραμμικής ανάλυσης. Στη συνέχεια, πραγματοποιούνται μη γραμμικές αναλύσεις γεωμετρίας με ατέλειες (GNIA) χρησιμοποιώντας σαν σχήμα αρχικών ατελειών τις κατάλληλες ιδιομορφές λυγισμού από τις γραμμικές αναλύσεις λυγισμού που προηγήθηκαν. Οι διατομές οριστικοποιούνται μέσω της σύγκρισης των αποτελεσμάτων, με τον σχεδιασμό μέσω του προβλεπόμενου κανονιστικού πλαισίου του Ευρωκώδικα 9 για διατομές αλουμινίου. Με την οριστικοποίηση των διατομών οριστικοποιείται και η γεωμετρία του κόμβου και γίνεται αναθεώρηση του φορτίου τους στην κατασκευή.

Τέλος διενεργείται προσομοίωση του κόμβου και των μελών με χρήση χωρικών πεπερασμένων στοιχείων. Από την ανάλυση αυτή εξάγονται συμπεράσματα για τις αναπτυσσόμενες τάσεις στον κόμβο και τα μέλη, παρέχοντας πολύτιμα δεδομένα για τον σχεδιασμό μιας πιθανής πειραματικής διάταξης.

NATIONAL TECHNICAL UNIVERSITY OF ATHENS
SCHOOL OF CIVIL ENGINEERING
INSTITUTE OF STEEL STRUCTURES

GRADUATE THESIS
EMK ME 2026 6

Development of a Joint without Eccentricity for Scissor-Type Deployable Structures

Emmanouil-Ioannis Daktylidis

Supervisor: Charis Gantes, Professor NTUA
Co-supervisor: Georgios Pantazis, PhD Student

ABSTRACT

One of the most critical aspects in the design and analysis of deployable structures is the configuration of their joints. In the design of scissor-like elements that form deployable structures, such as shelters or domes, the development of joints connecting the individual members typically introduces eccentricities of the member axes with respect to the centroid of the joints. These eccentricities often influence the structural behaviour under loading conditions such as wind or snow.

The present study aims to develop a joint capable of accommodating the connected members without introducing eccentricities. This is achieved through the adoption of double scissor-like elements, involving the addition of an extra member to the conventional two-member scissor configuration. In this way, eccentricities are eliminated during the geometric configuration of the joint.

The geometry of the joint is directly dependent on the cross-sectional geometry of the connected members. Therefore, a methodology is followed to determine the optimal hollow aluminium cross-sections to be used in the structure. Initially, rigid elements are assumed for the joints and linear beam finite elements for the members. Linear analyses are then performed by applying the assumed joint loads, as well as snow and wind loads, according to the relevant design standards.

The finalisation of the cross-sections is achieved through two approaches. First, geometrically nonlinear analyses (GNA) are performed to compare the internal forces with those obtained from linear analysis. Subsequently, geometrically nonlinear analyses with imperfections (GNIA) are conducted, using initial imperfection shapes derived from the buckling mode shapes obtained through preceding linear buckling analyses. The final cross-sections are determined through comparison of the results and verification according to the provisions of Eurocode 9 for aluminium structures. Once the cross-sections are finalised, the geometry of the joint is also determined, and the corresponding joint loads in the structure are revised accordingly.

Finally, a simulation of the joint and the members is conducted using solid finite elements. This analysis yields conclusions regarding the developed stresses of the joint and the elements, providing valuable insight for the design of a potential experimental setup.

Contents

1 DEPLOYABLE STRUCTURES

1.1 General

Deployable structures consist of lightweight structures that can rapidly alter their shape through a controllable process governed by their geometry and the arrangement of their members and joints. This shape transformation can be achieved through joint mechanisms or other innovative solutions that integrate controllable kinematics or automatic control processes. Their geometry is defined in two basic stages, regardless of their category. The first stage consists of the so-called closed form, which is the transportable, non-deployed form that helps the structure be transferred or stored until deployment. The second stage consists of the so-called open form, which is the partial or full deployment, depending on the category of the deployable structure. That stage is considered the usable stage for the deployable structure. During the structure's lifetime, the stages can be altered multiple times.

The categorization of the deployable structures is based simply on their structural system as follows [1]:

- Pantographic deployable structures
- Membrane deployable structures
- Pneumatic deployable structures
- Tensegrity deployable structures

This graduate thesis investigates the scissor-like element deployable structures and the definition of an optimal node without eccentricity for a deployable shelter. This category of deployable structures is ideal for emergency situations or other circumstances that demand rapid housing, sheltering, or even shading of a space. These structures offer advantages such as the transportation ability relative to their decreased size during the closed form, as well as the rapid assembly and disassembly ability. Their closed form volume capacity, when compared to the open form, increases their ability to shelter a maximum of space with the minimum logistical need. Their disadvantage is simply their analysis and design process. Their complexity demands a non-linear analysis approach to the structure in order to be as close to reality as possible. These structures can be considered highly nonlinear, resulting in major uncertainties regarding their behavior under complex loading.

1.2 Pantographic deployable structures

Pantographic deployable structures are the most common type of deployable structures found in everyday applications and have multiple uses. They consist of repetitive frames of scissor-like elements or SLEs that create frames which with their place create the structure. Their main characteristic is their ability to alter their volume in a very rapid way by changing their shape [1].

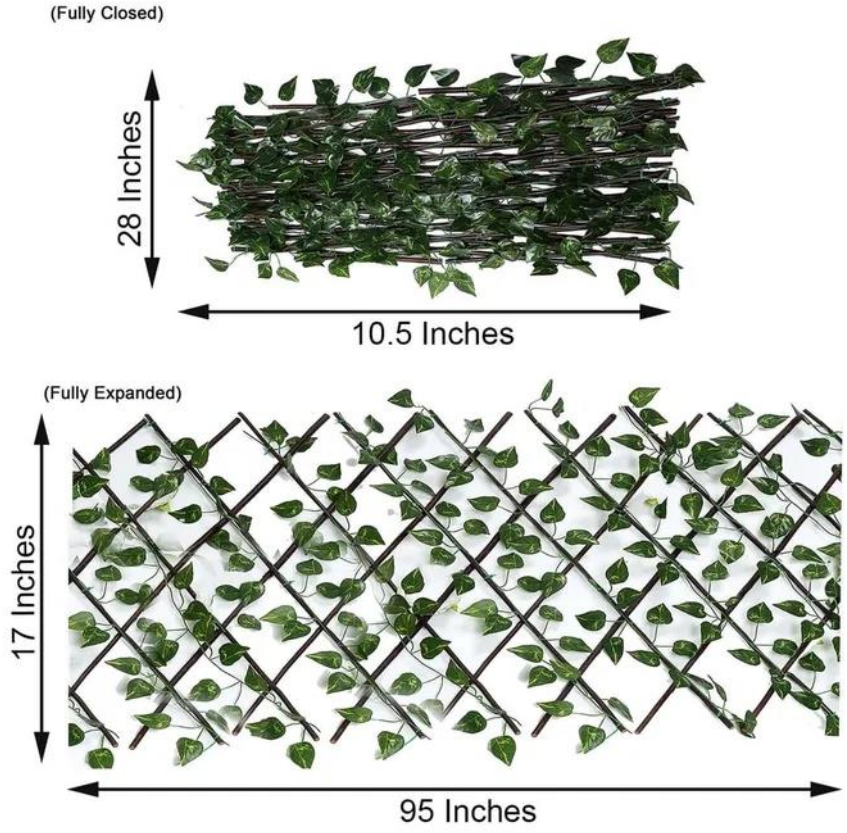

Figure 1. Accordion-style lattice pantographic deployable structure [2].

The expansion of a pantographic deployable structure can easily happen in a two-dimensional space. This means that the simple pantograph can be repeated linearly into each component. The more pantographs used for the closed from the larger the area of the plane covered in the open form. For civil engineering applications, though, there is the need to cover a three dimentional space. For this reason, the pantographic repetition of the scissor-like elements (SLEs) needs to be expanded into the three-dimensional space. The final geometry will define the direction in which the pantographs will be repeated. The ultimate shape will be achieved through the connection of the SLEs, as well as the final curvature of the structure (single, double, or flat), and the dimensions of the grid. Fig.2 shows the possible outlays and combinations of the parameters mentioned in closed and open form.

1.2.1 Scissor-Like Elements in Deployable Structures

Depending on the kind of their fundamental unit, deployable scissor structures can be categorised as translational, polar, or angulated. The core structural element of any deployable scissor grid is a Scissor-Like Element (SLE). An SLE is made up of two bars that are hinged together and can move inside the

unit's plane. Only one axis can be rotated by an SLE. The angulated unit is made up of two angled bars, while the translational and polar units are made up of two straight bars.

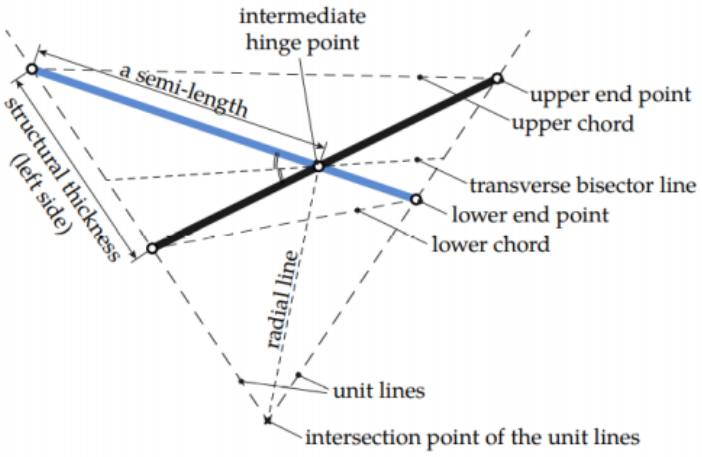

Figure 2. General form of the Scissor-like Element (SLE) [3].

Each scissor unit may behave differently mechanically depending on the shape of the bars and the location of the intermediate hinge. This gives the designer the freedom to create several general shapes in a deployable scissor structure based on the required kinematic behaviour during deployment, as well as the geometric specifications of the folded and deployed configurations. The most important factor influencing how the scissor element behaves is the location of the intermediate hinge. It calculates the lengths of the two segments (semi-lengths) into which each bar is split and, as a result, the degree of convergence of the unit lines, which are imaginary lines that connect the end nodes of the two bars.

The element is categorised as a translational scissor unit when these unit lines stay parallel during each deployment stage. This type of scissor mechanism is the most basic. The intermediate hinge in translational units is positioned to ensure that the two bars' semi-length ratios are equivalent. Because of this, the element's movement results in a pure translational expansion, with no radial convergence and the end nodes moving along parallel trajectories. During expansion, structures made out of translational units usually produce planar or cylindrical deployable grids with consistent geometry and uniform motion.

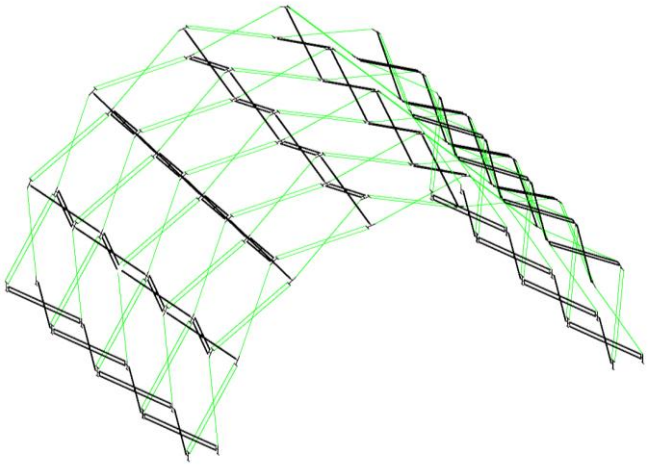

Figure 3. Example of translational scissor-like elements (SLEs) in black, forming a deployable shelter.

On the other hand, the element is categorised as a polar scissor unit when the axes joining the end nodes converge toward a common point during deployment. In this instance, uneven semi-lengths are produced by the intermediate hinge's asymmetrical placement along the bars. As the structure deploys, the unit lines rotate and converge toward a centre of curvature as a result of this geometric asymmetry. Therefore, polar scissor units create radial or dome-like topologies, making it possible to create curved deployable surfaces like spherical grids or circular roofs. What essentially separates polar units from translational ones and enables them to produce non-linear, centrally directed geometries is the convergence of the unit lines.

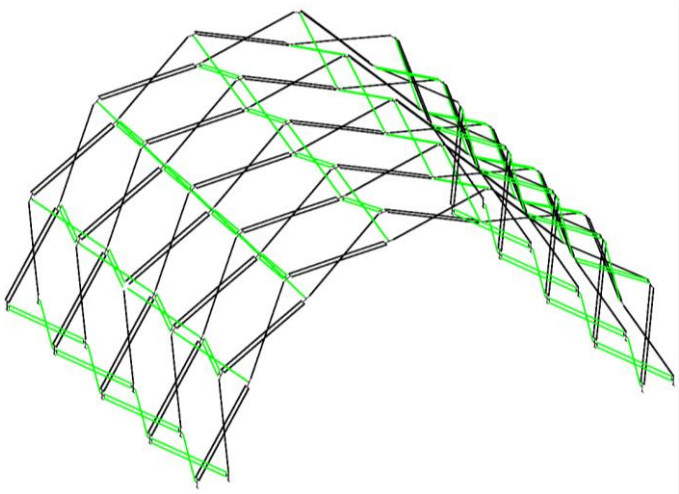

Figure 4. Example of polar scissor-like elements (SLEs) in black, forming a deployable shelter.

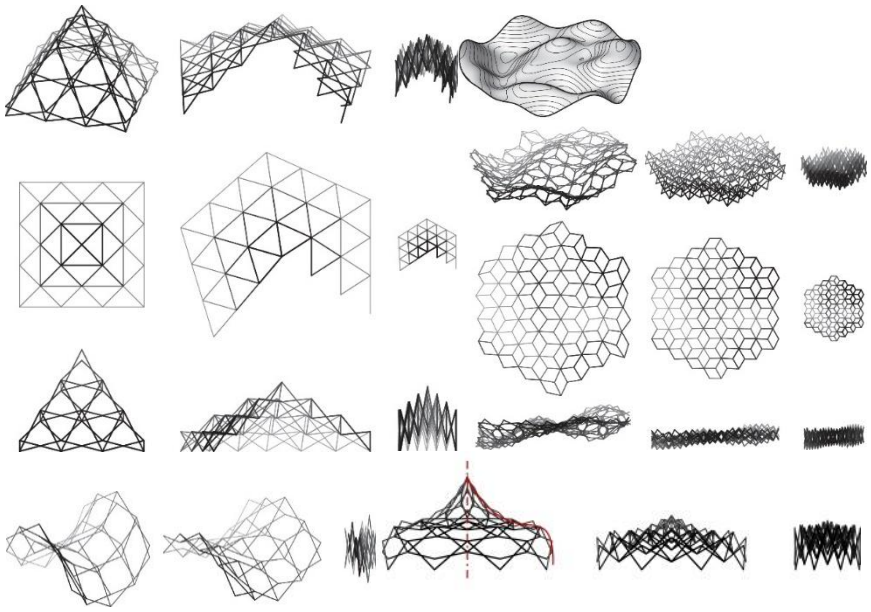

Figure 5. Possible outlays of pantographic deployable structures in closed and open form [4].

1.2.2 Earth-Based Pantographic Deployable Structures

As mentioned before, most applications of deployable structures consist of emergency sheltering or temporary applications in general. However, in some cases, deployable structures have been applied instead of a temporary steel structure as a retractable roof, able to cover large-span areas such as sports centres. One of the most notable applications is the San Pablo retractable roof in Seville, Spain, as shown in Fig.6 which covers the swimming pool, protecting the facilities from adverse weather conditions and other external factors that may have prevented their use.

Figure 6. San Pablo retractable roof in Seville, Spain in its closed and open form [5].

Another notable application of deployable structure is the temporary use of them in exchibitions or outdoor activites. These structures can either be very simple and small scale but also complex and large scale. The most common products consist of simple tents for example as shown in Fig. 7.

Figure 7. Deployable motorsport tent for outdoor shading [6].

1.2.3 Deployable structures applied in space

The application in the space of pantographic deployable structures was created through the need for a fundamental constraint of rocketry. In order to transfer payload into orbit, launch vehicles impose strict limits on volume and mass, yet once in orbit, spacecraft often require structures far larger than any rocket fairing can accommodate. The first attempt at conceiving deployable structures in space was during the 1960s, when engineers at agencies such as NASA and the European Space Research Organisation (now European Space Agency) began making experiments with retractable booms and articulated trusses for simple scientific instruments or antennas of the first satellites. The goal was to provide a packaging solution as an engineering necessity rather than architectural innovation. The initial inspiration came from mechanical linkage principles such as terrestrial cranes, umbrellas, and simple scissor lifts, aiming for compact stowage and reliable deployment in zero gravity. This is the stage where the idea of a pantographic expansion was more of a clever mechanical trick rather than a distinct structural typology for unfolding space hardware.

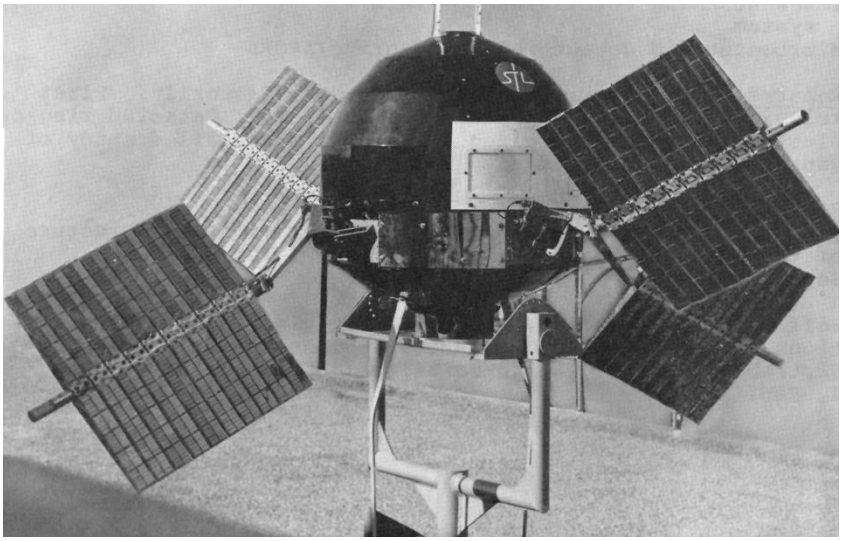

Figure 8. Explorer 6 satellite with its solar panels extended (NASA) [7].

By the early 1970s, in missions such as ATS-6 in 1974, the deployable antennas had been significantly developed. Once in orbit, its huge deployable reflector proved that articulated rib and truss structures could reliably stretch to many meters in diameter. Because of this accomplishment, deployable structures were seen as mission-enabling technologies rather than just small add-ons. Pantographic and articulated systems started to be viewed by engineers as scalable frameworks that could handle payloads for high-precision communication. In satellite design, the concept of regulated geometric expansion, where links changed from a tight bundle into a stable structural surface, became crucial.

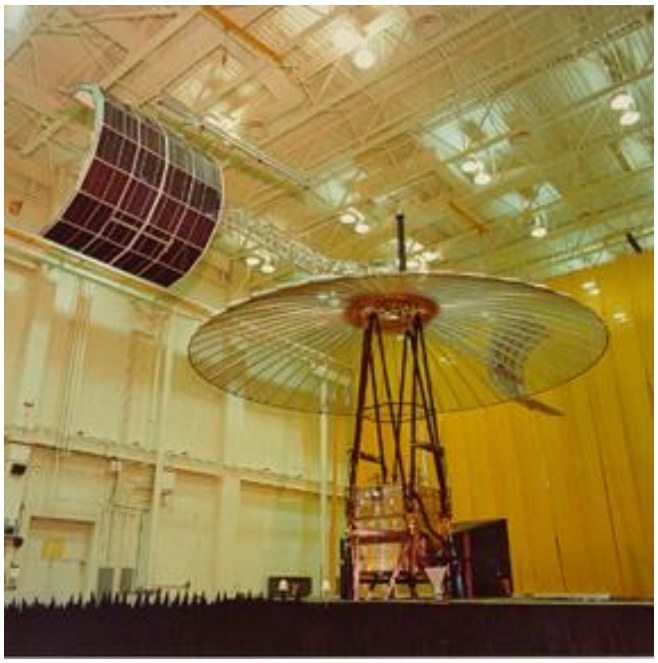

Figure 9. ATS-6 during radio-frequency tests (NASA) [8].

An important turning point was reached in the 1980s with the invention of articulated deployable masts, such as the ADAM mast flown on Space Shuttle flights. The stiffness and alignment of these scissor-like truss systems would allow them to span considerable distances. Further, pantographic systems were viewed as structural backbones that could support sensors located far from spaceship bodies, rather than merely deployable devices. During this time, long, thin deployable booms gained trust, and it was shown that scissor-based kinematics could offer rigidity and compactness through locking mechanisms after deployment.

Large-scale applications like the 60-meter mast flown during Space Shuttle Endeavour's Shuttle Radar Topography Mission and the International Space Station's growing truss assemblies in the 1990s strengthened this faith. Deployable systems were included in significant international programs and were no longer considered experimental. Pantographic and articulated structures were seen by engineers as dependable infrastructure in orbit that can support large solar arrays and construct prolonged measuring baselines.

Figure 10. SRTM (Shuttle Radar Topography Mission) mast fully deployed (JPL) [9].

By the 2000s, deployable antenna systems might achieve previously unheard-of scales, such as 20 meters and beyond, thanks to missions like ETS-VIII. At this point, the idea was about precision, surface accuracy, and lightweight composite construction rather than just folding and unfolding. A sophisticated grasp of geometry, rigidity, and orbital dynamics was demonstrated by the frequent combination of pantographic logic with mesh reflectors and cutting-edge materials.

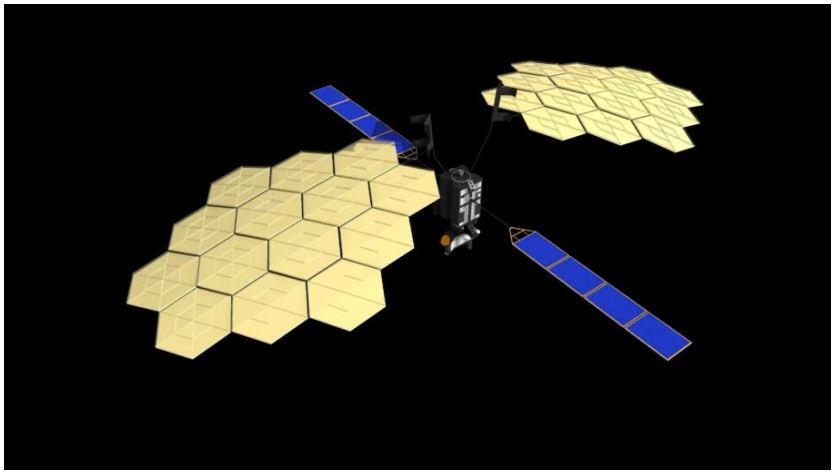

Figure 11. Engineering Test Satellite VIII "KIKU No.8" (ETS-VIII), NASDA [10].

Between 2000 and 2010, engineering work at NASA's Jet Propulsion Laboratory (JPL) and research on large-scale deployable space structures at the California Institute of Technology's Graduate Aerospace Laboratories (GALCIT), particularly under the guidance of Prof. Sergio Pellegrino, established crucial foundational research and applied technologies in ultra-lightweight, precision masts and mechanisms for space applications.

The mechanics of lightweight deployable systems, namely the issues of packaging, deployment, form control, and stability for space structures, were the main emphasis of Professor Sergio Pellegrino and associates at GALCIT. To comprehend how thin-shell, coiled, and linkage-based structures can be compactly stowed and reliably deployed in orbit with minimal mass, a crucial requirement for missions such as space solar power platforms and space telescopes, this research investigated innovative deployable concepts and analytical techniques over the course of the decade. In order to better understand deployment kinematics and dynamics, Prof. Pellegrino's work produced structured knowledge of deployable mechanisms and structural dynamics for precision space applications, as well as analytical frameworks and prototypes that may scale to tens of meters for future missions.

At the same time, JPL's technical teams were creating and testing deployable mast technologies for use in space science missions. The NuSTAR X-ray observatory's deployable boom, which extended a lightweight, stowed mast to its full length in orbit to give the telescope's large focal length necessary for high-energy X-ray imaging, is a notable example. Even though NuSTAR was launched in 2012, Caltech and JPL engineers worked together to develop the design, analysis, and precision requirements for its deployable mast in the late 2000s. This endeavour was a reflection of JPL's continuous efforts to develop scalable, high-precision deployable hardware for space astronomy missions and other scientific payloads that need extended structural baselines once in orbit.

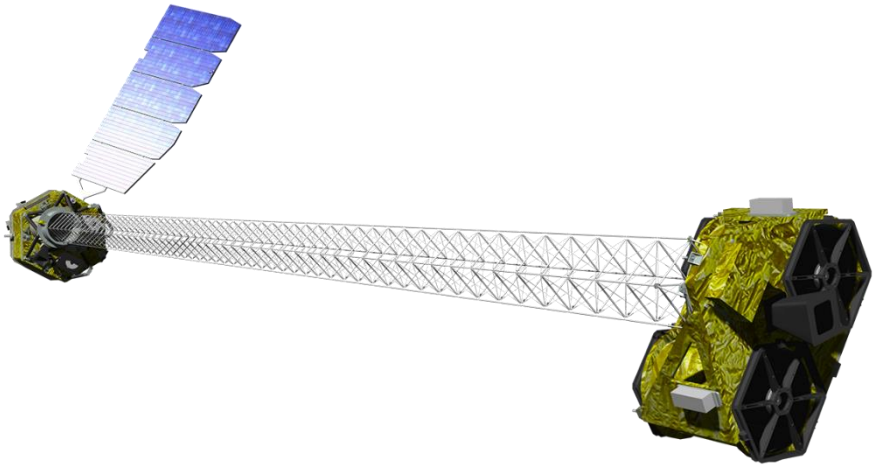

Figure 12. Nuclear Spectroscopic Telescope Array, or NuSTAR (JPL) [11].

Decades of deployable-structure research culminated in complex missions like the James Webb Space Telescope in the 2010s and 2020s. Its mechanics are based more on segmented unfolding and hinged trusses than on pure scissor grids, but its conceptual roots are in early pantographic concepts: structures that drastically change from a small launch configuration to an expansive operational form. These days, pantographic deployable systems are seen as crucial facilitators of large-scale space architecture, connecting geometry, materials science, and precision engineering in the special environment of orbit, rather than merely mechanical solutions to packing limitations.

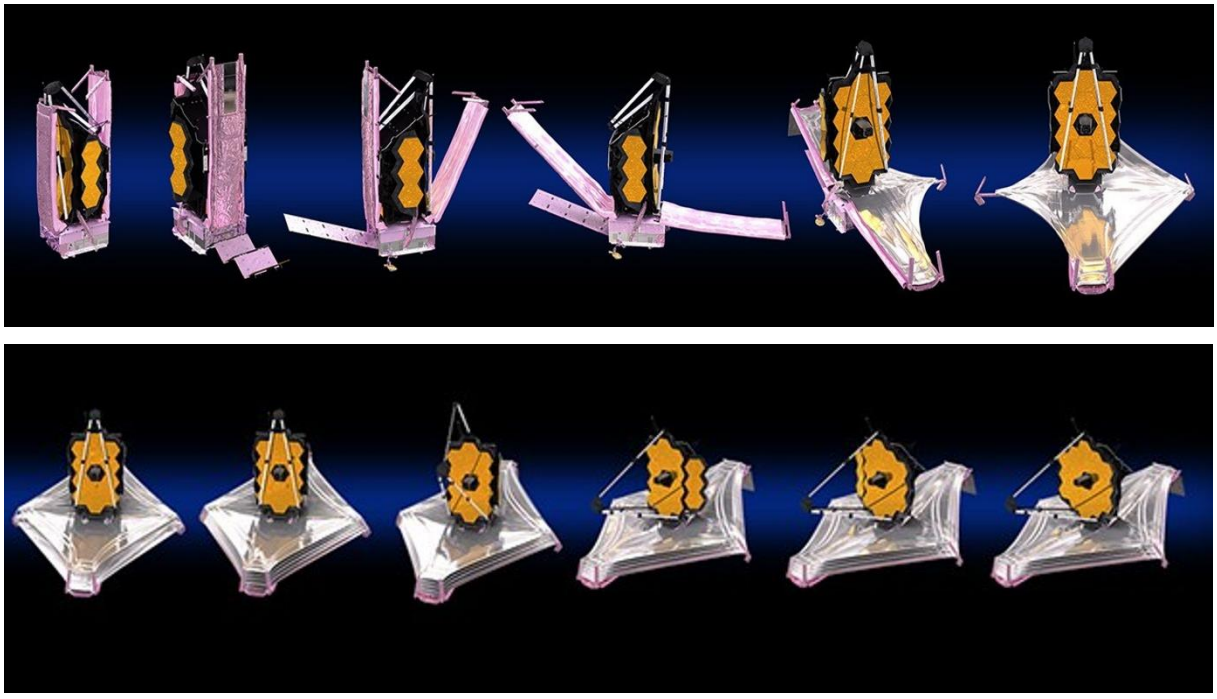

Figure 13. Deployment phases of James Webb Space Telescope (NASA) [12].

1.3 Joints in Deployable Structures

One of the major issues in assembling and constructing deployable structures is the joints. For a certain configuration to operate, the elements of a deployable structure need to operate with certain degrees of freedom. These will be provided to the elements from the joints, which will restrain or free certain movements. The development of these joints is one of the major challenges in engineering. Historically, the most commonly used joint was the hinged joint because it is the simplest one of all. It allows the rotation about a single axis, providing a controlled deployment motion, thus releasing the rotational degree of freedom. To provide the necessary stiffness on the fully deployed phase, the joint can sustain a self-locking mechanism or other stiffening methods.

1.3.1 Classification of Joints in Deployable Structures

Specialised joints are crucial for deployable constructions because they enable significant relative movement between structural elements while maintaining connectivity and load transfer. Depending on the degrees of freedom they offer, joints can be broadly divided into three types of articulated systems: revolute, spherical, and universal [1] . Revolute joints, which are commonly employed at the intersections of bars to permit rotation about a single axis and simplify folding and unfolding, are the most prevalent connectors in scissor-type deployable constructions. Hub connections act worldwide as spherical joints at the nodes where several members converge, allowing rotations in several directions to adapt to geometric changes during deployment. When two rotational degrees of freedom are needed, universal joints can also be conceptually explored.

1.3.2 Hub and Connection Design Requirements

Because joints in deployable structures must support significant relative rotations while maintaining sufficient load transfer and geometric compatibility throughout the deployment process, their design is subject to strict kinematic and structural criteria [1]. Hubs serve as multi-member nodes that join multiple bars in articulated systems, including scissor-type deployable frameworks. They distribute weights applied from the outside as well as internal forces without adding undue restrictions that would prevent deployment. Enough rotational degrees of freedom must be provided, usually via revolute or pin-based connections, so that members can experience significant angular displacements with little resistance.

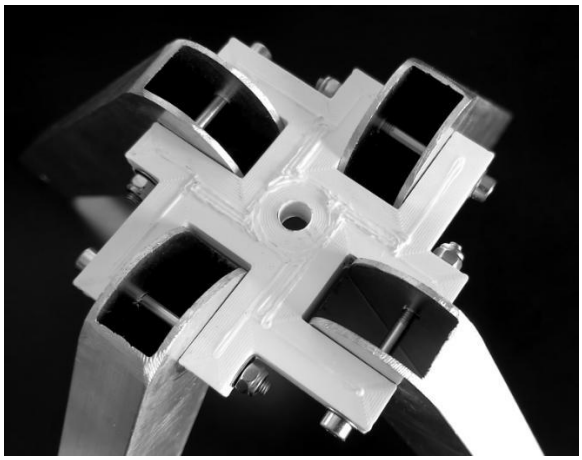

Figure 14. Example of a hub type joint [13].

Hub geometry must be set up to allow for compact packing of members in the folded configuration, in addition to kinematic functioning. This will prevent mechanical interference and guarantee that the bundle of parts stays well-organised during stowage. This calls for careful management of clearances, tolerances, and pin positioning in addition to taking member cross-sectional dimensions into account. Because excessive friction can greatly increase deployment forces and cause uneven motion or local binding, it is important to limit frictional effects at the interfaces of pins, bars, and hub slots through proper material selection, surface treatment, and lubrication.

From a structural perspective, connections must be strong and stiff enough to transfer bending moments, shear pressures, and axial forces in the deployed configuration while avoiding stress concentrations that could shorten fatigue life under repeated deployment cycles. The need to strike a compromise between the functional requirements to support massive rotations and the mechanical dependability, manufacturability, and assembly efficiency is reflected in the progression of hub designs toward simpler geometries. As a result, the precise layout of hubs and connections is essential to guaranteeing the deployable systems' overall performance, structural stability, and smooth kinematic behaviour.

1.3.3 Mechanical Behavior of Joints During Deployment

Since connections must support significant relative rotations and numerous motion cycles while preserving structural integrity, the mechanical behaviour of joints during deployment is crucial to the overall performance and dependability of deployable systems. The creation of frictional forces and resistive moments that affect the necessary deployment loads and the smoothness of motion is caused by the different contact conditions that pivotal and hinged joints encounter as components rotate in scissor-type systems and other articulated frameworks [14]. Geometric clearances and contact between pins, bars, and hub slots can cause nonlinear behaviour, especially close to folded configurations where transverse forces between components may rise noticeably.

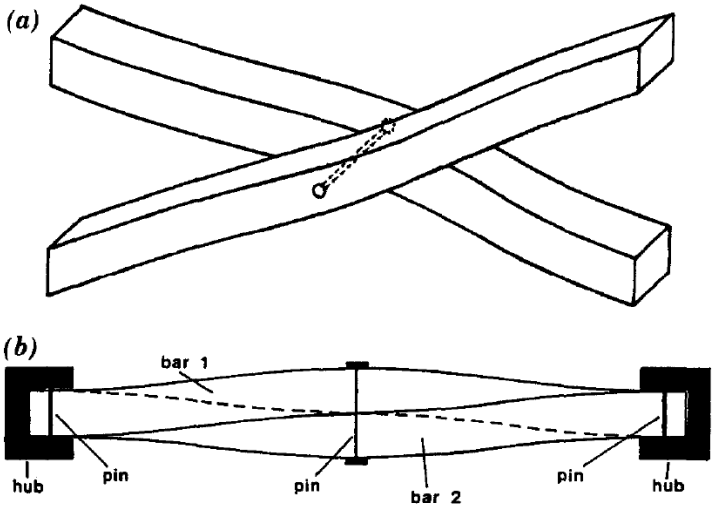

Figure 15. Scissor-like element with discrete member width illustrating bar contact and the geometric origin of friction during relative rotation [14].

Additionally, the global kinematic response is impacted by the interplay between member stiffness and joint flexibility, which may also be a factor in locking behaviour or snap-through. Because friction, local deformation, and possible misalignment can change load courses and add extra energy dissipation during deployment and disassembly, these aspects must be taken into account for an accurate

assessment of joint mechanics. Predicting deployment forces, guaranteeing stable operation, and avoiding problems like binding, excessive wear, or loss of synchronisation among structural components all depend on an understanding of the mechanical reaction of joints.

Since connections introduce nonlinearities related to large rotations, contact interactions, and frictional effects, accurate joint modelling is crucial for forecasting the kinematic response and structural behaviour of deployable systems. To capture the main motion of the mechanism, joints are frequently modelled as kinematic constraints with predetermined degrees of freedom in analytical and numerical simulations, such as spherical or revolute connections. More complex models, on the other hand, include friction, joint stiffness, and clearances to simulate the resistive moments that occur during folding and deployment. In order to assess deployment forces and the impact of joint flaws on global behaviour, these effects are often approximated in finite element analyses using rotational springs or nonlinear contact elements that replicate the interaction between pins, bars, and hubs [14].

For scissor-type deployable structures, where friction and geometric tolerances can drastically impact unit synchronisation and change the load–displacement response, joint modelling is very crucial. As a result, the creation of trustworthy numerical models that strike a balance between computational effectiveness and physical realism is essential for design optimisation. This allows engineers to evaluate performance under service loads and deployment scenarios while taking into consideration the intricate mechanical behaviour of connections.

2 DESCRIPTION OF THE SCISSOR-TYPE DEPLOYABLE STRUCTURE

2.1 General

The purpose of the current thesis is to find and validate an optimal joint geometry, as well as a deployable structure able to counteract the phenomenon of eccentricity in joints. The deployable structure belongs to the category of scissor structures and consists of scissor-like elements (SLEs) connected by hinged joints. This chapter presents the outline and generation of the structure's geometry in its initial studied form. It explains the number and layout of the scissor-like elements and their connection points to form a single curvature shelter. In addition, the chapter focuses on the geometrical approach of using "double" scissor-like elements, a term explained below, to form the final structure.

2.2 Geometrical approach

The deployable structure studied in the current thesis consists of scissor-like elements repeated both radially and axially as shown in Fig.18, forming a single-curve shelter able to alter its geometry from a closed to a fully deployed form. Each scissor-like element is connected to the others using hinged joints, allowing the relative rotation around the axis perpendicular to the joint-member system during the deployment process. One of the basic assumptions in designing the structure is the fact that each member has the same length, an assumption that is adopted in other similar studies [15]. This parameter allows the development of a simpler structure, easier to assemble.

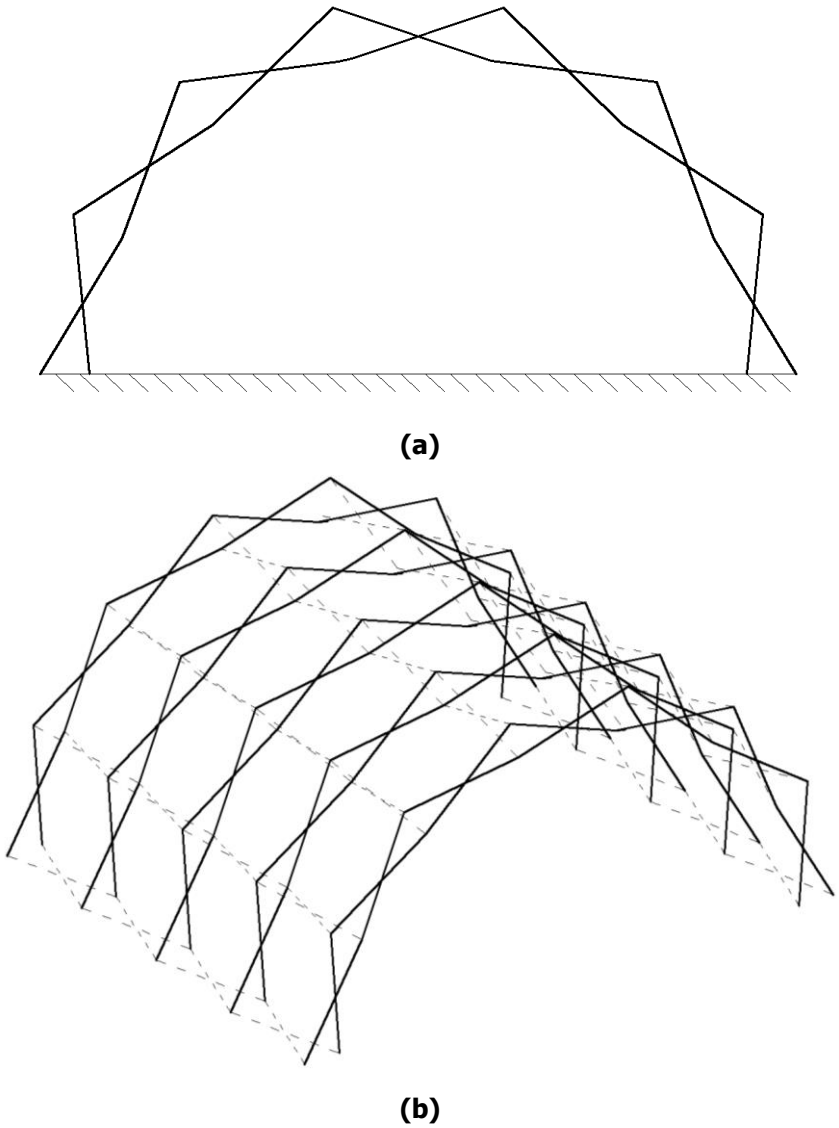

(a)

(b)

Figure 16. (a) Radial repetition of scissor-like elements (SLEs) forming a deployable frame; (b) axial repetition of the frame leading to the formation of a single-curvature deployable structure.

The geometrical approach was based on the geometric parameters that define the outlay of the structure at the fully deployed state. The first step consists of defining the characteristic geometry of the structure, followed by establishing basic parameters such as structural thickness and the number of scissor-like elements in each arc. Specifically, parameters including structural thickness (t), internal radius (R_{int}) and element count were adopted from similar studies [15], while other geometric definitions were determined as part of this thesis. The combination of these parameters allows the definition of the length of the scissor-like element members and subsequently the geometry of the whole structure.

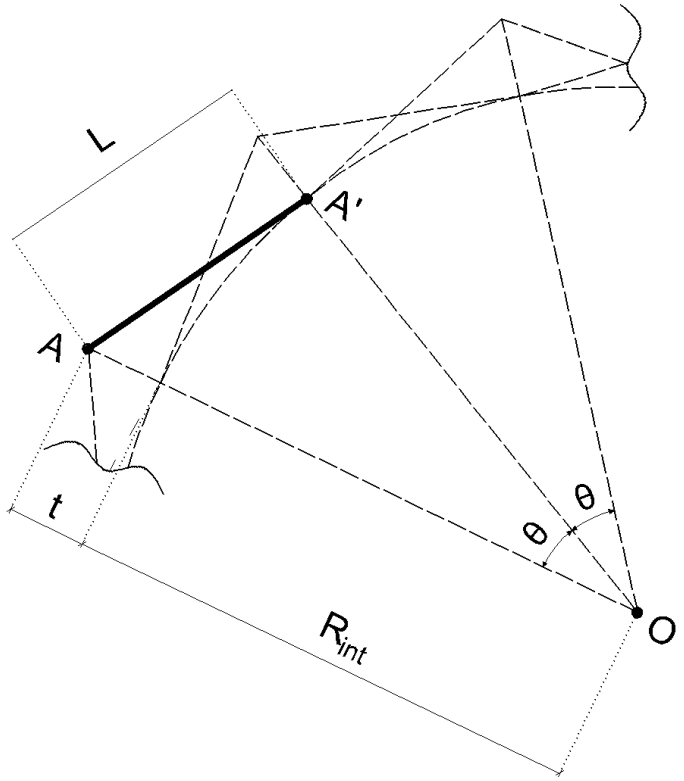

Figure 17. Definition of the structural thickness t, internal radius R_{int}, and member length L.

For the calculation of the member length L, the law of cosines will be used at the triangle AOA' (Eq.3-1) as approached in similar studies [15], where t is the structural thickness as mentioned above, R_{int} the internal radius of the frame and θ angle of each SLE relative to the center of each frame.

$$L = \sqrt{{R_{int}}^2 + (R_{int} + t)^2 - 2 \cdot R_{int} \cdot (R_{int} + t) \cdot \cos\theta} \qquad (3\text{-}1)$$

By substituting the thickness equal to 45cm, angle θ with the product of 180°/7 dividing the angle of the full frame by the number of selected SLEs, and the internal radius R_{int} with 300cm, the member length results in 150cm.

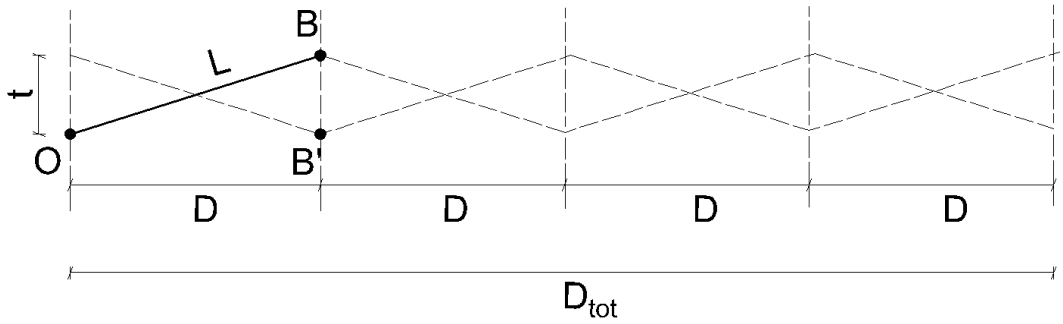

Figure 18. Definition of the distance between the frames.

A similar methodology is followed for the calculation of the translational members' length. By simply applying the Pythagorean theorem as shown in Eq. 3-2 in triangle BOB' as shown in the figure, the distance between the frames is obtained. The structural thickness t, as well as the translational members' length, remains the same in order to accommodate the initial assumption. The final result of the distance D is 143cm. This thesis assumes that the deployable structure consists of 5 polar frames; as a result, the translational SLEs will be 4, resulting in an overall length of 572cm as shown in Eq. 3-3.

$$D = \sqrt{L^2 - t^2} = \sqrt{150^2 - 45^2} = 143cm \tag{3-2}$$

$$D_{tot} = 4 \cdot D = 572cm \tag{3-3}$$

In conclusion, the final geometrical forming of the structure in its deployed form is defined by the parameters mentioned above. The final internal height of the structure is 300 cm. The length of the structure is 572 cm. The internal and external widths are 600 cm and 690 cm, respectively. The final length of the members, both translational and polar, is 150 cm. This approach does not consider that, to form a joint without eccentricities, double scissor-like elements will be used. This increases the length of the structure slightly. This need arises from ensuring the coincidence of the axes does not occur during folding and unfolding. Despite these factors, the basic geometrical dimensions remain as calculated for the later development of the geometrical model.

2.3 Connections of scissor-like elements

For the connection of both linear and translational elements between them, at first, the choice was a steel connection hinged joint that coincides with the polar and the translational elements, respectively. In contrast to ideal or facilitated solutions, the current thesis adopts the assumption that this joint will not consist of any welded parts. The assumed manufacturing process will be either the moulding of the joints or the most likely process of CNC machining. This approach is more accurate and provides better control over the tolerances.

As of the initial geometrical generation of the connection, the source will be the geometry resulting from the geometrical generation of the structure. The fundamental lines that cross the centre of the cross-section and the joint form the initial outlay of the joint-member connection, as shown in Fig. 19. In the same figure, the problem addressed by this thesis is highlighted as mentioned above. The phenomenal eccentricities ePO, eTR result in a non-symmetrical way of applying the axial forces to the joint. Moreover, the dimensions of the joint, as well as the cross sections and the thread hole diameter, cannot be defined from the beginning because they depend on the final cross sections.

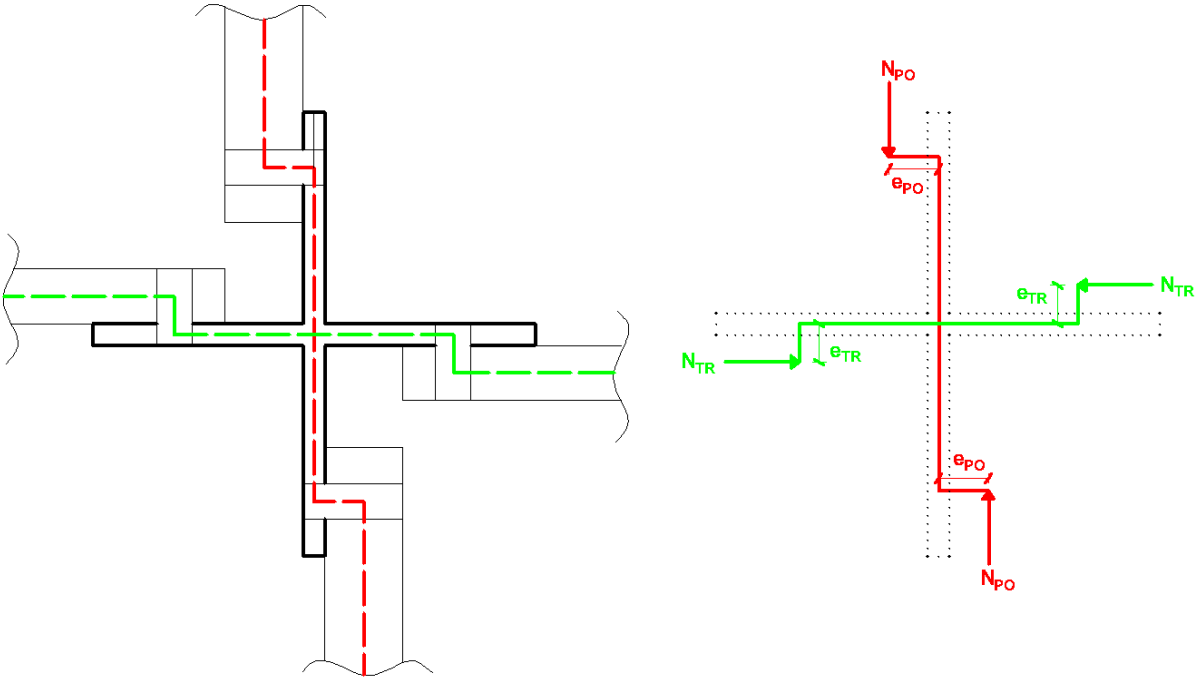

Figure 19. Geometrical representation of the joint based on the initial member assumption (left), and the load path of external axial forces to the joint (right).

Apart from the cross-type joint displayed in Fig. 19, the connection between the elements can also be achieved using the core-and-pin outlay [5], as displayed in Fig. 20. This system uses a central round element, either a hollow section or a cylindrical prism, into which bolts are inserted. The connected elements are then attached to the core, allowing them to rotate freely around it.

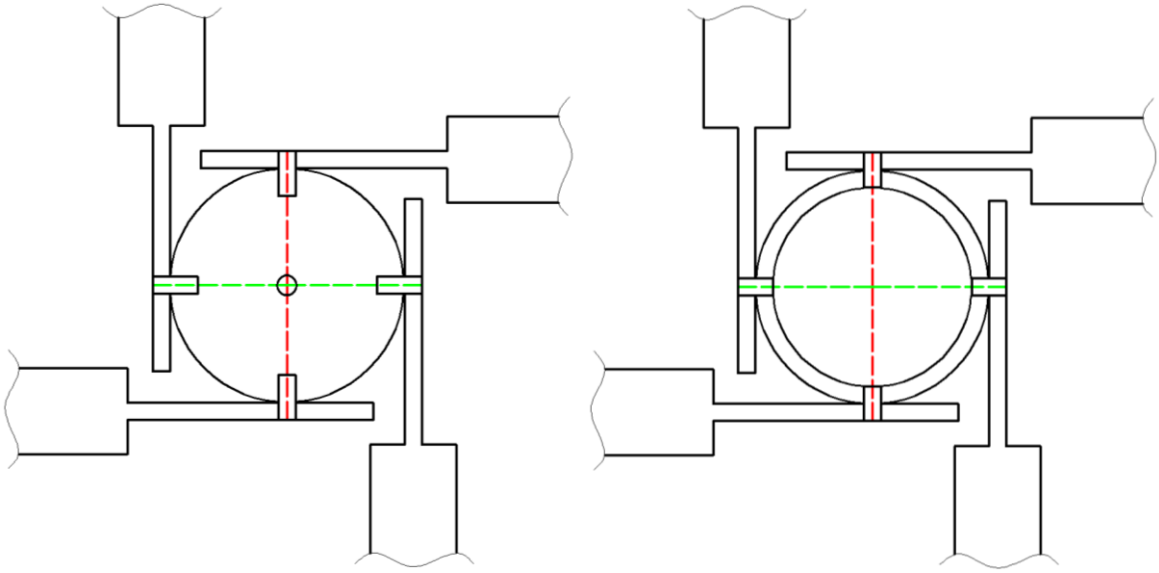

Figure 20. Geometrical representation of the core-and-pin joint: cylindrical prism (left), circular hollow section (right).

The key advantage of this joint is its efficient reduction of eccentricities that are present in cross-type joints. However, a significant disadvantage is the required modification of member tips to the specific "fin" shape detailed in Fig. 20. This thesis studies how altering a cross-type joint configuration eliminates eccentricities, whereas in the explored joint, the design itself inherently prevents them.

Another approach is the hub connection of the elements. This approach, the geometrical approach, consists of a central joint of circular type that connects more than four elements in angles smaller that the 90o presented in the previous schemes. The hub-type joint, along with the different number of elements that can be connected are shown in Fig. 21.

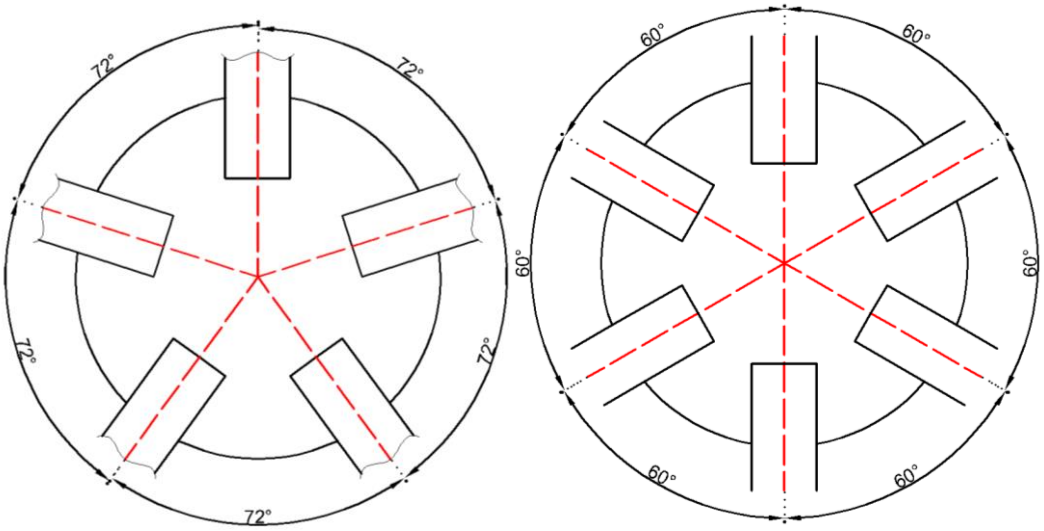

Figure 21. Geometrical representation of the multi-fin hub joint [1]: five-element multi-fin hub (left) and six-element multi-fin hub (right).

One of the major advantages of the multi-fin hub joint is the fact that its circular form allows for the definition of a rigid, closed formation using the slots as guidance into common planes that cannot coincide. The distribution of forces is also symmetrical due to the central plate behaviour as a rigid joint, making the deployment process easier for the structure. The possibility of creating complicated geometries is another major advantage of this type of joint. This means that it can be used in domes or other types of complicated scissor-type structures.

In order to eliminate this eccentricity from the flow of the loads to the joint, this thesis adopts the term of a "double" scissor-like element. The difference between single and double scissor-like elements is the fact that the first consists of two members interconnected and the predefined point (depending on the structure) along their length, while the second consists of three members connected at the same point mentioned above, as shown in Fig.22.

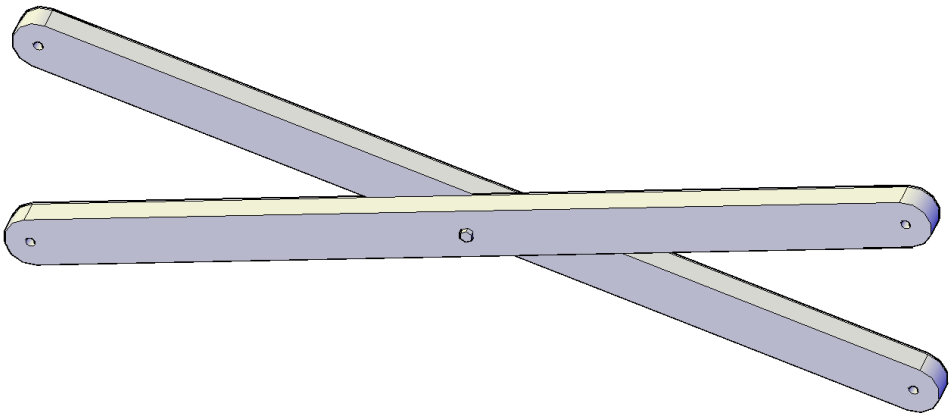

(a)

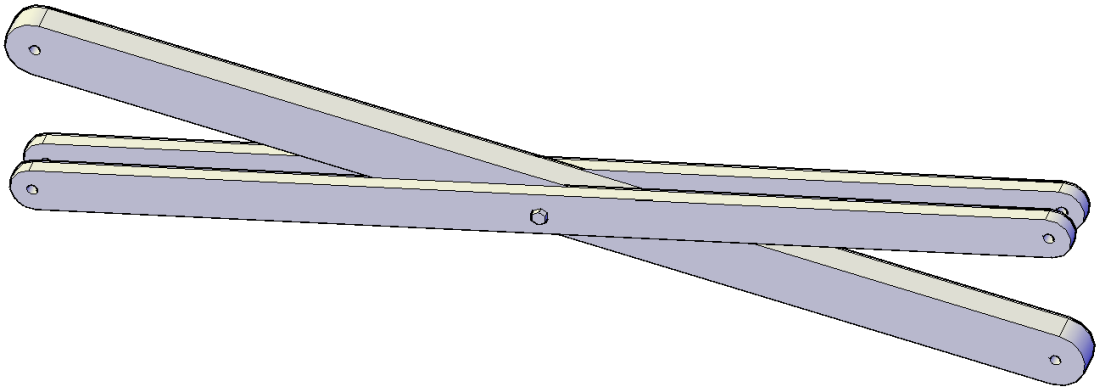

(b)

Figure 22. (a) Single scissor-like element (SLE); (b) double scissor-like element (SLE) configuration.

In the case of the double scissor-like elements, the two "external" members are connected through the same thread hole at the joint, forming a section-joint-section connection that moves the two external members as one. While in the middle of the double scissor-like elements, this is achieved by means of a single bolt located at the intermediate hinge point, allowing the relative rotation of the members as shown in Fig. 23.

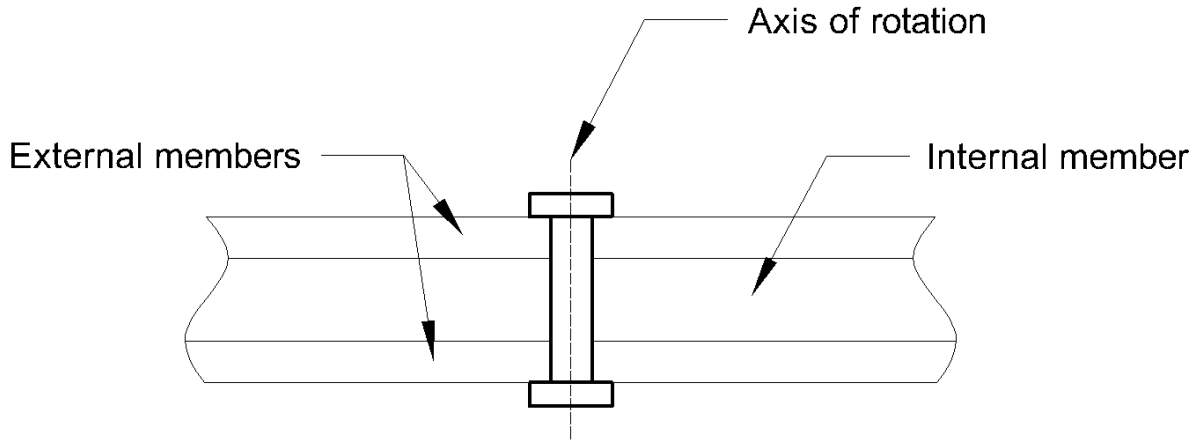

Figure 23. Intermediate connection of double scissor-like elements.

3 JOINT ECCENTRICITY IN SCISSOR-TYPE DEPLOYABLE STRUCTURES

3.1 Origin of eccentricity in joints

3.1.1 Eccentricities introduced by joint and member geometry

In scissor-type deployable structures, eccentricities are introduced when the axes of the members across the sides of the joint do not pass through the same spot in the joint. This means that an axis of symmetry cannot be formed within the joint, and the distance between the axis of symmetry and the axis of the member is referred to as the eccentricity (e_{PO}, e_{TR}) as shown in Fig. 24. The cause of this eccentricity is that the scissor-like elements must follow a specific geometric path, and for this to happen, they must be aligned in some way. To be more specific, the real geometry of the sections and the joint introduces this kind of eccentricity. In the ideal kinematic description of the scissor-like elements, all member axes are considered to meet at the same point without any eccentricities. In real-life structures, the thickness of the members or joints, as well as the distances of the thread holes and the dimensions of the sections, introduce this kind of eccentricity that influences the static behaviour of the structure, introducing further moments and variations into the stiffness of the structure.

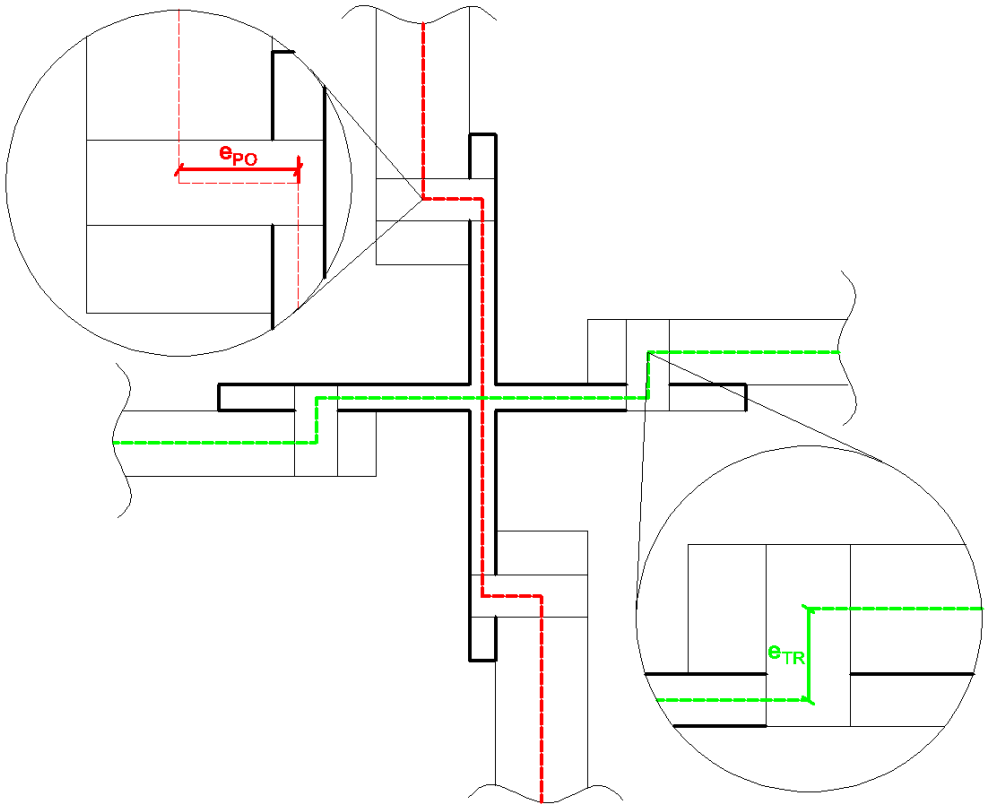

Figure 24. Geometrical representation of the eccentricities in the joint-member connection.

Cross-section eccentricity occurs when the axes of connected members at a joint cannot align because of the section width. In scissor-type deployable structures, threads inside flanges form joints, shifting the member axis from the theoretical connection point. This eccentricity introduces secondary moments in the joint and influences the overall structural response under operational loads.

The joint geometry is one of the most important factors in eccentricity generation. In most real-life applications, joints are made from steel flanges or other three-dimensional connection elements. These elements have a specific thickness. This thickness shifts the connection point of the members away from the centre of the joint, introducing eccentricity. Such eccentricity influences the load transfer from the members to the joint and creates additional moments under operational loads.

Another major factor that plays a significant role in the eccentricity is the eccentricity introduced by connection plates, washers, or other parts that are between the joint and the member. When two members are connected using bolts, washers, flanges or other parts are used as well in order to align the members [1]. The thickness of these minor parts introduces more eccentricity to the joint, resulting in further increase of the lever of the additional moments, resulting in increased stresses and overall static response.

3.1.2 Influence of eccentricity on structural behavior

The existence of eccentricity in deployable structures' joints can significantly affect the overall static and kinematic behaviour of the system. In ideal kinematic models of typical scissor-type structures, members are considered connected at the same axis; as a result, the loads are transferred axially from the members to the joint without the appearance of additional moments into the joint. In real-life structures, though, due to the dimensions of the sections, the geometry of the joint, and the location of the bolts, the theoretical member axes do not match the practical point.

This eccentricity leads to the development of secondary moments into the joints and members, affecting the stiffness of the joint and the distribution of the internal forces into the structure. Additionally, the kinematic behaviour of the assembly can be affected during the process of deployment, while in many cases it affects the deformed state of the structure under specific loading, resulting in unexpected structural response. For this reason, the initial geometrical approach and the finite model implementation using simple linear elements for the whole structure need to consider this type of eccentricity. In one approach, the eccentricity can be introduced by the joint configuration as shown in Fig. 25.

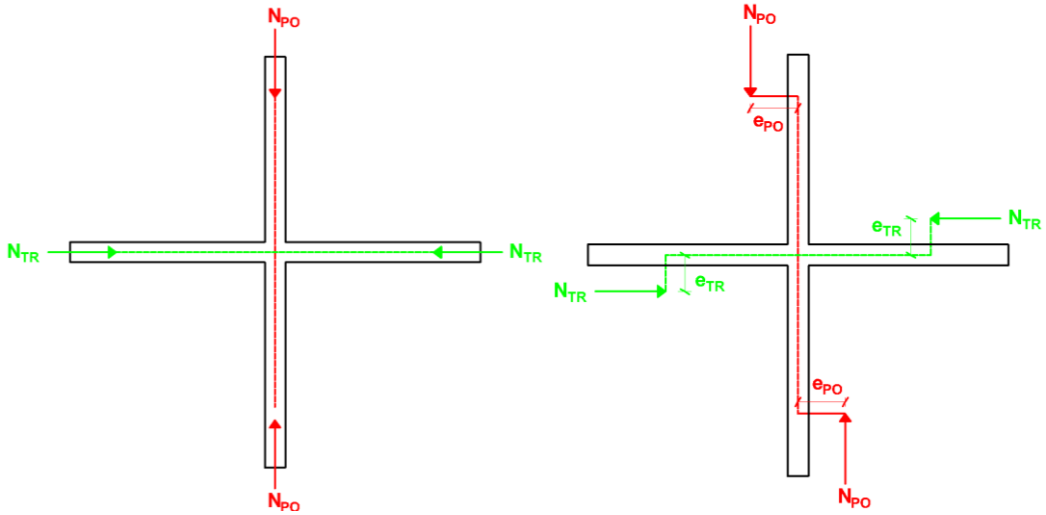

Figure 25. Schematic representation of the eccentricity introduced by the joint configuration, showing the offset between the theoretical intersection of member axes and the actual connection point.

While the eccentricity can be easily defined in cross-type joints, it is also present in the type of joints mentioned in Chapter 2. At the core-and-pin joints, the eccentricity is practically increased in comparison with the cross type by the very geometry of the joint. The fact that the members are placed at 90 degrees to their corresponding axis to the joint increases the eccentricity significantly.

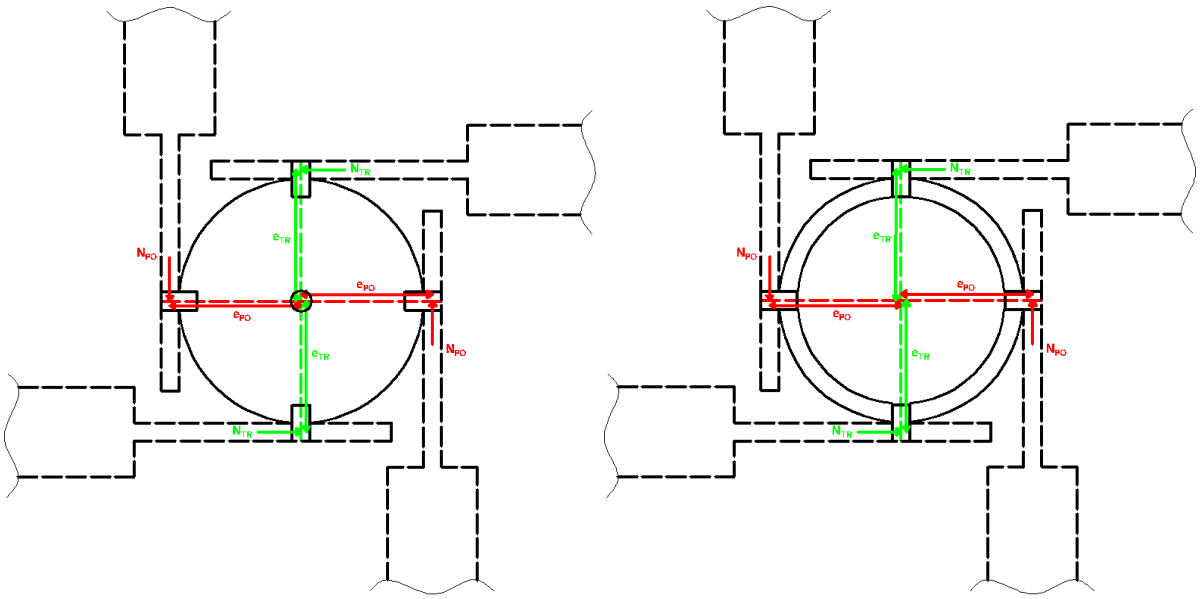

Figure 26. Schematic representation of the eccentricity introduced by the core-and-pin joint configuration: cylindrical prism (left), circular hollow section (right).

The multi-fin hub joints do not present eccentricities in their general application due to the central plate of circular type that, in most cases, consists of radial sockets where the members are connected. The transfer of the axial loads to the joint is displayed in Fig. 27.

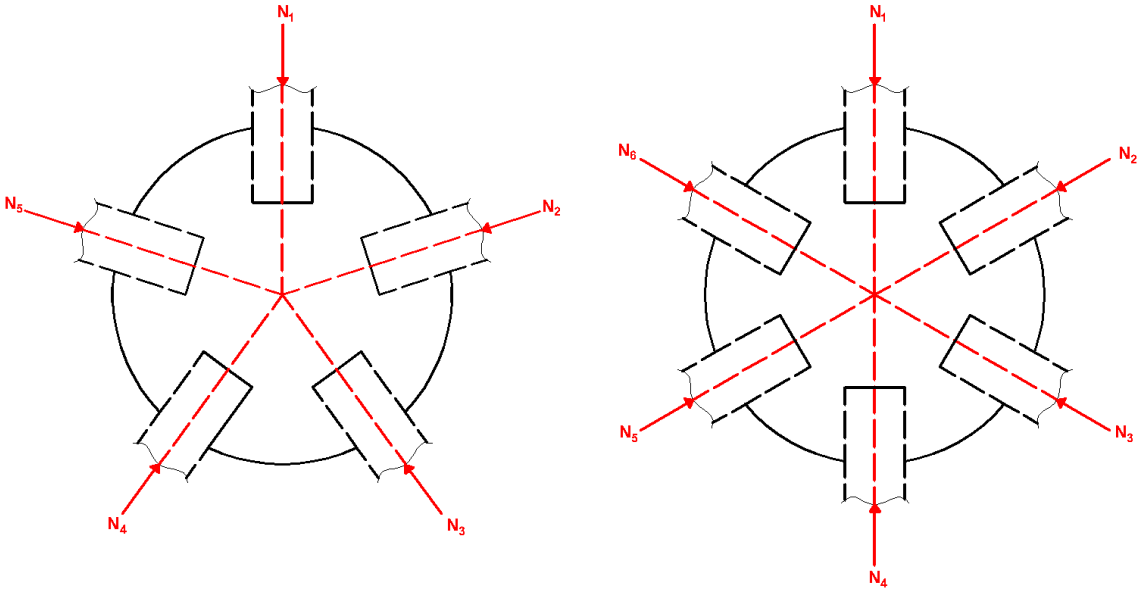

Figure 27. Schematic representation of the axial load transfer from the members to the multi-fin hub joint.

Another suggestion by Roovers et al. [3] introduces rotational freedom during deployment, enabling smooth kinematic motion of the elements by selectively constraining certain rotational directions while permitting in-plane rotation of specific members. As a result, the joint acts as both a deployment mechanism and a joint. The final configuration of the joint presents some deliberately placed eccentricities, reducing unwanted secondary stresses during deployment. As presented in the corresponding study [4], the overall stiffness and structural performance are enhanced. Fig. 28 shows the joint based on fixed joint vectors. Four out of the six members connected to the joint can rotate in-plane, while the rest can "adjust" their angle to the center of the joint.

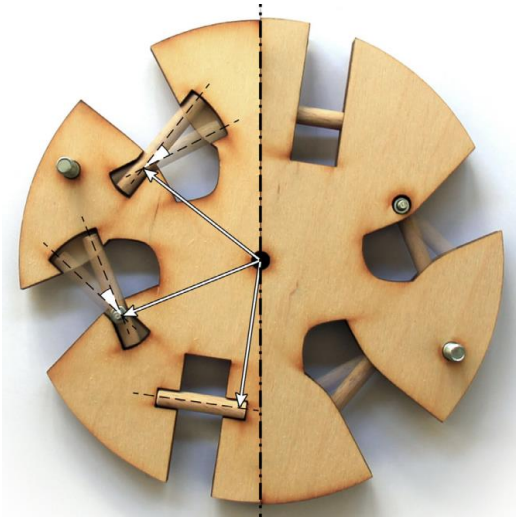

Figure 28. Experimental multi-member hub joint developed for the deployable triangulated scissor grid system [4].

4 ACTIONS ON THE STRUCTURE

4.1 Dead loads

The actions on a structure depend on its environment and structural characteristics. During design, the structure is dimensioned to meet stability and serviceability requirements. In this study, loads for structural design are classified as permanent (G), such as self-weight, connections, and covering, and variable (Q), such as snow and wind. Since deployable shelters are for temporary use, temperature variations and seismic actions are neglected. The calculation and modelling assumptions for these actions follow EN 1990 [16] and EN 1991 [17].

4.1.1 Self-weight of the structural members

Aluminium was adopted as the material for the structural members of the construction. According to EN 1991-1-1 [17], the unit weight of aluminium is taken as γ_{al} = 27.0 kN/m³. The self-weight of the members was automatically included in the numerical simulation through the analysis software.

4.1.2 Self-weight of joints

Structural steel was adopted as the material for the connections. According to EN 1991-1-1, the unit weight of structural steel is taken as γ_{st} = 78.5 kN/m³. For the calculation of the self-weight of a typical steel joint, its volume was assumed equal to V_{joint} = 175 cm³ as adopted from similar studies [18] . Consequently, the self-weight was determined from Eq. (4-1).

$$G_{joint} = \gamma_{st} \cdot V_{joint} \tag{4-1}$$

By substituting γ_{st} and V_{joint} to Eq. (4-1) the G_{joint} is obtained as 13.74×10^{-3} kN. A similar approach was followed, based on relevant studies [15], for the estimation of the contribution of washers, threads, and nuts. The total weight per joint was adopted from the same reference [15] and taken as 4.6×10^{-3} kN. This load was introduced in the numerical model as a concentrated load at the centroid of each joint and will be revised following the finalization of the joint geometry.

4.1.3 Self-weight of the covering

The covering was assumed to consist of a tensioned membrane with a PVC coating [15]. Based on values reported in similar studies, the surface density was taken as $\rho_{memb} = 1.45$ kg/m², corresponding to a self-weight of $\gamma_{memb} = 14.5 \times 10^{-3}$ kN/m². Similar to the approach adopted for the joint loads, the membrane load was introduced into the numerical model as a concentrated load applied at the centroid of each joint.

4.1.4 Self-weight of cables

Due to its negligible influence, the self-weight of the cables of the bracing system was not considered as a separate action in the design process. Nevertheless, as expected, their contribution is inherently included in the numerical model.

4.2 Live loads

4.2.1 Snow load

Snow load is calculated according to Part 1-3 of EN 1991 [17] for civil engineering applications and structures under a height of 1500m. The core equation of calculating the snow load is described in Eq. (3-3). For this case, certain assumptions regarding some parameters demanded by the regulations needed to be made due to the special nature and geometry of the structure.

$$s = \mu_i \cdot C_e \cdot C_t \cdot s_k \tag{4-2}$$

Where μ_i corresponds to the coefficient of shape of the snow load, C_e corresponds to the exposure coefficient, C_t corresponds to the thermal coefficient, and s_k corresponds to the characteristic value of the snow load on the ground.

For the coefficient of shape of the snow load, the relative categorisation for cylindrical roofs according to EN1991-1-3 [17], as shown in Fig., was adopted, which defines the snow load in two cases.

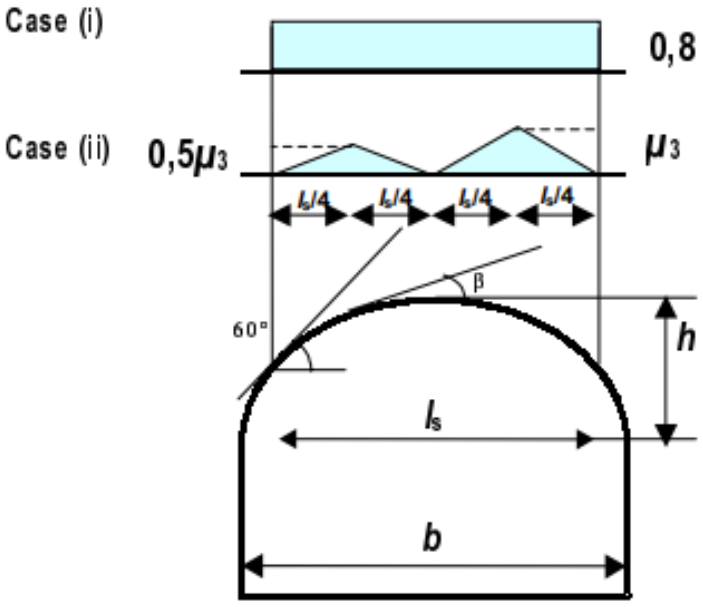

Figure 29. Snow load shape coefficients for cylindrical roof according to EN1991-1-3 [17].

For the case of non-drifted snow, according to EN 1991-1-3, the shape coefficients are determined based on β, representing the roof slope angle, b, the internal roof height, and h, the maximum roof width. The following equations, Eq. (3-3;7), describe the calculation process :

$$\mu_i = \mu = 0.8 \tag{4-3}$$

$$\mu_{ii} = \mu_3 = 0.2 + 10 \cdot \frac{h}{b} \tag{4-4}$$

For b=690cm, h=345cm and β≤60° respectively, μ_i and μ_{ii} are obtained as:

$$\mu_i = \mu = 0.8 \tag{4-5}$$

$$\mu_{ii} = \mu_3 = 0.2 + 10 \cdot \frac{345}{690} = 5.20 \tag{4-6}$$

But, μ_{ii} should be less than equal to 2 so, μ_{ii} = 2.0 is adopted.

For the exposure coefficient, the chosen value is Ce = 1.0 for normal conditions. The thermal coefficient is adopted as Ct=1.0 as the minimum coefficient due to the assumption of low heat loss through the roof.

The characteristic value of the snow on the ground will be based on Eq. (3-7) that describes the relationship between the A, altitude above the sea and $s_{k,0}$, which is the characteristic value of the snow load at sea level based on the map shown in the national annex of EN1991 Fig.

$$s_k = s_{k.0} \cdot \left[1 + \left(\frac{A}{917}\right)^2\right] \tag{4-7}$$

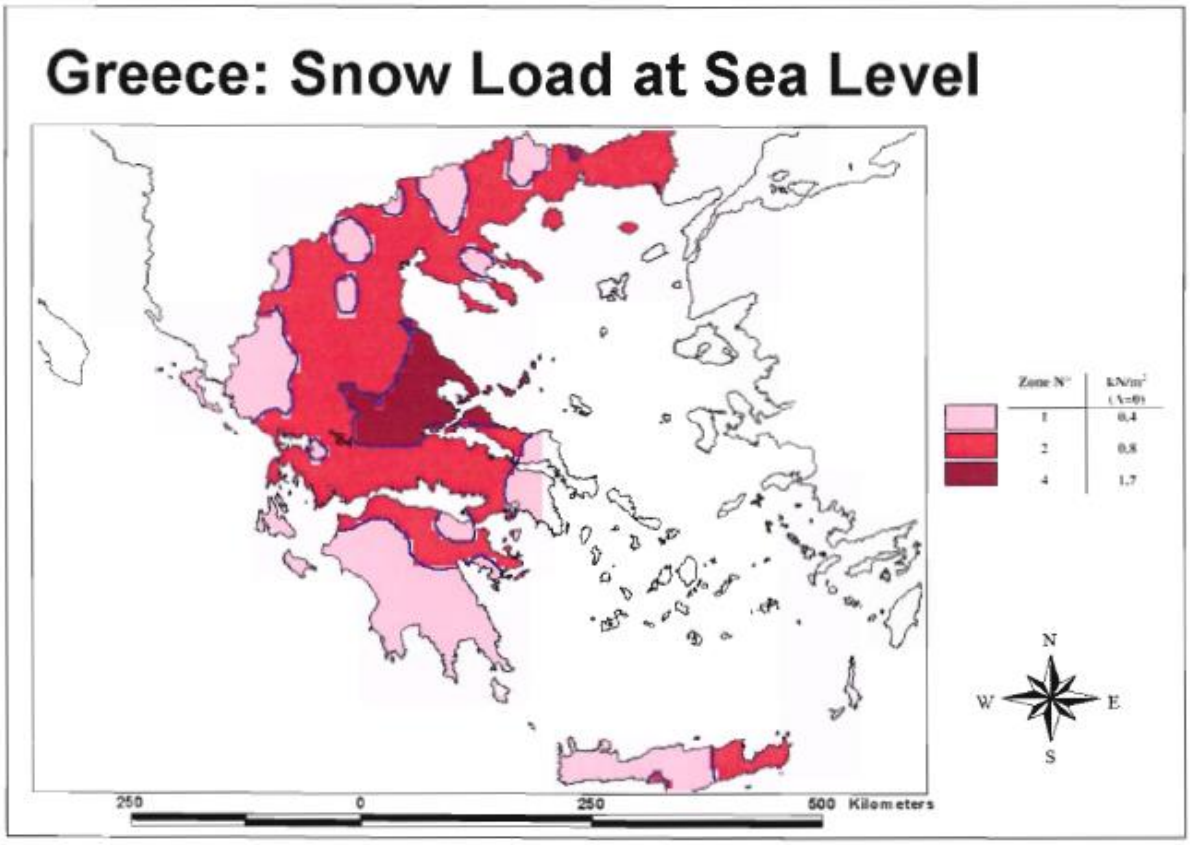

Figure 30. Characteristic value of the snow load at sea level for Greece according to EN1991-1-3.

Using Fig. 1,0 is adopted as 1.7 kN/m^2 in order to take into account the worst possible case, while the assumed height will be A=200m as adopted from similar studies [15]. As a result Eq. (3.7) becomes:

$$s_k = 1.7 \cdot \left[1 + \left(\frac{200}{917}\right)^2\right] = 1.781 kN/m^2 \quad (4\text{-}8)$$

By substituting the values calculated above Eq. (3-7) becomes:

$$s_i = \mu_i \cdot C_e \cdot C_t \cdot s_k = 0.8 \cdot 1.0 \cdot 1.0 \cdot 1.781 = 1.425 kN/\,m^2 \quad (4\text{-}9)$$

$$s_{ii} = \mu_i \cdot C_e \cdot C_t \cdot s_k = 2.0 \cdot 1.0 \cdot 1.0 \cdot 1.781 = 3.562 kN/\,m^2 \quad (4\text{-}10)$$

The roof of the shelter does not form a lean surface due to the presence of the converging and the irregular geometry of the SLEs; for this reason, in this study, it is assumed that the section of the roof is a half circle and the following Fig.26.

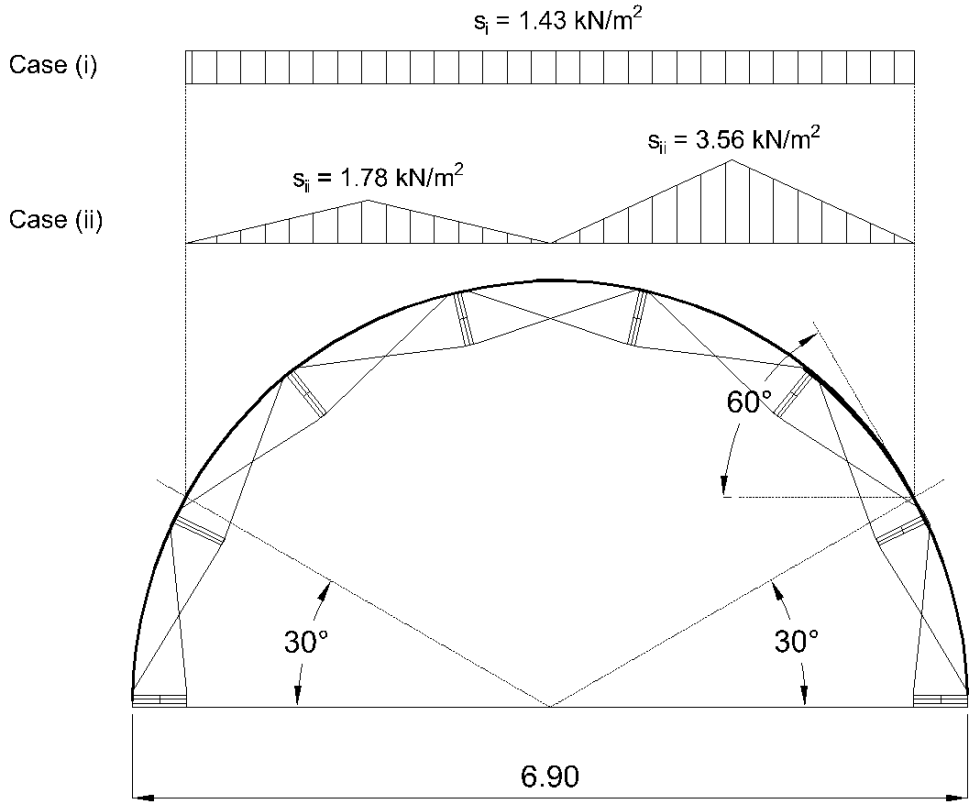

Figure 31. Distribution of snow loads to the roof.

As with the previous loads, the load was introduced into the numerical model as a concentrated load applied at the centroid of each joint. The loads were distributed respectively depending on the area covered by the joint.

4.2.2 Wind actions

For wind actions, EN 1991-1-4 [17] was used, which describes, for short, civil engineering applications that both external and internal wind pressures should be taken into account. The external wind pressure is calculated as follows (Eq. 4-11), where $q_{p(ze)}$ stands for the peak velocity of the wind, z_e is the reference altitude for the external pressure and c_{pe} is the coefficient of external pressure.

$$w_e = q_{p(z_e)} \cdot c_{pe} \tag{4-11}$$

The internal pressure that acts perpendicularly to the internal surface of the structure is calculated as following (Eq. 4-12). Where $q_{p(zi)}$ stands for the peak velocity of the wind, z_i is the reference altitude for the external pressure and c_{pi} is the coefficient of external pressure.

$$w_i = q_{p(z_i)} \cdot c_{pi} \tag{4-12}$$

The peak velocity of the wind $q_{p(z)}$ is calculated as following (Eq. 4-13), where $I_{v(z)}$ is the turbulence intensity at altitude z, p is the air density during windstorm of magnitude p=1.25kg/m^3, $v_{m(z)}$ is the

average wind velocity at altitude z above the ground, $c_{e(z)}$ corresponds to the coefficient of exposure, and q_b corresponds to the basic pressure.

$$q_{p(z)} = \left[1 + 7 \cdot I_{v(z)}\right] \cdot \frac{1}{2} \cdot p \cdot {v_{m(z)}}^2 = c_{e(z)} \cdot q_b \tag{4-12}$$

The turbulence intensity $I_{v(z)}$ at altitude z is calculated as following where, kI corresponds to the coefficient of turbulence equal to 1.0, $c_{o(z)}$ is the coefficient of territorial influence which is also equal to 1.0, z_0 corresponds to the length of roughness, z_{min} the minimum altitude in meters which is taken as 0.05m according to Tab. 4-1 of EN1991 part 1-4 [17] and zmax the maximum altitude which will be considered equal to 200m :

$$I_{v(z)} = \frac{k_I}{c_{o(z)} \cdot \ln\left(\frac{z}{z_0}\right)} \text{ for } z_{min} \le z \le z_{max} \tag{4-13}$$

$$I_{v(z)} = I_{v(z_{min})} \text{ for } \le z \le z_{min} \tag{4-14}$$

Tab 4-1. Terrain categories and terrain parameters according to EN1991 part 1-4 [17].

Terrain category	z_0 (m)	z_1 (m)
0 Sea or coastal area exposed to the open sea	0.003	1
I Lakes or flat and horizontal area with negligible vegetation without obstacles.	0.01	1
II Area with low vegetation such as grass and isolated obstacles (trees, buildings) with separations of at least 20 obstacle heights.	0.05	2
III Area with regular cover of vegetation or buildings or with isolated obstacles with separations of maximum 20 obstacle heights (such as villages, suburban terrain, permanent forest).	0.3	5
IV Area in which at least 15% of the surface is covered with buildings and their average height exceeds 15m.	1	10

The average wind velocity $v_{m(z)}$ at altitude z above the ground is calculated as follows (Eq. 4-14), where $c_{r(z)}$ corresponds to the coefficient of roughness, and v_b is the basic wind velocity.

$$v_{m(z)} = c_{r(z)} \cdot c_{0(z)} \cdot v_b \tag{4-15}$$

The coefficient of roughness $c_{r(z)}$ is calculated as follows:

$$c_{r(z)} = k_r \cdot \ln\left(\frac{z}{z_0}\right) \text{ for } z_{min} \le z \le z_{max} \tag{4-16}$$

$$c_{r(z)} = k_r \cdot \ln\left(\frac{z}{z_0}\right) \text{ for } \le z \le z_{min} \tag{4-17}$$

Where kr corresponds to the terrain coefficient which is calculated as follows:

$$k_r = 0.19 \cdot \left(\frac{z_0}{z_{0,II}}\right)^{0.07}, \qquad z_{0,II} = 0.05m \tag{4-18}$$

The basic wind velocity is calculated as follows (Eq. 4-19), where c_{dir} is the coefficient of wind direction, C_{season} corresponds to the coefficient of season, and $v_{b,0}$ is defined as the fundamental value of the basic wind velocity.

$$v_b = c_{dir} \cdot C_{season} \cdot v_{b,0} \tag{4-19}$$

The fundamental wind velocity, $v_{b,0}$ is defined as the characteristic 10-minute mean wind speed at a height of 10 m above ground level in terrain category II, independent of direction and season. According to the National Annex, $v_{b,0}$ is taken as 33 m/s for coastal and island regions within 10 km of the shoreline, and 27 m/s for inland areas as shown in Fig.27.

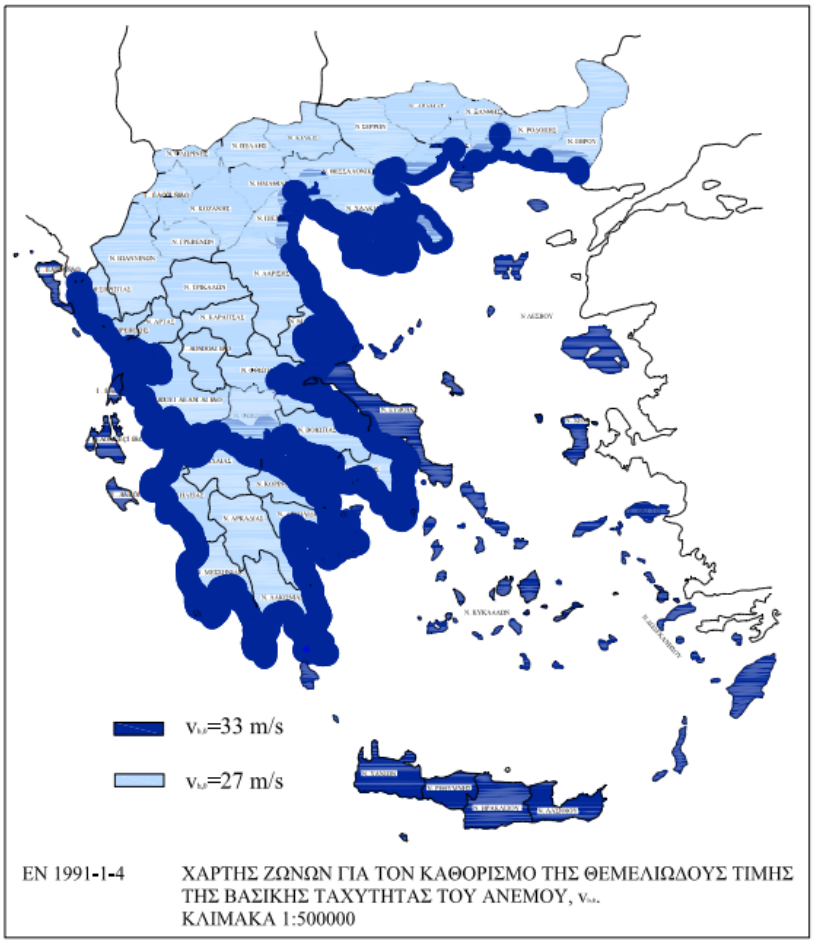

Figure 32. Fundamental wind velocity map for Greece.

The calculation of the coefficient of the external wind pressure cpe is based on the surface is dependent to the surface of application on the structure. For a surface less that $1m^2$ the external wind pressure is defined as $c_{pe,1}$ while for bigger that $10m^2$ the coefficient of external pressure is defined as $cp_{e,10}$ as shown in Fig.28.

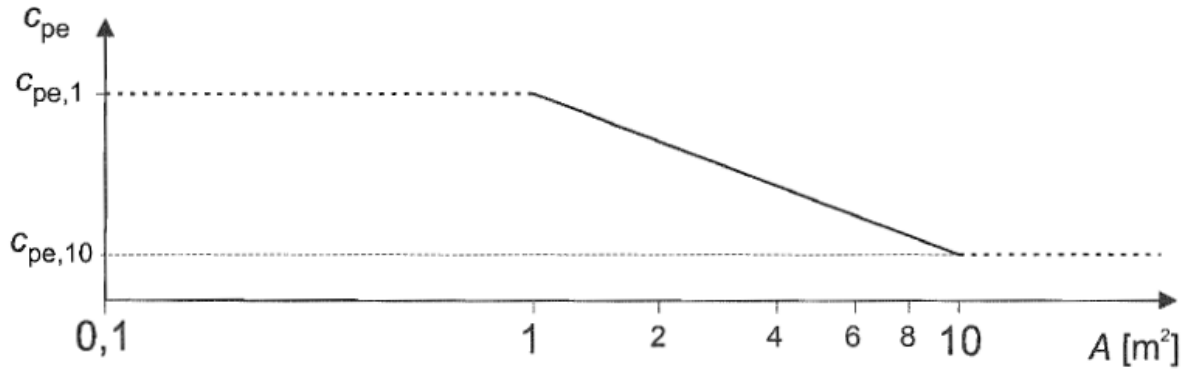

Figure 33. Calculation of the coefficient of external wind pressure for structures wind loaded area A between $1m^2$ and $10m^2$ [17].

For values of A between 1 and $10m^2$ it is calculated as follows (Eq. 4-20):

$$c_{pe} = c_{pe,1} - (c_{pe,1} - c_{pe,10}) \cdot log_{10} A \tag{4-20}$$

The wind load is separated into transversal and longitudinal directions. The transversal direction corresponds to the x direction according to Fig.29.

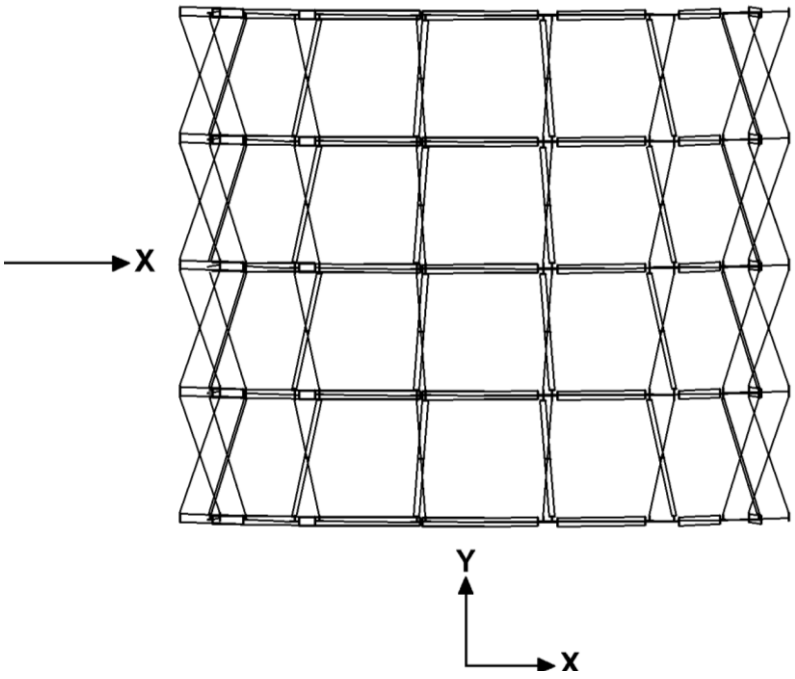

Figure 34. Transversal wind direction.

According to EN 1991 part 1-4, the structure is considered a cylindrical roof structure; as a result, the coefficient of external wind pressure cpe,10 is dependent on the ratios h/d and f/d that need to be between the margins 0.2≤f/d≤0.3, and h/d≥0.5. The following Fig.30 describes the graphical calculation of the pressure $c_{pe,10}$.

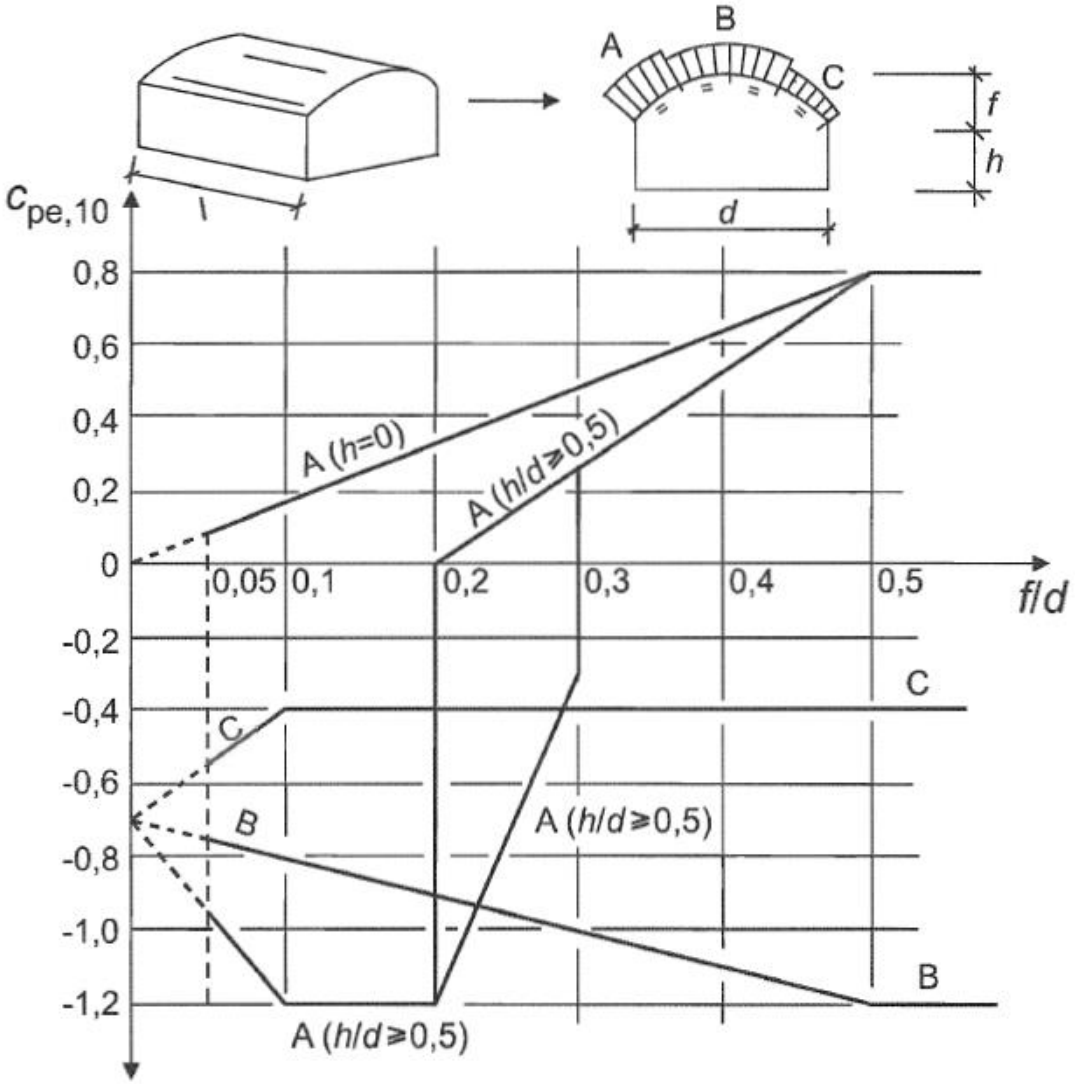

Figure 35. Recommended values of external pressure coefficients $c_{pe,10}$ for vaulted roofs [17].

For the structure, it is considered the wind pressure applied to the vertical surfaces of the front and the rear. For this case, the following Fig. defines the reference height that needs to be used. For this case, the width and the length of the side will be used as well, parallel to the wind direction. While the key for vertical walls is given by Fig., the proposed values for the coefficient of external pressure based on the ratio h/d are given by Tab 4-2.

Tab. 4-2. Recommended values of external pressure coefficients for vertical walls of rectangular plan buildings.

Zone	A		B		C		D		E	
h/d	$C_{pe,10}$	$C_{pe,1}$	$C_{pe,10}$	$C_{pe,1}$	$C_{pe,10}$	$C_{pe,1}$	$C_{pe,10}$	$C_{pe,1}$	$C_{pe,10}$	$C_{pe,1}$
5	-1.2	-1.4	-0.8	-1.1	-0.5		0.8	1	-0.7	
1	-1.2	-1.4	-0.8	-1.1	-0.5		0.8	1	-0.5	
≤ 0.25	-1.2	-1.4	-0.8	-1.1	-0.5		0.7	1	-0.3	

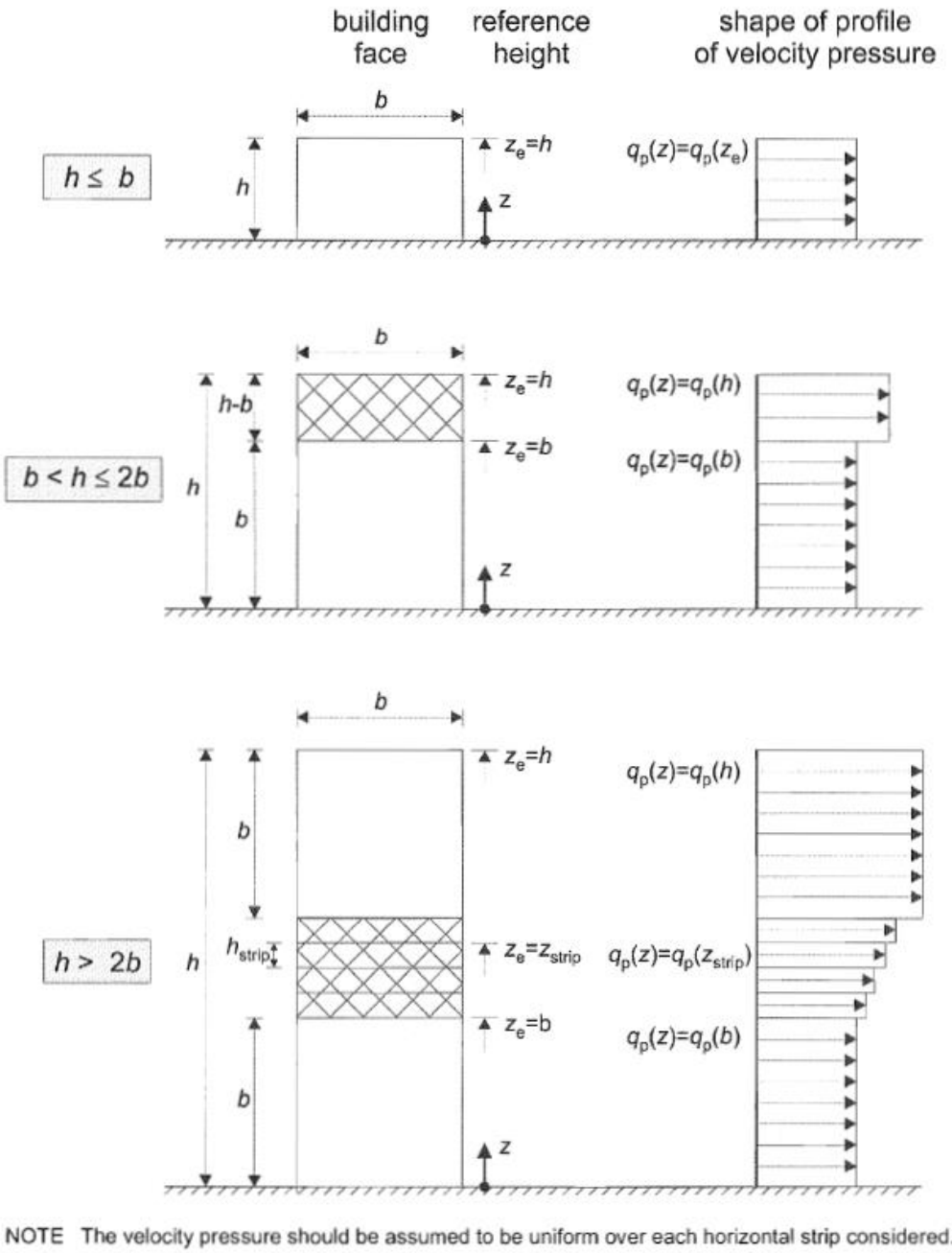

NOTE The velocity pressure should be assumed to be uniform over each horizontal strip considered.

Figure 36. Reference height, z_e, depending on h and b, and corresponding velocity pressure profile.

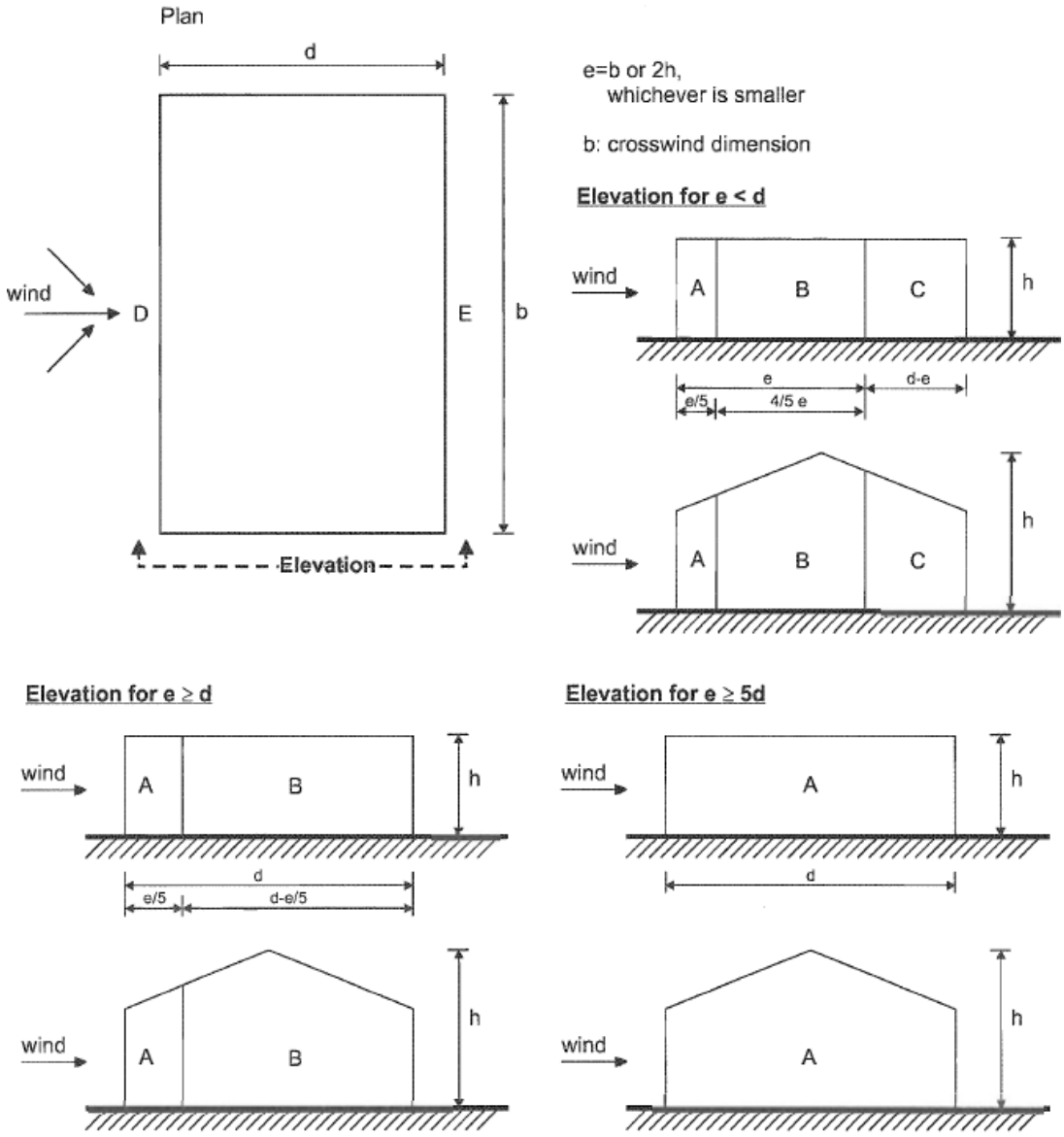

Figure 37. Wind pressure zones for vertical walls [17].

The wind along the y-direction was calculated according to EN 1991 Part 1-4 [17]. According to similar studies, the roof was assumed to be horizontal with sharp edges due to a lack of relevant information on calculations in the regulations. The distribution of the wind pressure zones is described in Fig.32, the direction of application is depicted in Fig.33, and the proposed coefficients of external pressure, c_{pe}, are listed in Tab. 4-3.

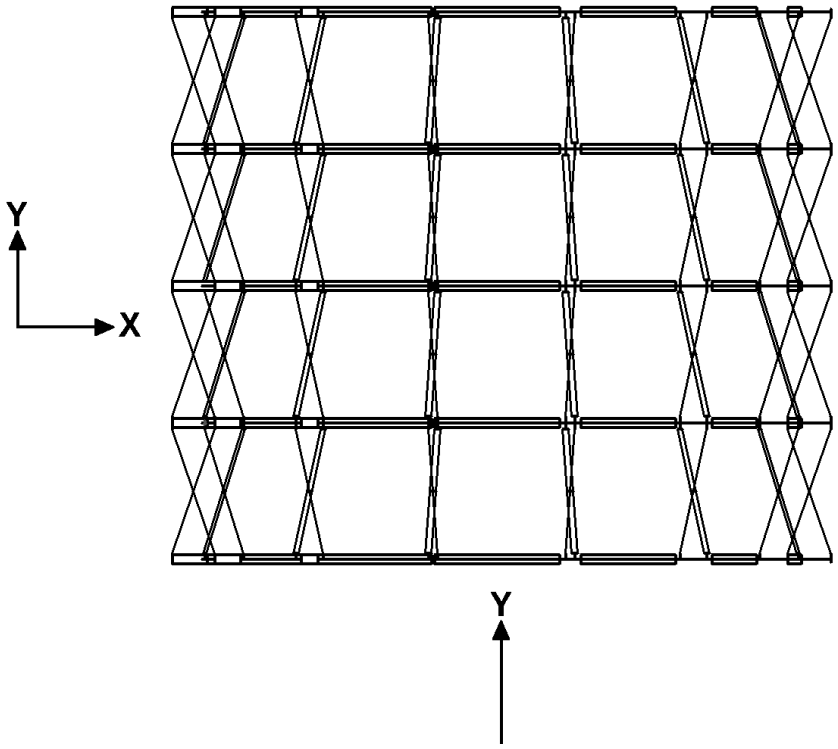

Figure 38. Longitudinal wind direction.

Tab. 4-3. Recommended values of external pressure coefficients for vertical walls of rectangular plan buildings.

Zone	F		G		H		I	
Type of roof	$C_{pe,10}$	$C_{pe,1}$	$C_{pe,10}$	$C_{pe,1}$	$C_{pe,10}$	$C_{pe,1}$	$C_{pe,10}$	$C_{pe,1}$
Sharp edges	-1.8	-2.5	-2.0	-0.7	-0.7	-1.2	0.2 -0.2	

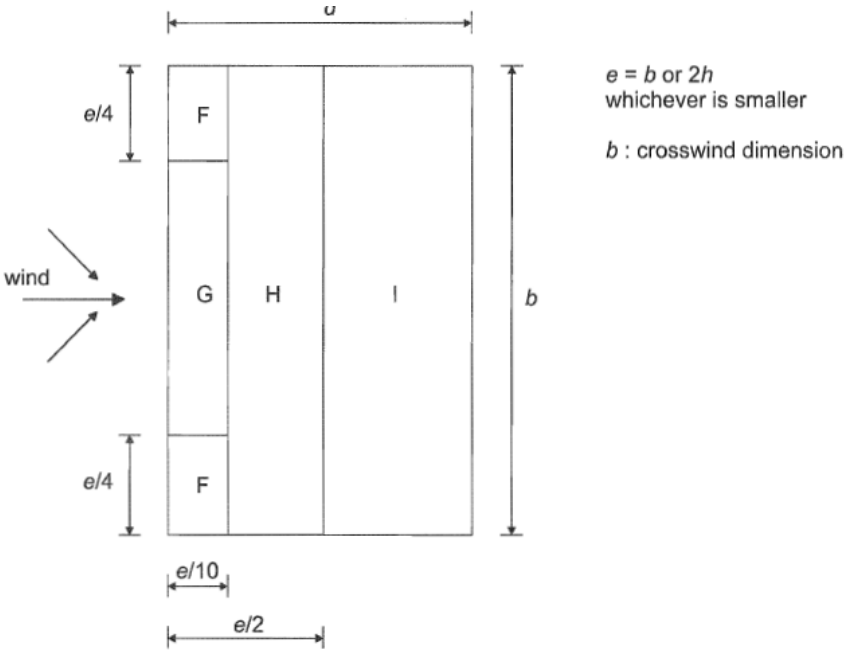

Figure 39. Wind pressure zones for flat roofs [17].

Internal and external pressures act simultaneously and must be analyzed together. As per EN 1991-1-4 [17], the internal pressure coefficient (c_{pi}) can conservatively be taken as the most unfavourable value between +0.2 and −0.3. For this structure, the fundamental wind velocity is considered 33 m/s, according to [15]. The area is classified as terrain category II. Fig.35 shows how external and internal pressures are applied to the structure.

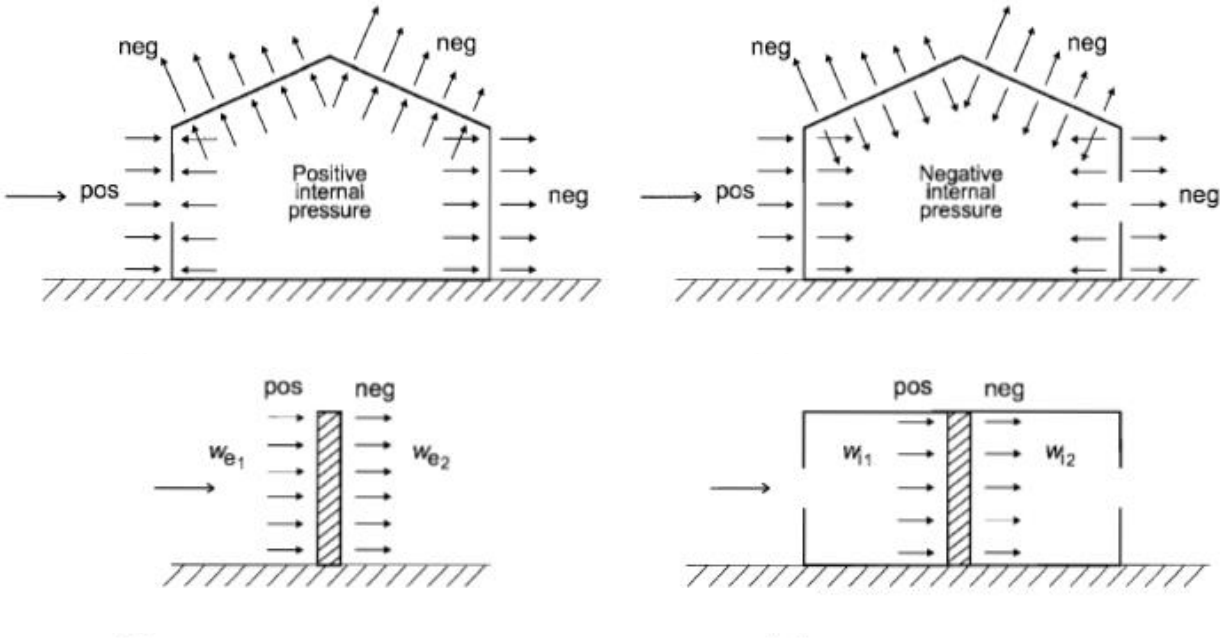

Figure 40. Wind pressure application in structures according to EN1991 Part 1-4 [17].

The fundamental wind pressure v_b is calculated as follows by Eq. (4-21) using Eq. 4-19, assuming cdir is equal to 1.0, c_{season} is equal to 1.0 and $v_{b,0}$ is equal to 33.0m/s.

$$v_b = c_{dir} \cdot c_{season} \cdot v_{b,0} = 1.0 \cdot 1.0 \cdot 33.0m/s = 33.0m/s \tag{4-21}$$

The coefficient of roughness $c_{r(z)}$ is calculated as follows by Eq. (4-22) using Eq. 4-16 assuming both z_0 and $z_{0,II}$ equal to 0.05m.

$$c_{r(z)} = k_r \cdot ln\left(\frac{z}{z_0}\right) = 0.19 \cdot ln\left(\frac{3.45m}{0.05m}\right) = 0.804 \tag{4-22}$$

Where,

$$k_r = 0.19 \cdot \left(\frac{z_0}{z_{0.II}}\right)^{0.07} = 0.19 \cdot \left(\frac{0.05}{0.05}\right)^{0.07} = 0.19 \tag{4-23}$$

The average wind velocity $v_{m(z)}$ is calculated as follows by Eq. (4-24) using Eq. 4-15 assuming $c_{r(z)}$ equal to 0.804, $c_{0(z)}$ equalto 1.0 and v_b equal to 33.0m/s.

$$v_{m(z)} = c_{r(z)} \cdot c_{0(z)} \cdot v_b = 0.804 \cdot 1.0 \cdot 33.0m/s = 26.548m/s \tag{4-24}$$

The turbulence intensity $I_{v(z)}$ is calculated as follows by Eq. (4-25) using Eq. (4-13) assuming k_I equal to 1.0, $c_{0(z)}$ equal to 1.0 and z_0 equal to 0.05m.

$$I_{v(z)} = \frac{k_I}{c_{o(z)} \cdot \ln\left(\frac{z}{z_0}\right)} = \frac{1.0}{1.0 \cdot ln\left(\frac{3.45}{0.05}\right)} = 0.236 \tag{4-25}$$

Finally, the peak wind pressure is calculated as follows using Eq. (4-12) and the previously calculated turbulence intensity $I_{v(z)}$ (Eq. 4-25), average wind velocity $v_{m(z)}$ (Eq. 4-24) and air density ρ equal to 1.25kg/m^3.

$$q_{p(z)} = \left[1 + 7 \cdot I_{v(z)}\right] \cdot \frac{1}{2} \cdot \rho \cdot v_{m(z)}^2$$
$$= [1 + 7 \cdot 0.236] \cdot \frac{1}{2} \cdot 1.25 kg/m^3 \cdot 26.548^2 \, {m^2}/{s^2} = 1169 N/m^2 \tag{4-26}$$

In all wind cases, the shelter's exposed surface exceeds 10 m². Therefore, the external pressure coefficient $c_{pe,10}$, as defined in EN 1991-1-4, is used. For each wind direction, wind pressure zones and external pressure coefficients are identified for both the curved roof and the vertical walls. For wind in the X-direction, three wind pressure zones are found for the curved surface based on f/d=0.5. Similar zones are determined for the vertical walls, considering their shape. The external pressure coefficients for each zone A, B, C, A', B', C' used are 0.5, -1.2, -0.4, -1.2, -0.8, -0.5, respectively [15].

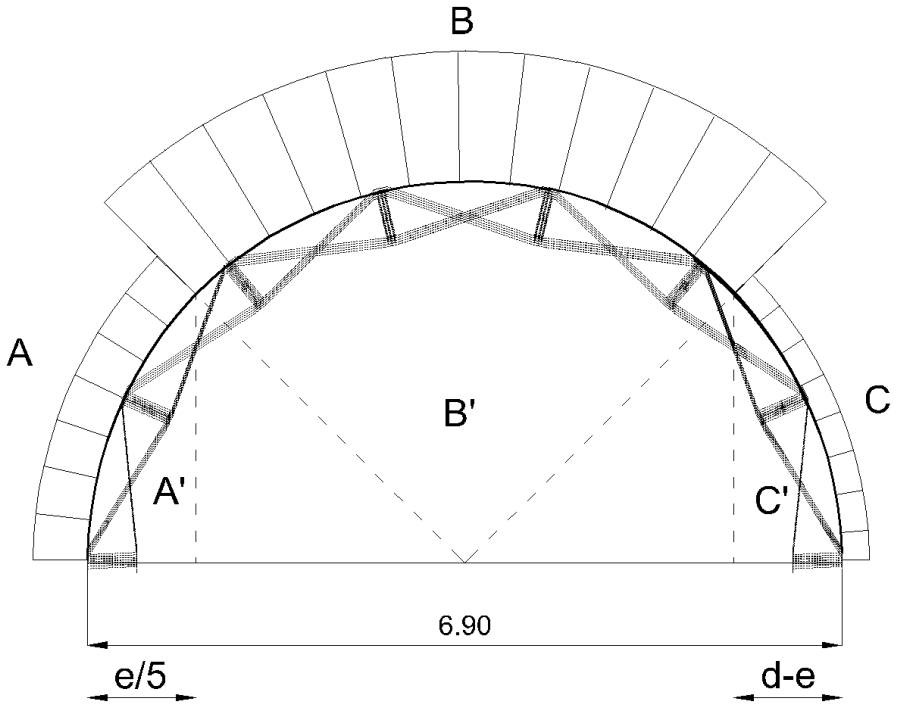

Figure 41. Wind pressure zones for the vaulted roof and vertical walls (transversal direction) [15].

For wind acting in the Y-direction, four wind pressure zones were identified on the curved surface of the shelter, based on the geometric parameters h = 3.45 m, d = 5.73 m, b = 6.90 m, and e = 6.90 m. For the vertical walls, considering that e > d and h/d = 0.60, two wind pressure zones were defined. The external pressure coefficients for each zone D, E, F, G, H, I used are 0.8, -0.4, -1.8, -2.0, -0.7, -0.2, respectively [15].

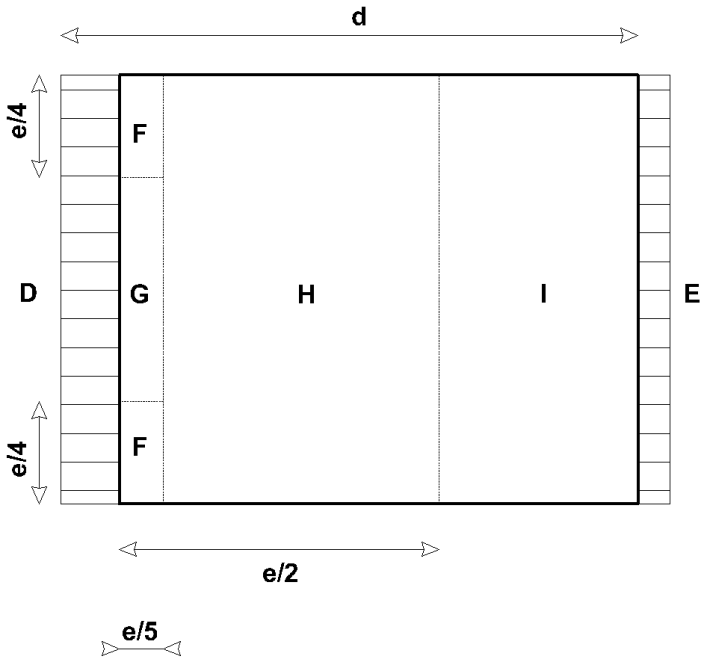

Figure 42. Wind pressure zones for the vaulted roof and vertical walls (longitudinal direction) [15].

Due to the uncertainty in the distribution of openings and the large number of possible load combinations, the internal pressure coefficients cpi were conservatively assumed as follows: $c_{pi} = -0.3$ for wind acting in the X-direction and $c_{pi} = 0.2$ for wind acting in the Y-direction. Based on Eq. (4-26), and for $q_{pe} = 1169$ N/m², the external and internal wind pressure values for each zone were calculated accordingly and are presented below [15].

Tab. 4-4. External wind pressure w_e (Pa).

Zone	c_{pe}	w_e
A	0.8	935
B	-1.2	-1402
C	-0.4	-467
A'	-1.2	-1402
B'	-0.8	-935
C'	-0.5	-584
D	0.8	935
E	-0.4	-467
F	-1.8	-2104
G	-2	-2337
H	-0.7	-818

I	-0.2	-234

Tab. 4-5. Internal wind pressure w_i (Pa).

Zone	c_{pe}	w_i
A	-0.3	-351
B	-0.3	-351
C	-0.3	-351
A'	-0.3	-351
B'	-0.3	-351
C'	-0.3	-351
D	0.2	234
E	0.2	234
F	0.2	234
G	0.2	234
H	0.2	234
I	0.2	234

The final wind pressures will be given by subtracting the internal from the external pressures as shown below in Tab. 4-6 [15].

Tab. 4-6. Final wind pressure w (Pa).

Zone	w_e	w_i	w
A	935	-351	1286
B	-1402	-351	-1052
C	-467	-351	-117
A'	-1402	-351	-1052
B'	-935	-351	-584
C'	-584	-351	-234
D	935	234	701
E	-467	234	-701
F	-2104	234	-2337
G	-2337	234	-2571
H	-818	234	-1052
I	-234	234	-467

The wind pressure was modelled by applying concentrated loads at the centroid of each joint, acting normal to the surface of the arch, following an appropriate distribution to the nearest nodes. Below depicted are the loads applied to the corresponding surfaces.

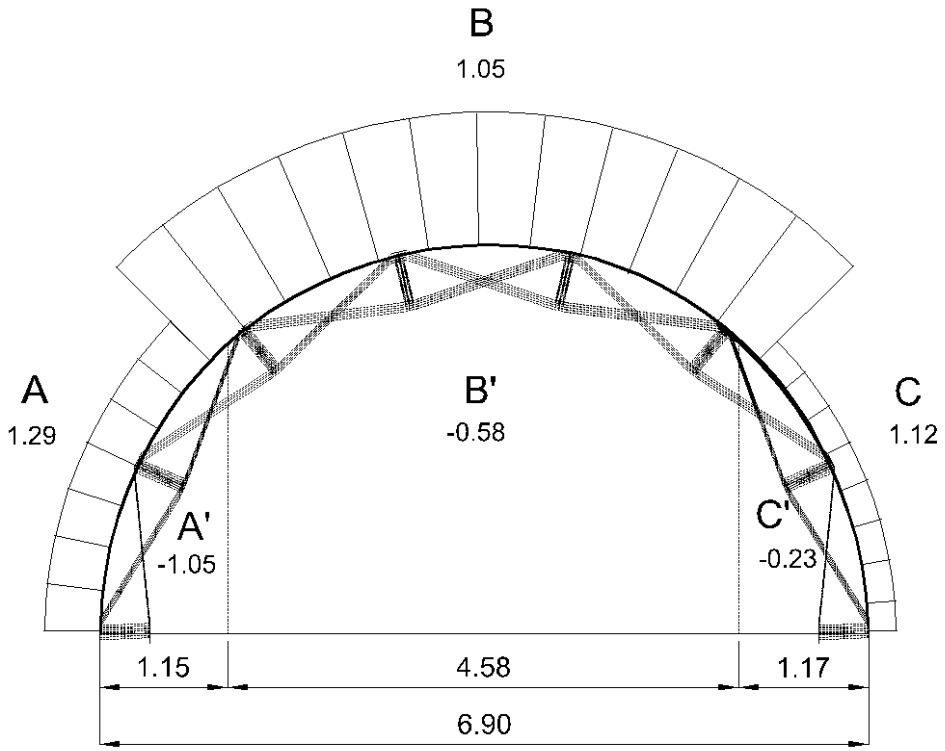

Figure 43. Transversal direction wind pressure in kN/m^2 to the vaulted and vertical surface areas.

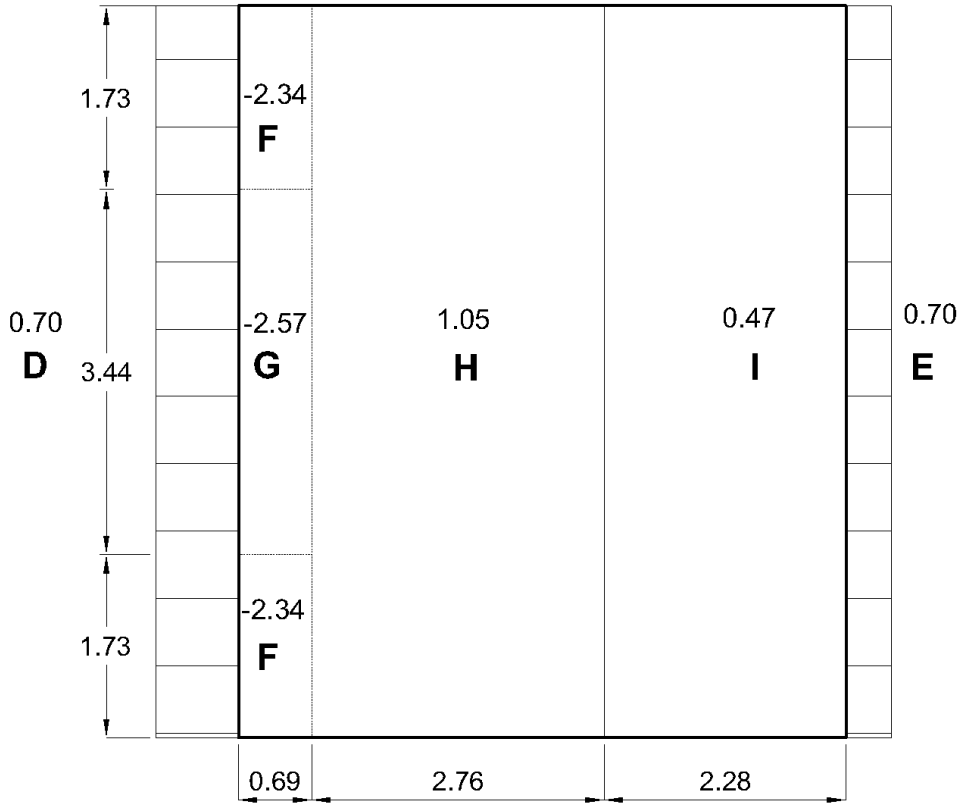

Figure 44. Longitudinal direction wind pressure in kN/m^2 to the vaulted and vertical surface areas.

4.3 Load combinations

The verification of structural adequacy is performed with respect to the limit states. Beyond these states, the structure no longer satisfies safety and serviceability requirements. Limit states are classified into ultimate limit states (ULS) and serviceability limit states (SLS). Ultimate limit states correspond to conditions that compromise the safety of the structure. These include loss of equilibrium, or partial or total collapse, which can pose a risk to human life. Serviceability limit states correspond to conditions that render the functional performance of the structure unsatisfactory. Examples include excessive deformations, damage to non-structural elements, undesirable cracking, or vibrations affecting user comfort. The characteristic values of the actions, as previously calculated, are multiplied by appropriate partial safety factors (γ). These are then combined using suitable combination factors (ψ) for ULS and SLS. The combinations are applied under the assumption that actions act simultaneously, resulting in the load combinations used for verification of ultimate and serviceability limit states.

4.3.1 Ultimate limit state (ULS)

For the verification at the ultimate limit state (ULS), the following load combinations are defined.

For persistent and transient design situations (Eq. 4-12), the actions are combined in accordance with the provisions of EN 1990 [16], taking into account the appropriate partial safety factors and combination coefficients.

$$\sum_{j\geq 1} \gamma_{G,j} \cdot G_{k.j} \text{ "+" } \gamma_p \cdot P \text{ "+" } \gamma_{Q,1} \cdot Q_{k,1} \text{ "+" } \sum_{i\geq 1} \gamma_{Q,i} \cdot \psi_{0,\iota} \cdot Q_{k,i} \tag{4-12}$$

For accidental design situations, the load combinations are defined according to EN 1990 [16] (Eq. 4-13), considering appropriate reduction factors for accompanying variable actions.

$$\sum_{j\geq 1} G_{k.j} \text{ "+" } P \text{ "+" } A_d \text{ "+" } \psi_{1,1} \cdot Q_{k,1} \text{ "+" } \sum_{i\geq 1} \psi_{2,i} \cdot Q_{k,i} \tag{4-13}$$

For seismic design situations, the load combinations are defined as following (Eq. 4-14).

$$\sum_{j\geq 1} G_{k.j} \text{ "+" } P \text{ "+" } A_{Ed} \text{ "+" } \sum_{i\geq 1} \psi_{2,i} \cdot Q_{k,i} \tag{4-14}$$

In the above expressions, the symbol "+" denotes combination with. $G_{k,j}$ represents the characteristic value of permanent actions, while P corresponds to the characteristic value of prestressing. $Q_{k,1}$ denotes the characteristic value of the leading variable action, and Qk,i denotes the characteristic values of the accompanying variable actions. A_d and A_{Ed} represent the design values of accidental and seismic actions, respectively. The factors $\gamma_{G,j}$, γ_P, and $\gamma_{Q,i}$ are the partial safety factors for permanent actions, prestressing, and variable actions, respectively, while $\psi_{0,i}$, $\psi_{1,i}$, and $\psi_{2,i}$ are the combination factors associated with variable actions.

4.3.2 Serviceability Limit State (SLS)

The design combinations defined for the verification at the serviceability limit state (SLS) are as follows:

For the characteristic combination, as defined by Eq. (4-15), the following expression applies.

$$\sum_{j\geq 1} G_{k.j} \text{ " + "} P \text{ " + "} Q_{k,1} \text{" + " } \sum_{i\geq 1} \psi_{0,i} \cdot Q_{k,i} \tag{4-15}$$

For the frequent combination, as defined by Eq. (4-16), the following expression applies.

$$\sum_{j\geq 1} G_{k.j} \text{ " + "} P \text{ " + "} \psi_{1,1} \cdot Q_{k,1} \text{" + " } \sum_{i\geq 1} \psi_{2,i} \cdot Q_{k,i} \tag{4-16}$$

For the quasi-permanent combination, as defined in Eq. (4-17).

$$\sum_{j\geq 1} G_{k.j} \text{ " + "} P \text{ " + " } \sum_{i\geq 1} \psi_{2,i} \cdot Q_{k,i} \tag{4-17}$$

4.3.3 Combination factors

The partial safety factors γ are defined according to Eurocode provisions. For ultimate limit states (ULS), $\gamma_G = 1.35$ is adopted for permanent actions with unfavourable effects and $\gamma_Q = 1.50$ for variable actions, while for favourable effects, $\gamma_G = 1.00$ and $\gamma_Q = 0.00$. For accidental actions, $\gamma_A = 1.00$ is considered.

For serviceability limit states (SLS), the partial factors are generally taken equal to 1.00 for unfavourable effects and 0.00 for favourable variable actions. The combination factors ψ for variable actions depend on the type of action and reflect the reduced probability of simultaneous occurrence.

For imposed loads in buildings, ψ_0 typically ranges between 0.7 and 1.0, while ψ1 and ψ_2 take lower values.

For snow loads, ψ_0 is commonly taken as 0.5, with $\psi_1 = 0.2$ and $\psi_2 = 0$. For wind actions, $\psi_0 = 0.6$, $\psi_1 = 0.2$, and $\psi_2 = 0$, whereas for temperature actions $\psi_0 = 0.6$, $\psi_1 = 0.5$, and $\psi_2 = 0$.

These values are used for the formulation of load combinations in both ultimate and serviceability limit state verifications.

4.3.4 Load combinations

The following tables, Tab. (3-2) and (3-3), depict the 12 combinations selected for study based on similar studies [15]. The structure is assumed to be located at an altitude of under 1000 m. As a result of the considered live loads of snow and wind, the coefficients will be given from the following Tab. 3-1.

Table 3-1. Combination factors for live loads.

Type of load	ψ_0	ψ_1	ψ_2
Snow loads	0.5	0.2	0
Wind loads	0.6	0.5	0

In the following tables Tab. (3-2) and (3-3) , SW (Self Weight) represents the load due to the self-weight of the structure, SSL (Symmetrical Snow Load) corresponds to the non-drifted snow load, and DSL (Drifted Snow Load) refers to the drifted snow load. TWL (Transverse Wind Load) denotes the wind load acting in the transverse direction (X-axis), while LWL (Longitudinal Wind Load) represents the wind load in the longitudinal direction (Y-axis). The above load combinations were derived assuming unfavorable effects for both permanent and variable actions. Considering all possible combinations of favorable and unfavorable effects results in a total of 96 load combinations for both ultimate and serviceability limit states. However, due to the complexity associated with the implementation of these loads in the numerical model, only the combinations described above were taken into account.

Table 3-2. Load combinations for the Ultimate Limit State including the corresponding safety factors.

	SW	SSL	DSL	TWL	LWL
ULS_LC1	1.35 X 1.0	1.50 X 1.0	-	-	-
ULS_LC2	1.35 X 1.0	-	1.50 X 1.0	-	-
ULS_LC3	1.35 X 1.0	-	-	1.50 X 1.0	-
ULS_LC4	1.35 X 1.0	-	-	-	1.50 X 1.0
ULS_LC5	1.35 X 1.0	-	1.50 X 0.5	1.50 X 1.0	-
ULS_LC6	1.35 X 1.0	-	1.50 X 0.5	-	1.50 X 1.0
ULS_LC7	1.35 X 1.0	-	1.50 X 1.0	1.50 X 0.6	-
ULS_LC8	1.35 X 1.0	-	1.50 X 1.0	-	1.50 X 0.6
ULS_LC9	1.35 X 1.0	1.50 X 1.0	-	1.50 X 0.6	-
ULS_LC10	1.35 X 1.0	1.50 X 1.0	-	-	1.50 X 0.6
ULS_LC11	1.35 X 1.0	1.50 X 0.5	-	1.50 X 1.0	-
ULS_LC12	1.35 X 1.0	1.50 X 0.5	-	-	1.50 X 1.0

Table 3-3. Load combnations for the Ultimate Limit State including the corresponding safety factors.

	SW	SSL	DSL	TWL	LWL
SLS_LC1	1.00 X 1.0	1.00 X 1.0	-	-	-
SLS_LC2	1.00 X 1.0	-	1.00 X 1.0	-	-
SLS_LC3	1.00 X 1.0	-	-	1.00 X 1.0	-
SLS_LC4	1.00 X 1.0	-	-	-	1.00 X 1.0
SLS_LC5	1.00 X 1.0	-	1.00 X 0.5	1.00 X 1.0	-
SLS_LC6	1.00 X 1.0	-	1.00 X 0.5	-	1.00 X 1.0
SLS_LC7	1.00 X 1.0	-	1.00 X 1.0	1.00 X 0.6	-
SLS_LC8	1.00 X 1.0	-	1.00 X 1.0	-	1.00 X 0.6
SLS_LC9	1.00 X 1.0	1.00 X 1.0	-	1.00 X 0.6	-
SLS_LC10	1.00 X 1.0	1.00 X 1.0	-	-	1.00 X 0.6
SLS_LC11	1.00 X 1.0	1.00 X 0.5	-	1.00 X 1.0	-
SLS_LC12	1.00 X 1.0	1.00 X 0.5	-	-	1.00 X 1.0

5 NUMERICAL MODELING OF THE STRUCTURE

5.1 General

The finite element method in deployable structures is used to simulate scissor-like elements, capturing both the elastic deformation of the members and the rigid-body motion related to deployment. Two straight rods joined by a central hinge make up a typical two-dimensional scissor unit. Each rod is split into two beam elements in the finite element formulation, creating a four-element model that faithfully captures axial and bending effects. The governing equations for each beam element are expressed through equilibrium, compatibility, and flexibility relations according to Prof. Pellegrino's book chapter on the finite element simulation of deployable structures [19],

$$\boldsymbol{Bf} = \begin{bmatrix} -1 & 0 & 0 \\ 0 & {}^{-1}/_{L_i} & {}^{1}/_{L_i} \\ 0 & -1 & 0 \\ 1 & 0 & 0 \\ 0 & {}^{1}/_{L_i} & {}^{-1}/_{L_i} \\ 0 & 0 & 1 \end{bmatrix} \begin{bmatrix} T_i \\ M_1 \\ M_2 \end{bmatrix} = \boldsymbol{p} \tag{5-1}$$

Where, Ti is defined as the axial force and M1, M2 are the bending moments at the element ends. The compatibility relation is expressed as:

$$\boldsymbol{B^T u} = \boldsymbol{\eta} \tag{5-2}$$

and the flexibility relation becomes,

$$\boldsymbol{\eta} = \begin{bmatrix} \frac{L}{AE} & 0 & 0 \\ 0 & \frac{L}{3EI} & \frac{L}{6EI} \\ 0 & \frac{L}{6EI} & \frac{L}{3EI} \end{bmatrix} \boldsymbol{f} \tag{5-3}$$

These equations are transformed into the global coordinate system using the rotation matrix,

$$\boldsymbol{B_g = RB} \tag{5-2}$$

before assembling all four beam elements into a global finite-element model of the scissor unit. This formulation allows the simulation of large rotational deployment of the scissor-like element while accounting for bending flexibility, axial deformation, and hinge compatibility, which are essential features of deployable structures. Since these equations are written for a single beam element, they do not depend on how many elements are present into the SLE. For the structure studied in this thesis the addition of an element only affects the size of the global vectors, the size of the assembled matrices as well as the number of compatibility constraints.

The development of the geometrical model in order to conduct finite element analysis involved integrating the previously calculated geometry into the RFEM 6 [20] software environment. The purpose of this integration was to conduct several types of analyses, including linear static, modal, and buckling analyses, to develop approaches for designing the structural members. The ultimate goal was to obtain the final geometry of both polar and translational members in order to generate the optimal geometry for the joint that connects them. All analysis phases adopted the assumption that the joints are rigid, allowing the analysis to focus on the stresses and forces generated in the members.

5.1.1 Geometrical design of the numerical model

As mentioned above, the geometrical design of the model was strictly based on the geometry obtained through the generation process. The problem in this case was that the ideal geometry generated above considered both polar and translational members connected at the same point in the joint. However, this is not the case in this model. The purpose of this thesis is to develop a joint without eccentricity as mentioned above. For this purpose, the proposed joint geometry of the initial joint assumption for the linear elements for the case of a single-SLE system vs the double-SLE system is depicted below in Fig.40.

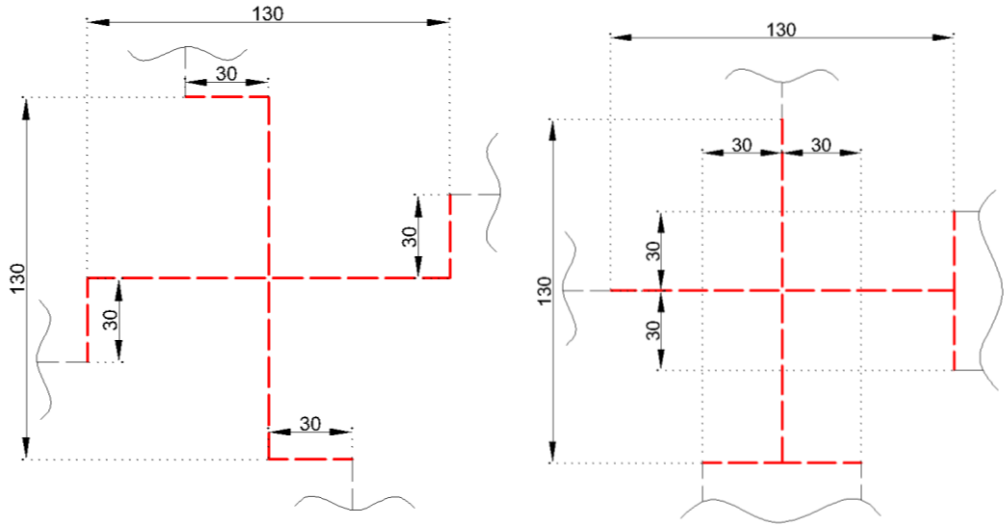

(a) **(b)**

Figure 45. Joint configuration in the finite element model using rigid elements (red) for (a) single and (b) double SLE configurations.

A sufficient distance to fit two structural members, since in similar studies, the distance of 20mm [15] was adopted, a little more than double that of 60mm was adopted for this case. The same assumption is used for the core joint length and width, where 130mm length and width were adopted. As seen in Fig., the CAD design was integrated into the RFEM 6 environment using linear elements for both polar and translational members and rigid elements for the joints.

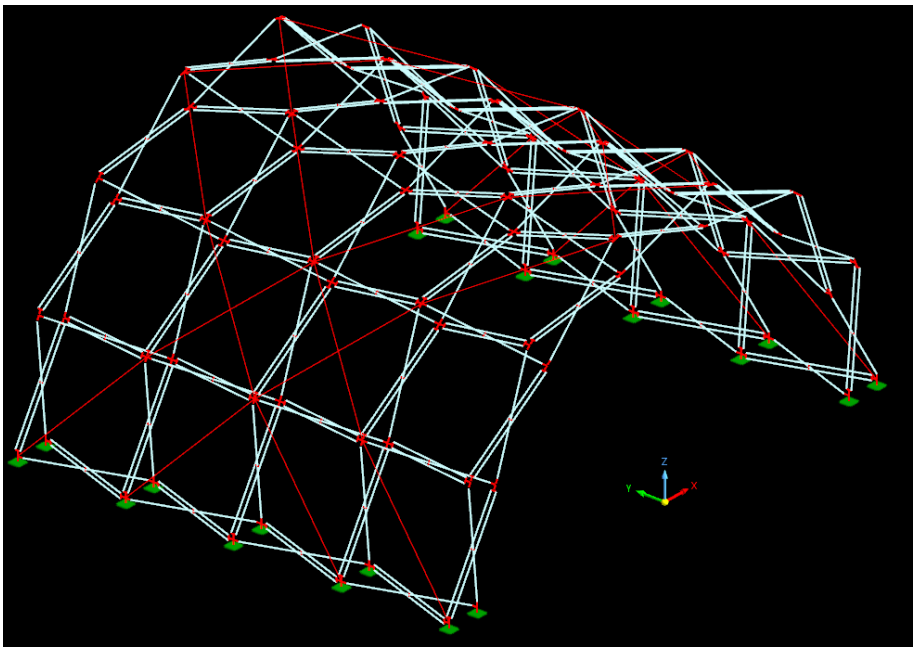

Figure 46. Finite element model of the structure developed in RFEM 6.

5.1.2 Structural members

As of the initial assumption for the cross-section of the members, four different cross-sections should be assumed at first. The first two will consist of the polar single-member cross section and the polar double-member cross section, while the other two will consist of the translational single-member cross section and the corresponding double-member cross section. All the members were implemented in the model as linear beam elements with equal length for all the members. The cross sections selected are displayed in Fig. and correspond to a maximum section class 3 according to EN 1993 [21] in order to avoid local buckling phenomena.

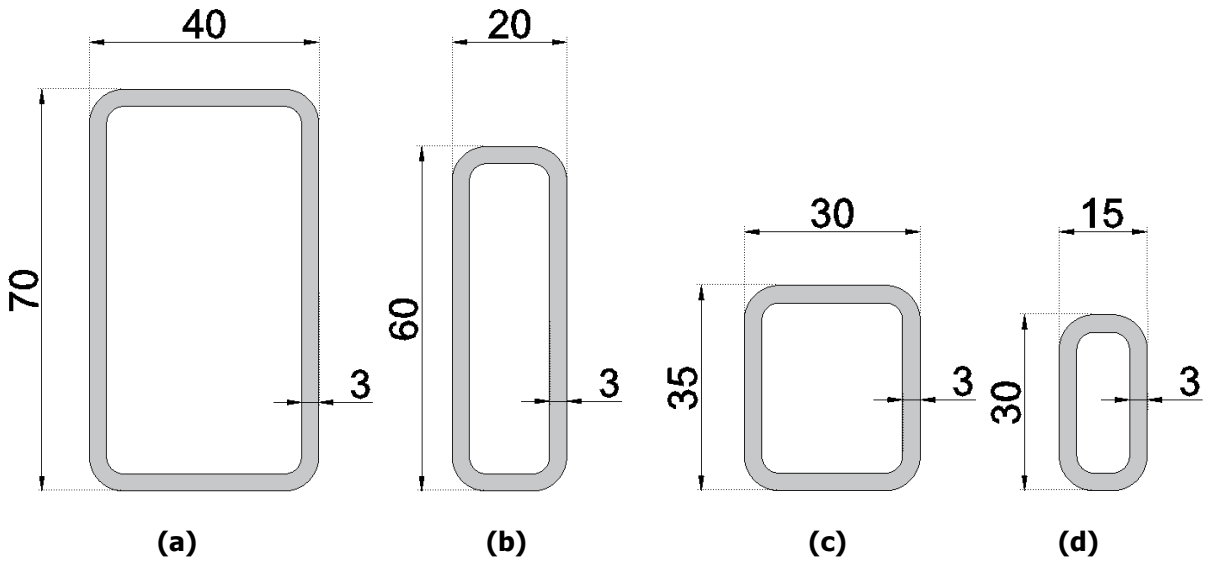

Figure 47. Initial cross-section assumptions for the polar single-member (a), polar double-member (b), translational single-member (c), and translational double-member (d) elements.

Aluminium was selected as the primary material for all members of the scissor-like elements in the numerical model of the shelter. This choice was mainly driven by its low weight compared to other structural materials typically used in load-bearing systems, allowing for the development of a lightweight structure that facilitates transportation and rapid deployment. Aluminium is available in various alloys, whose mechanical and physical properties depend on their chemical composition and manufacturing processes. Among the wrought aluminium alloys commonly used in structural applications is EN AW-6063, an aluminium–silicon–magnesium alloy. This alloy is typically strengthened through heat treatment, involving solution heat treatment followed by artificial ageing in the T6 condition. The properties of the selected aluminum alloy according to EN 1999 are given below in Tab.

Table 5-1. Mechanical properties of aluminium alloy EN AW-6063-T6

Alloy EN-AW	Product type	Temper	Thickness t (mm)	f_o (N/mm^2)	f_u (N/mm^2)	BC	n_p	E (GPa)	G (GPa)
6063	ET	T6	t≤25	160	195	A	24	70	27

Where, EN AW denotes the aluminium alloy designation according to European standards; Product Type refers to the form of the material (e.g., extruded products, ET), temper indicates the heat treatment condition of the alloy (e.g., T6), t is the material thickness, f_0 is the 0.2% proof strength, f_u is the ultimate tensile strength, BC denotes the buckling class according to Eurocode 9, and n_p is the strain hardening parameter used for design calculations.

Since the joints will not be able to lock in a specific place, a stiffening system consisting of stainless steel cables was introduced, modelled, and designed. The cable selected as an initial assumption has a diameter of 6.1mm and a modulus of elasticity equal to 130GPa and consists of 19 ropes that create a cross-section with an area of 22mm^2. The maximum tensile force that it can obtain is up to 16 kN, and the cross-section is depicted below in Fig.43.

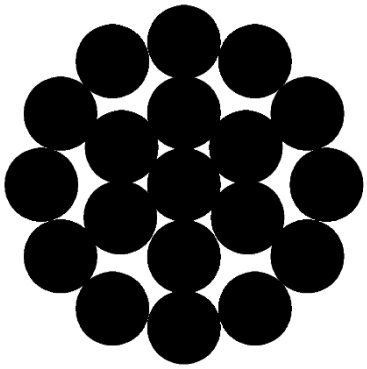

Figure 48. Cross section of the stiffening cable.

Their ends coincide with the centroid of the connected joints. In the numerical model, the cables were simulated as truss elements with zero compressive capacity and tensile resistance equal to the yield strength specified by the manufacturer. In practice, the function of this stiffening system could potentially be replaced by the membrane covering of the shelter [15]. The cables were arranged according to the configuration shown in Fig.44.

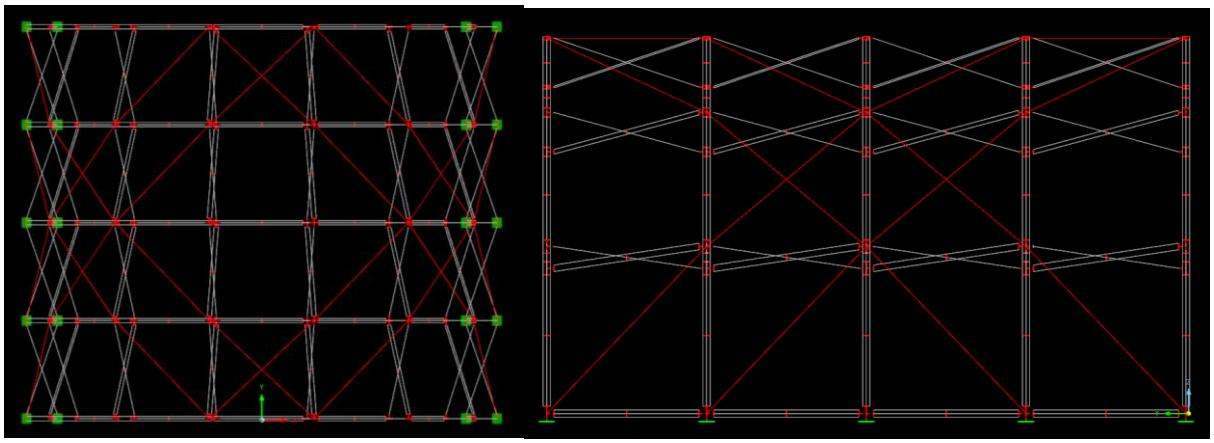

Figure 49. Bracing system of the structure highlighted in red, shown in top and side views.

5.1.3 Modelling of joints and connections.

The bolted connection between the members and the joints was modelled assuming that all relative displacements between member and joint were restrained, except for the relative rotation about the axis perpendicular to the plane of each scissor-like element. Thus, following the modelling of the rigid joint, rotational freedom about the local y-axis was assigned at the end of each member as shown in Fig.45.

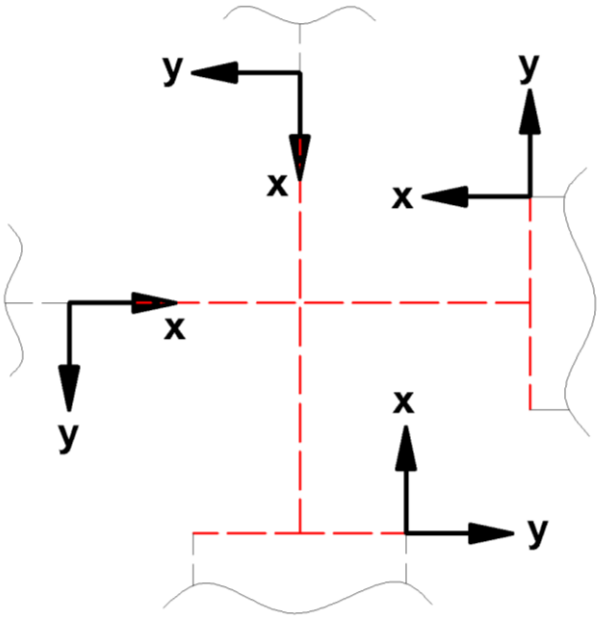

Figure 50. Rigid joint elements with local element axes.

To model the rotational point of each double scissor-like element, all relative displacements between the two opposing intermediate points of the members were restrained, except for the relative rotation about the x-axis, which is perpendicular to the plane defined by each pair of members, as shown in Fig.46.

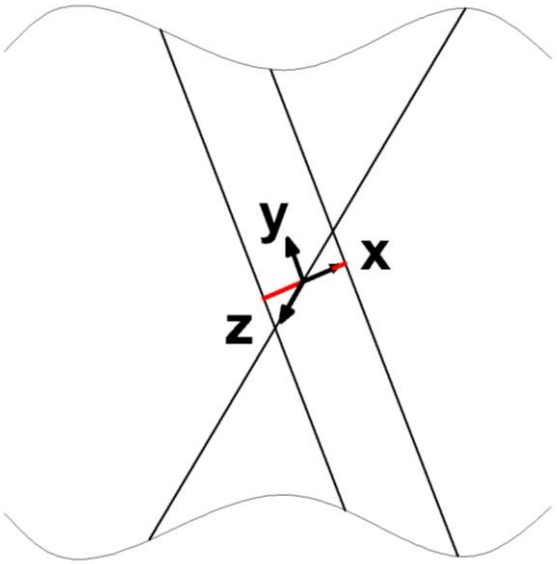

Figure 51. Intermediate pivot point of a double scissor-like element with local axes.

5.1.4 Actions applied to the structure

The structural loading was applied based on the permanent and variable actions calculated previously. Snow and wind surface loads, along with the self-weight of the membrane covering, were represented as concentrated forces acting at the centroids of the external joints of the shelter. The magnitude of

these forces was determined by distributing the load acting on each surface equally among its corresponding nodes. The direction of each force followed the respective loading condition, with snow loads acting in the direction of gravity and wind loads applied normal to the surface of the shelter. The self-weight of the joints and bolts was similarly introduced as concentrated loads acting at the centroid of each joint in the direction of gravity, while the self-weight of the members was automatically calculated by the software according to the geometric characteristics of their cross-sections.

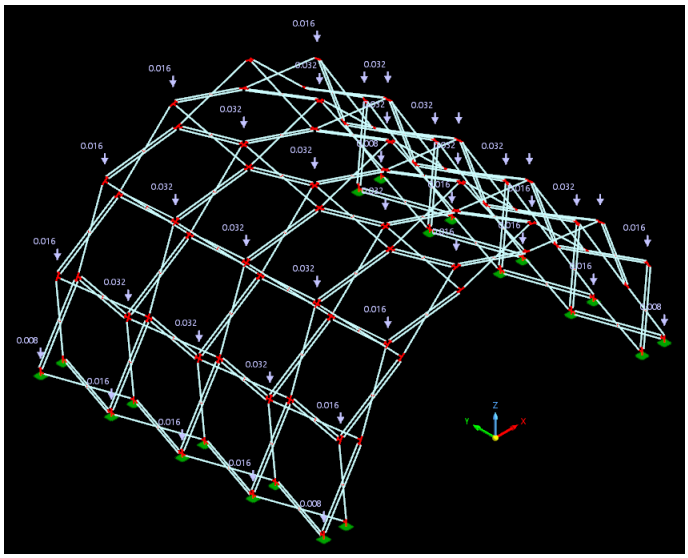

(a)

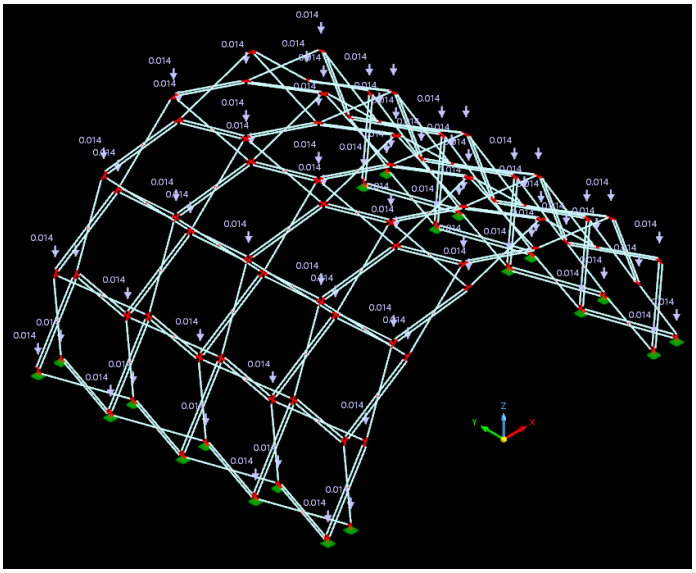

(b)

Figure 52. Self-weight of the joints (a) and membrane covering (b) applied to the numerical model.

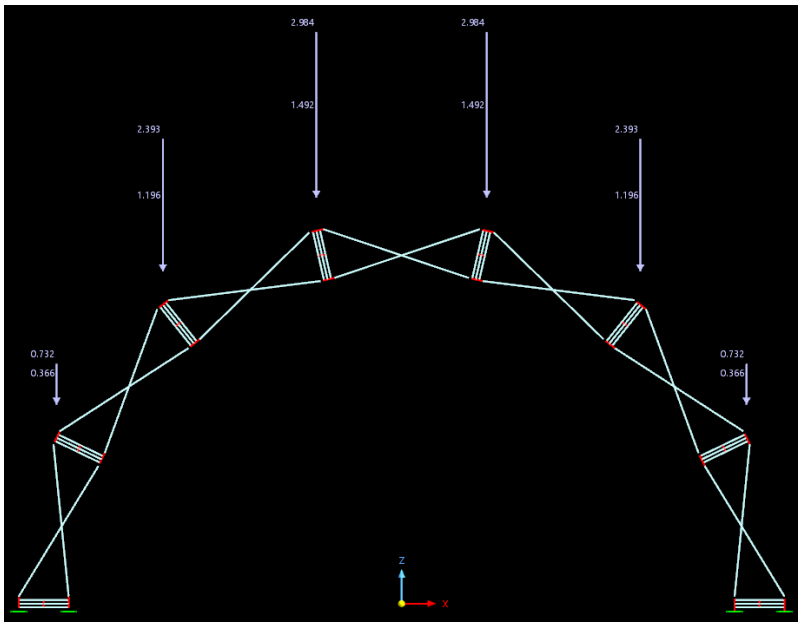

(a)

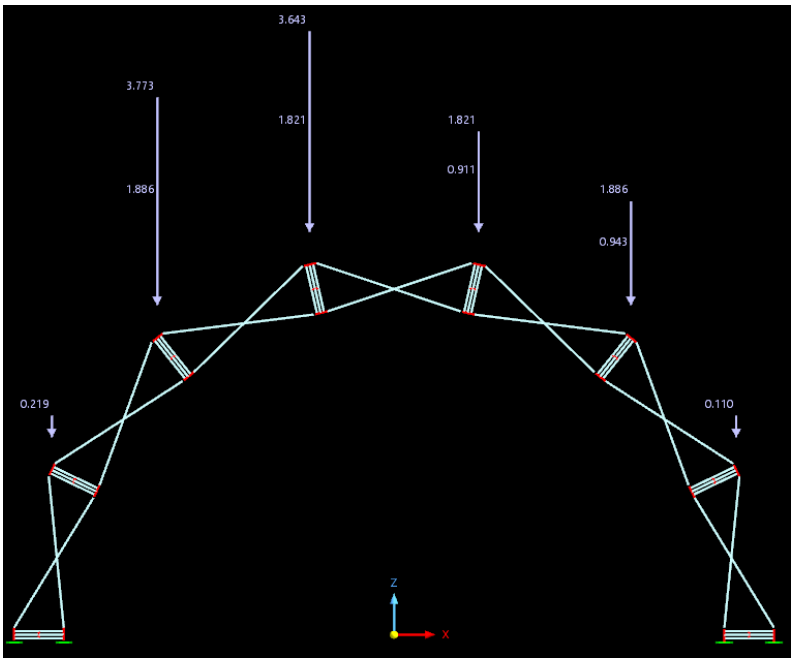

(b)

Figure 53. Symmetrical (a) and drifted (b) snow loads applied to the numerical model.

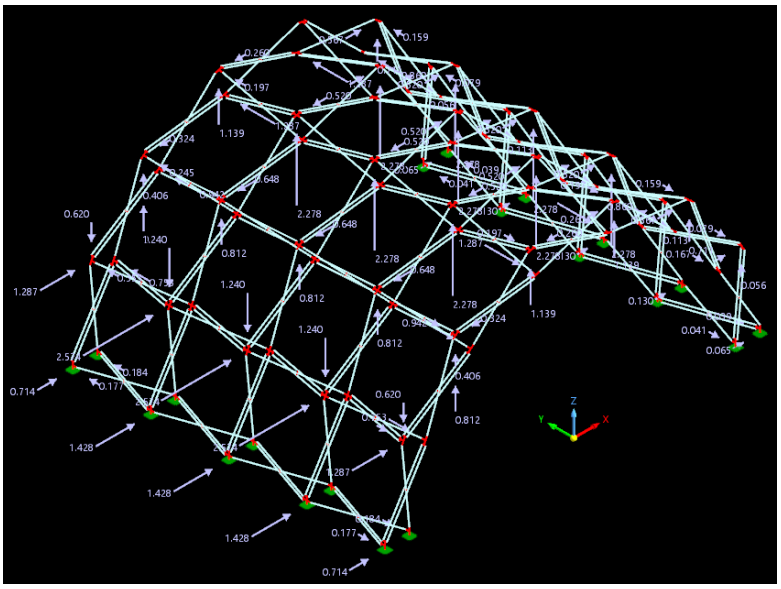

(a)

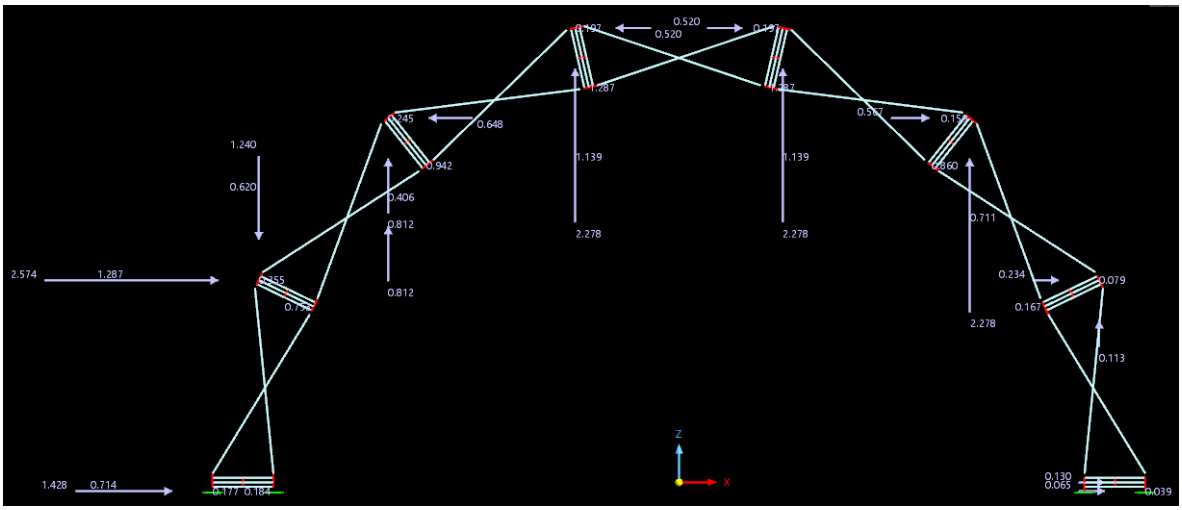

(b)

Figure 54. Transversal wind load: (a) axonometric view and (b) front view, showing the loads applied to the vaulted roof.

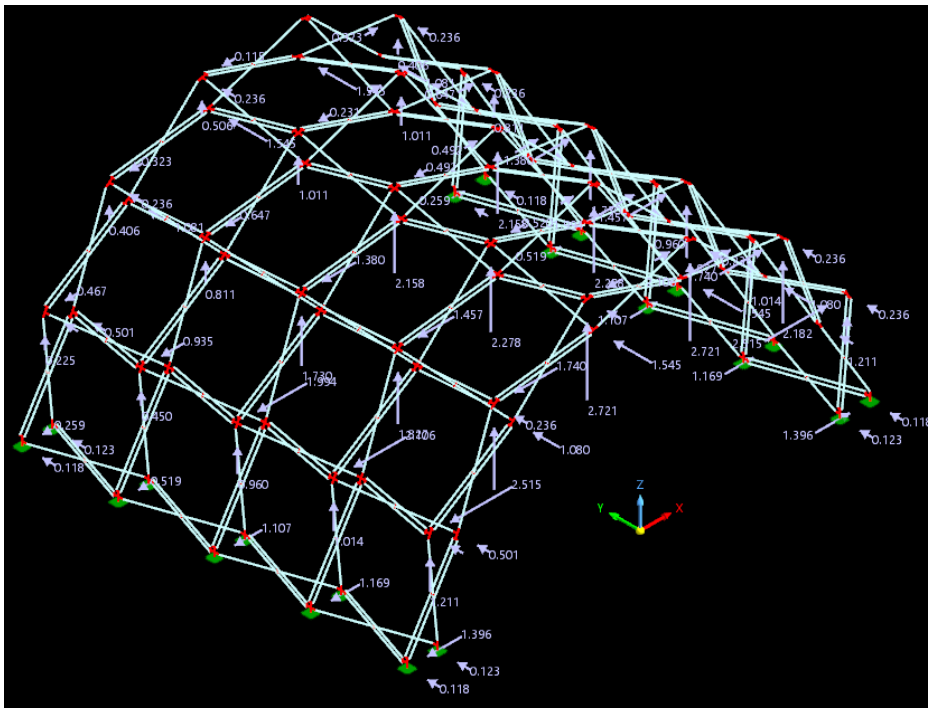

(a)

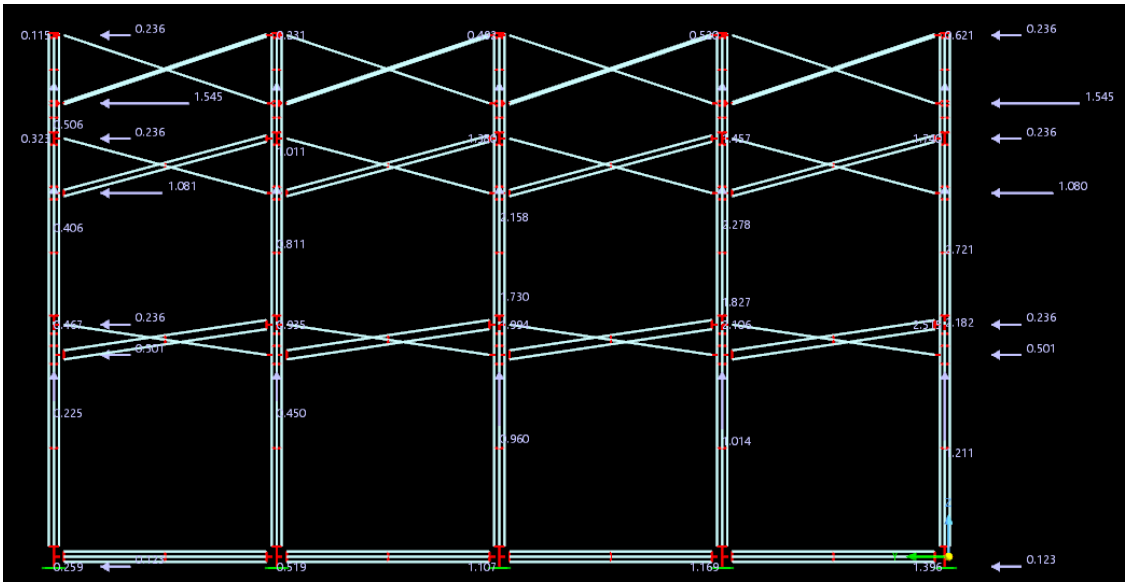

(b)

Figure 55. Longitudinal wind load: (a) axonometric view and (b) sode view, showing the loads applied to the vaulted roof.

5.2 Types of Analysis

The initial numerical model was first developed and loaded according to the twelve load combinations defined for both the ultimate and serviceability limit states, where each combination was analysed separately. The process followed is described as follows. Initially, preliminary cross-sections were selected for the members of the polar and translational scissor-like elements, and linear material and geometric analyses were carried out for all ultimate limit state combinations. The members were then

dimensioned by evaluating stresses using the von Mises criterion, ensuring global stability against buckling, and preventing local buckling by selecting Class 1, 2, or 3 cross-sections, while also verifying the serviceability limit state requirements. Subsequently, the design of the elements was conducted using both the influence of initial imperfections on the structural response, which was examined through geometrically nonlinear analyses with imperfections (GNIA) and the embedded designer of RFEM 6 according to EN1999. Finally, the joint and inal hole configuration of the members was designed as well according to EN 1993 and EN 1999.

5.2.1 Linear analysis

5.2.1.1 Structural design criteria

For the strength verification of the members, and considering that the structure is required to respond elastically under ultimate loading conditions, the von Mises yield criterion was adopted as the failure criterion. According to this criterion, yielding of a ductile material subjected to a multiaxial stress state occurs when the distortional strain energy reaches the corresponding value associated with yielding under uniaxial tension. The mathematical expression of the von Mises criterion, in terms of normal and shear stresses expressed in the global coordinate system xyz, is given as follows:

$$\sigma_{VM} = \sqrt{\left[\frac{1}{2}\cdot\left(\sigma_{xx}-\sigma_{yy}\right)^2+\left(\sigma_{yy}-\sigma_{zz}\right)^2+(\sigma_{zz}-\sigma_{xx})^2\right]+3\cdot\left(\tau_{xy}^2+\tau_{yz}^2+\tau_{xz}^2\right)} \quad (5\text{-}4)$$

While this criterion governs the ultimate limit state verification, the serviceability limit state is evaluated using the limits defined below. These limits are considered adequate, given that the structure does not present significant serviceability demands. The limits are depicted below in Tab. 5-2.

Table 5-2. Serviceability deformation limits adopted for the structure.

Vertical deformations limit (w)	Horizontal deformations limit (u)
L/200	H/200

Where the calculation of these limits is as follows, according to the calculated length L and height H of the structure in Chapter 3.

$$w = \frac{L}{200} = \frac{5.72m}{200} = 29mm \quad (5\text{-}5)$$

$$u = \frac{H}{200} = \frac{3.45m}{200} = 17mm \quad (5\text{-}6)$$

5.2.1.2 Internal forces in members

Table 5-3 presents the maximum von Mises stresses identified for each of the five member types of the structure under all load combinations. Based on the corresponding utilisation ratios, the most critical load combinations were determined as follows. For the polar single-member scissor-like elements, the governing load combination is ULS_LC3, with a utilisation ratio of 0.96, where only the transverse wind load (X-direction) is considered as the variable action. For the polar double-member scissor-like elements, the governing load combination is ULS_LC10, with an utilisation ratio of 0.83, where the symmetrical snow load and lomngitudinal wind load (Y-direction) are considered as the variable action. For the translational single-member scissor-like elements, the most unfavourable combinations are ULS_LC5 and ULS_LC3, with utilisation ratios of 0.51 and 0.52, respectively. In load combination ULS_LC5, the transverse wind load is considered as the leading variable action, while the drifted snow load is taken as accompanying. For the translational double-member scissor-like elements, the most unfavourable combinations are ULS_LC8 and ULS_LC10, with utilisation ratios of 0.72 and 0.56, respectively. In these combinations, the longitudinal wind load is considered as the leading variable action, while the symmetrical and drifted snow load is taken as accompanying, respectively.

For the bracing members, the critical load combination is ULS_LC6, with a utilisation ratio of 0.50, where the longitudinal wind load (Y-direction) is the leading variable action and the drifted snow load is the accompanying action. Similar utilisation ratios were obtained for load combination ULS_LC12 (0.48), where the longitudinal wind load remains the leading action, and the non-drifted snow load is considered as accompanying.

Table 5-3. Von Mises stresses for each member type.

	Polar SLEs				**Translational SLEs**				**Bracings (cables)**	
	Single		**Double**		**Single**		**Double**			
Load Combination	Max. V.Mises (MPa)	Ratio	Max. V.Mises (MPa)	Ratio	Max. V.Mises (MPa)	Ratio	Max. V.Mises (MPa)	Ratio	Max. V.Mises (MPa)	Ratio
ULS_LC1	121.96	**0.76**	115.9	**0.72**	55.86	**0.3**	69.59	**0.38**	20.18	**0.04**
ULS_LC2	108.9	**0.68**	123.44	**0.77**	84.24	**0.46**	98.03	**0.53**	74.75	**0.15**
ULS_LC3	152.91	**0.96**	104.31	**0.65**	96.25	**0.52**	90.2	**0.49**	103.85	**0.21**
ULS_LC4	49.51	**0.31**	59.86	**0.37**	40.92	**0.22**	72.57	**0.39**	228.04	**0.46**
ULS_LC5	114.9	**0.72**	68.71	**0.43**	94.35	**0.51**	93.13	**0.5**	94.08	**0.19**
ULS_LC6	73.57	**0.46**	94.87	**0.59**	56.04	**0.30**	95.66	**0.52**	249.11	**0.50**
ULS_LC7	85.85	**0.54**	91.54	**0.57**	66.86	**0.36**	73.25	**0.40**	73.79	**0.15**
ULS_LC8	101.12	**0.63**	141.76	**0.89**	85.59	**0.46**	132.33	**0.72**	181.39	**0.36**
ULS_LC9	62.35	**0.39**	84.16	**0.53**	41.53	**0.22**	53.97	**0.29**	30.54	**0.06**
ULS_LC10	132.58	**0.83**	133.4	**0.83**	62.8	**0.34**	102.9	**0.56**	160.71	**0.32**
ULS_LC11	104.64	**0.65**	63.84	**0.4**	81.1	**0.44**	78.97	**0.43**	83.38	**0.17**
ULS_LC12	86.49	**0.54**	89.36	**0.56**	54.29	**0.29**	91.89	**0.5**	239.77	**0.48**

As illustrated in the axial forces diagram (Fig.51), most of the arches are subjected to tensile forces, with the maximum tensile force of 10.61 kN occurring at the external support of the first polar scissor-like element on the windward side of the shelter. Compressive axial forces are also developed in the same region, particularly in the members connected to joints directly affected by wind pressure. The maximum compressive force is observed at the internal support of the same scissor-like element, with a value of 6.86 kN.

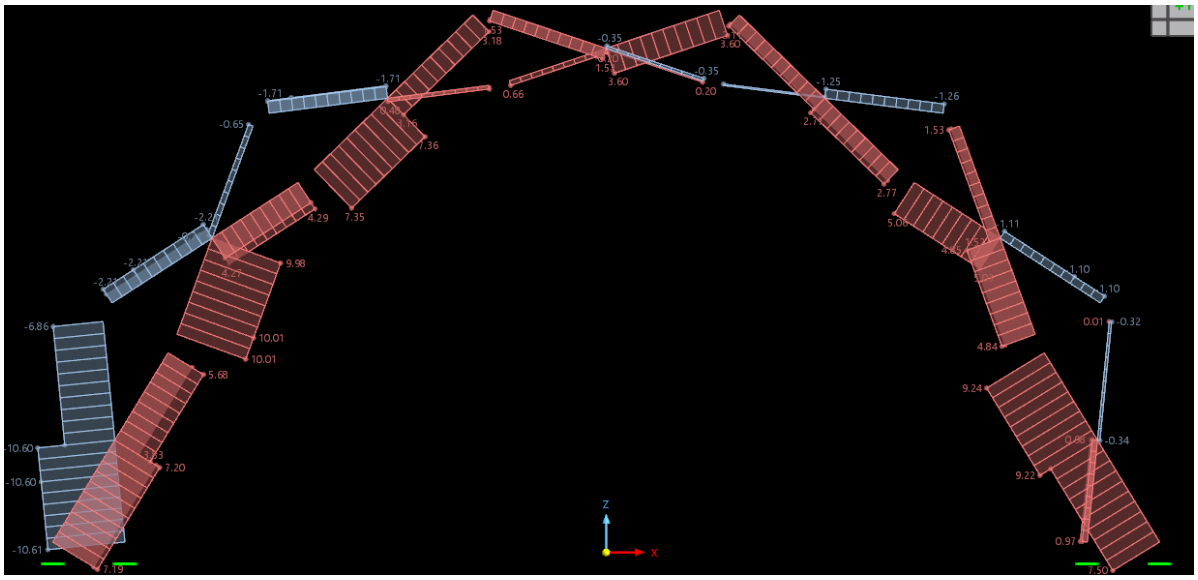

Figure 56. Axial force diagram for the third arch of the structure (ULS_LC3).

Fig.52 illustrates the in-plane bending moments of the scissor-like elements of the second arch. Notably, the moment diagrams highlight the hinged behaviour at the ends of the elements, as bending moments reduce to zero at the hinge locations. Additionally, maximum bending moments occur at the rotation pivots of the scissor-like elements. Specifically, the largest bending moment, equal to 1.27 kNm, is identified in the second scissor-like element at the location where the maximum von Mises stress is also recorded. This bending moment represents the governing internal action, as the corresponding normal stress reaches approximately 82% of the total von Mises stress (134.66 MPa). Overall, higher bending moments are observed on the windward side of the shelter, while lower values appear on the leeward side.

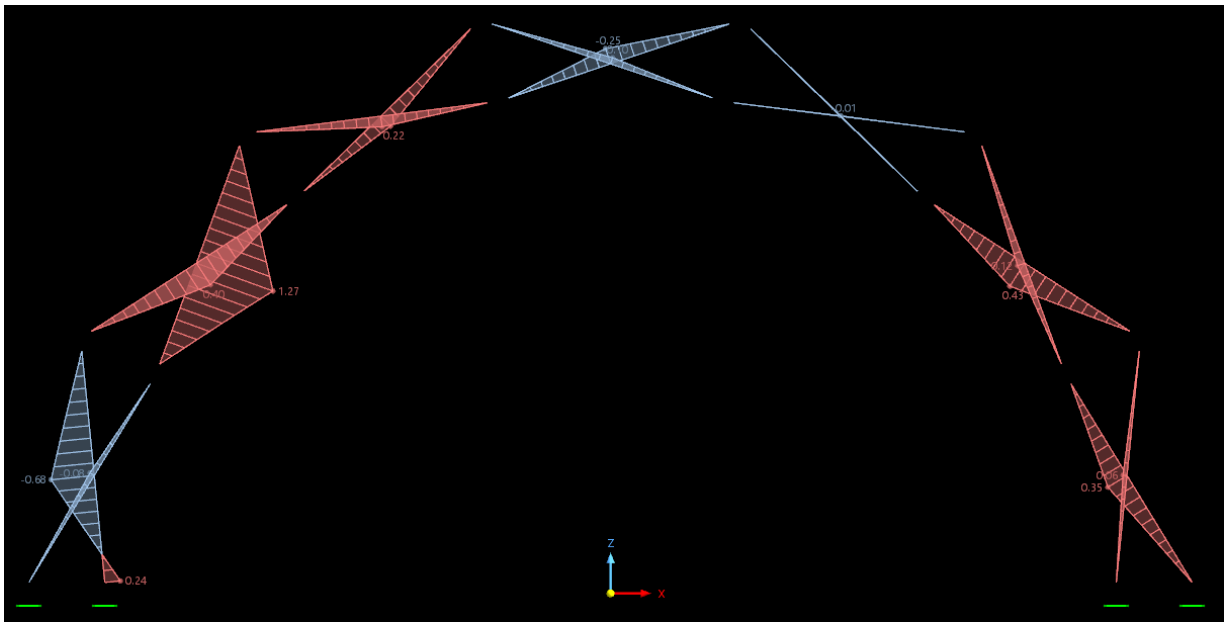

Figure 57. Bending moment diagram for the second arch of the structure (ULS_LC3).

As shown in Fig.53, the in-plane shear force distribution of the scissor-like elements, and consequently of the arch, exhibits a trend comparable to that observed in the bending moment diagrams. The highest shear forces, reaching 2.04 kN and 3.05 kN, are concentrated in the members of the critical scissor-like element. Overall, the most significant shear demand is observed on the windward side of the shelter, while lower values are recorded on the leeward side.

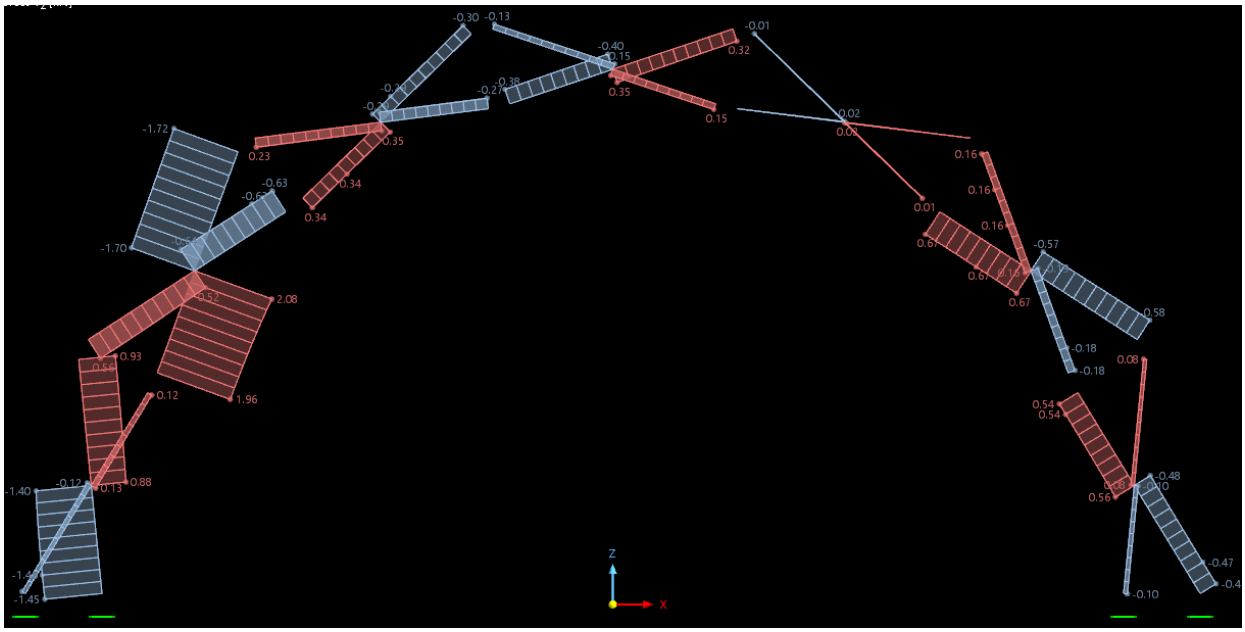

Figure 58. Shear force diagram for the second arch of the structure (ULS_LC3).

For the translational scissor-like elements subjected to the longitudinal wind load combination ULS_LC6, the axial force distribution (Fig.) indicates that the majority of the members are primarily subjected to compressive forces, with a peak value of 2.62 kN occurring in the elements located on the windward

side of the structure. Tensile axial forces develop in adjacent members, particularly near the supports and in regions directly influenced by the applied wind loads, with a magnitude of -1.60kN. Overall, the magnitude of the axial forces remains within acceptable limits, confirming the adequate performance of the translational members under longitudinal wind loading.

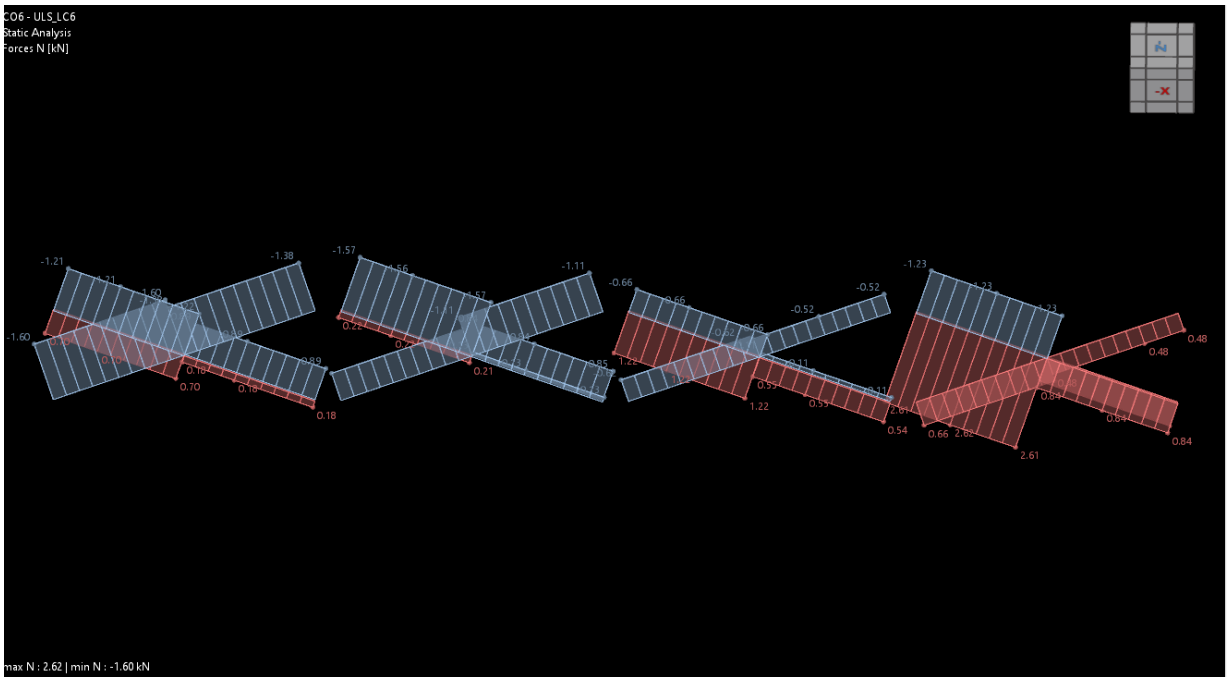

Figure 59. Shear force diagram for the third translational member set of the structure (ULS_LC6).

The in-plane bending moment diagrams for the translational members under load combination ULS_LC6 exhibit behaviour consistent with the hinged configuration of the scissor-like elements, with bending moments diminishing at the hinge locations. Maximum bending moments occur near the intermediate pivot points of the translational elements, with the highest values concentrated on the windward side of the structure. These moments remain within the elastic range of the material and do not govern the design. Fig.55 illustrates the in-plane bending moments of the translational scissor-like elements of the first arch. The distribution follows a pattern similar to that of the polar SLEs, with peak bending moments occurring at the intermediate connection of each scissor-like element and nearly zero values at the ends. The maximum bending moment, equal to 0.07 kNm, is identified in the second element at the location corresponding to the maximum von Mises stress, contributing notably to its magnitude. As observed for the polar SLEs, the highest bending moments are concentrated on the windward side of the shelter.

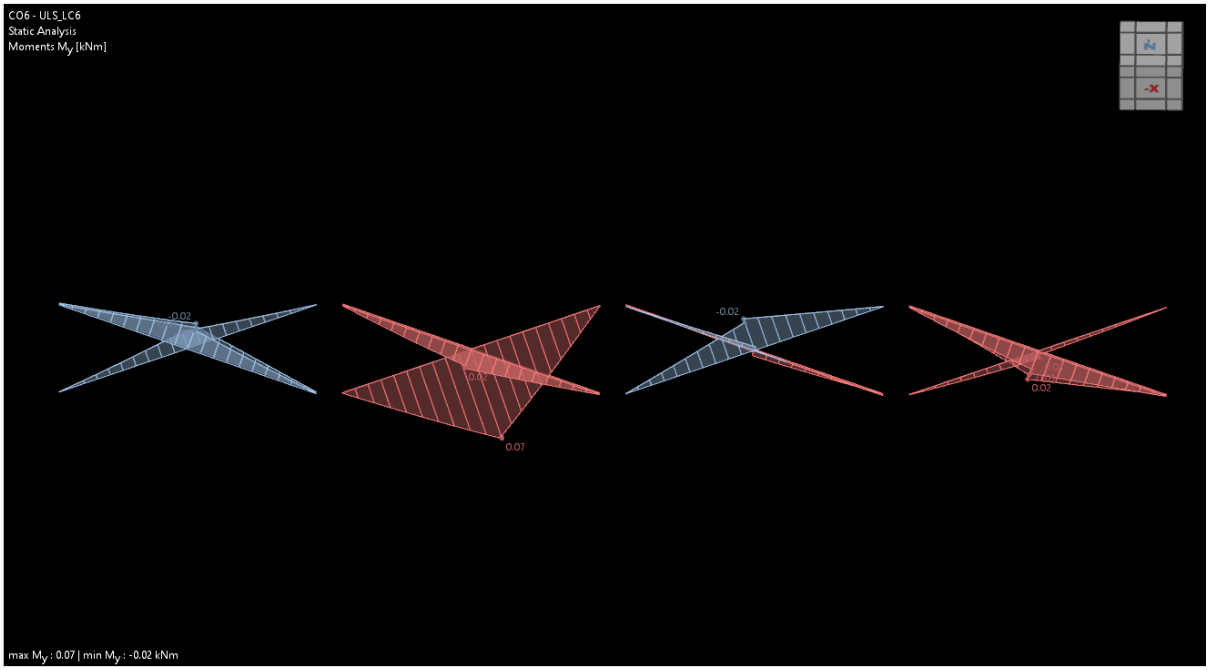

Figure 60. Bending moment diagram for the third translational member set of the structure (ULS_LC6).

Regarding the in-plane shear forces of the translational scissor-like elements (Fig.56), the distribution follows a pattern similar to that of the bending moments. The maximum shear force, equal to 0.10 kN, was developed in the second scissor-like element, with higher values concentrated on the windward side of the shelter.

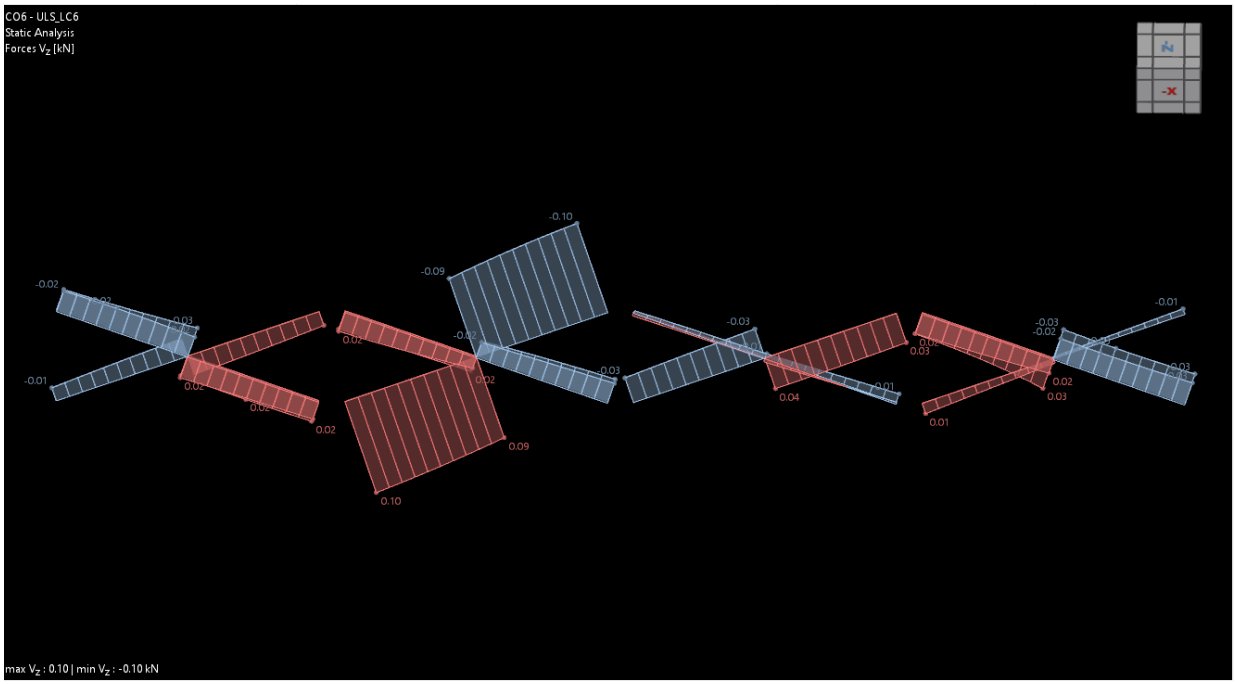

Figure 61. Shear force diagram for the third translational member set of the structure (ULS_LC6).

As illustrated in Fig.57, the highest von Mises stress occurs in a polar single-member scissor-like element of the third arch, located on the windward side of the shelter. The maximum stress in this member reaches 152.91 MPa, corresponding to 96% of the characteristic yield strength of the material (f_0 = 160 MPa).

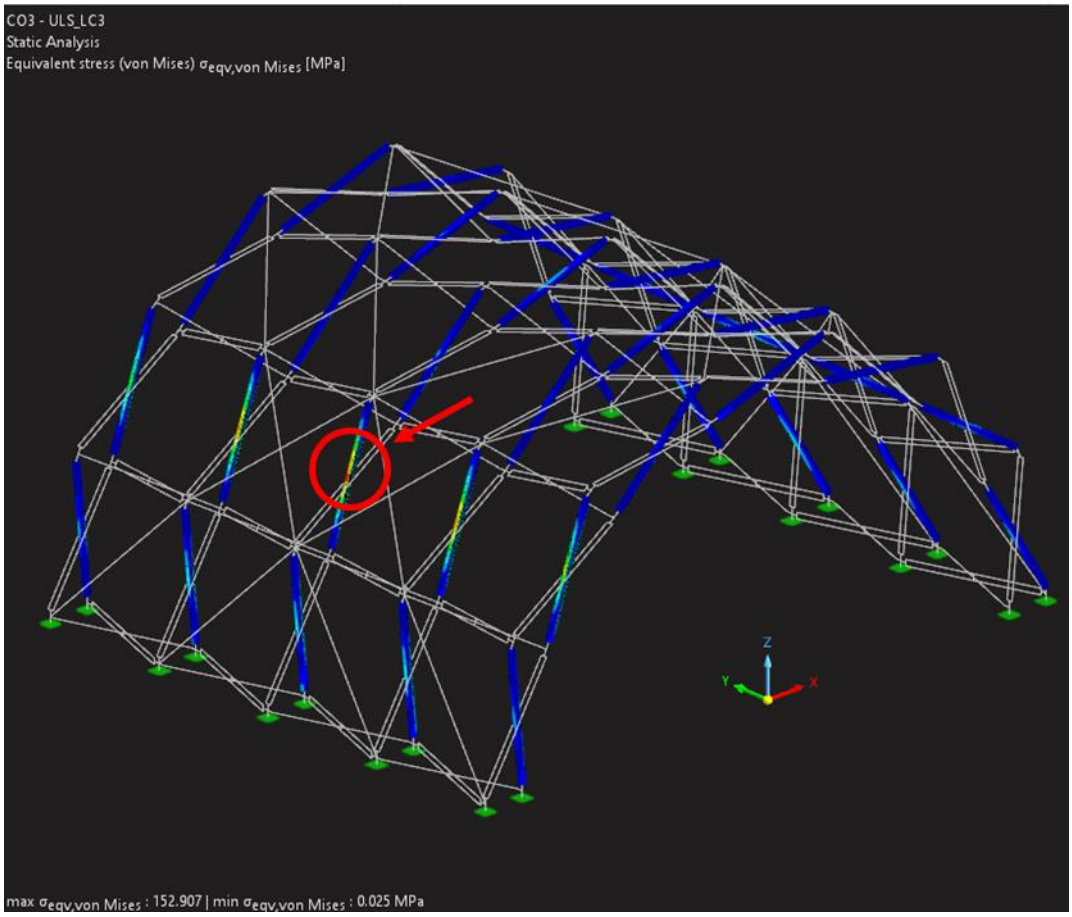

Figure 62. Von Mises stress distribution in single-member polar elements (ULS_LC3).

In the same area, the translational single-member scissor-like elements experience a maximum stress of 96.25 MPa, equivalent to 52% of the material yield strength.

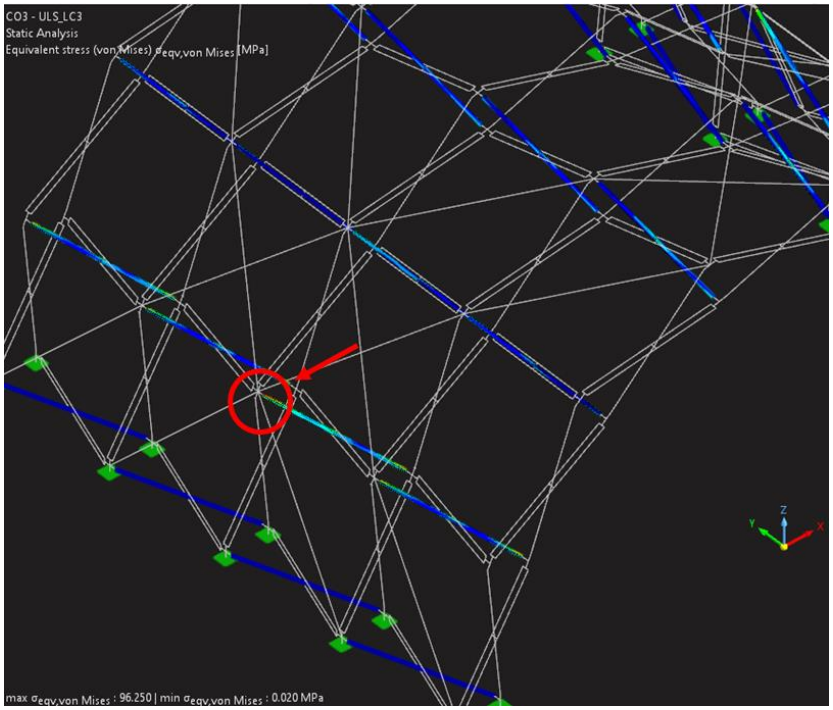

Figure 63. Von Mises stress distribution in single-member translational elements (ULS_LC3).

As illustrated in Fig.59, the maximum von Mises stress for the double-member configuration is observed in a polar double scissor-like element located in the second arch on the windward side of the shelter. The critical stress is calculated at 141.8 MPa, equivalent to 89% of the yield strength, indicating adequate structural performance.

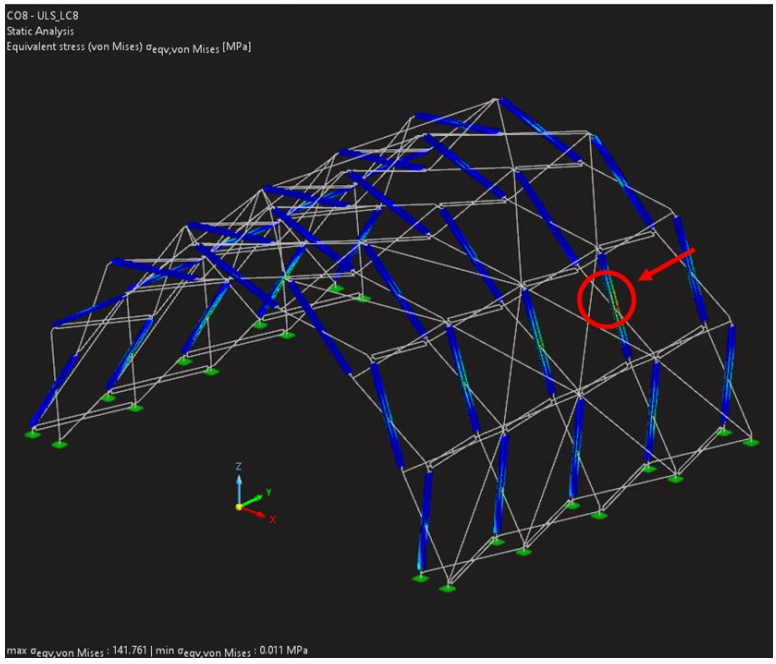

Figure 64. Von Mises stress distribution in double-member polar elements (ULS_LC8).

In the same region, the maximum stress in the translational double scissor-like elements, as shown in Fig.60, is also identified at 132.33 MPa, equivalent to 72% of the yield strength, lower than the corresponding stresses of the polar members. Regarding the bracing members, the stresses remain low,

corresponding to a small percentage of their tensile capacity, confirming that the bracing system operates well within the elastic range.

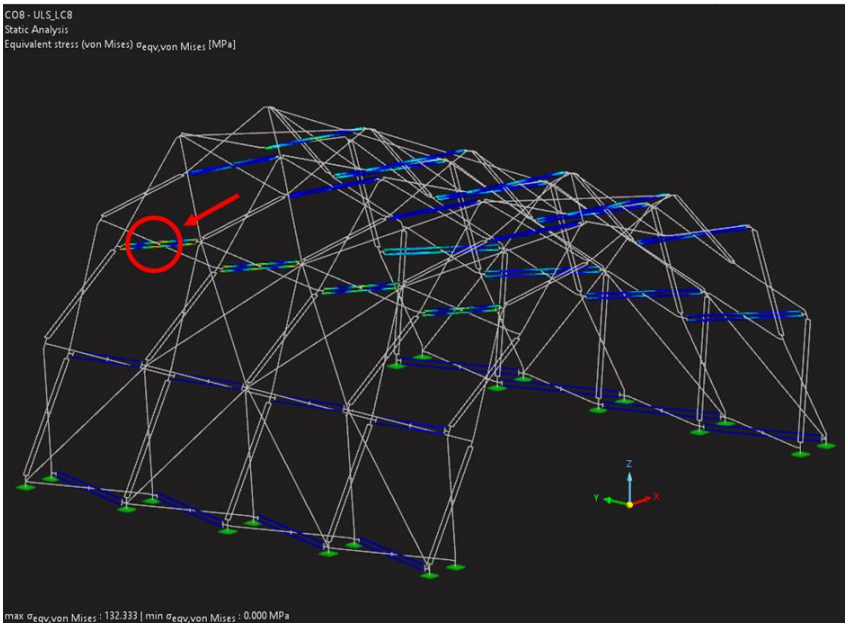

Figure 65. Von Mises stress distribution in double-member translational elements (ULS_LC8).

For the bracing members, which stabilise the structure laterally, the maximum stress corresponds to 249.11 equal to 50% of their tensile capacity.

5.2.1.3 Displacements of the structure

Fig.61 presents the deformed shape of the structure under ULS_LC6, which is consistent with the wind pressure acting on the windward side and suction developing on the leeward side.

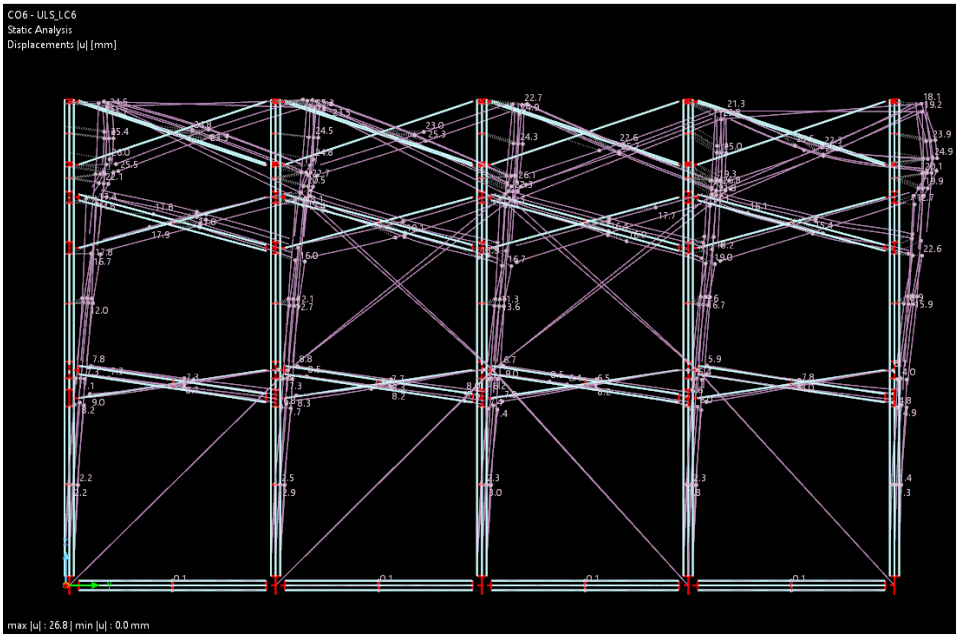

Figure 66. Structural deformation under longitudinal wind load as the leading live action (ULS_LC6).

Fig.62 presents the deformed shape of the structure under the transverse wind load combination, which is consistent with the wind pressure acting on the windward side and suction developing on the leeward side.

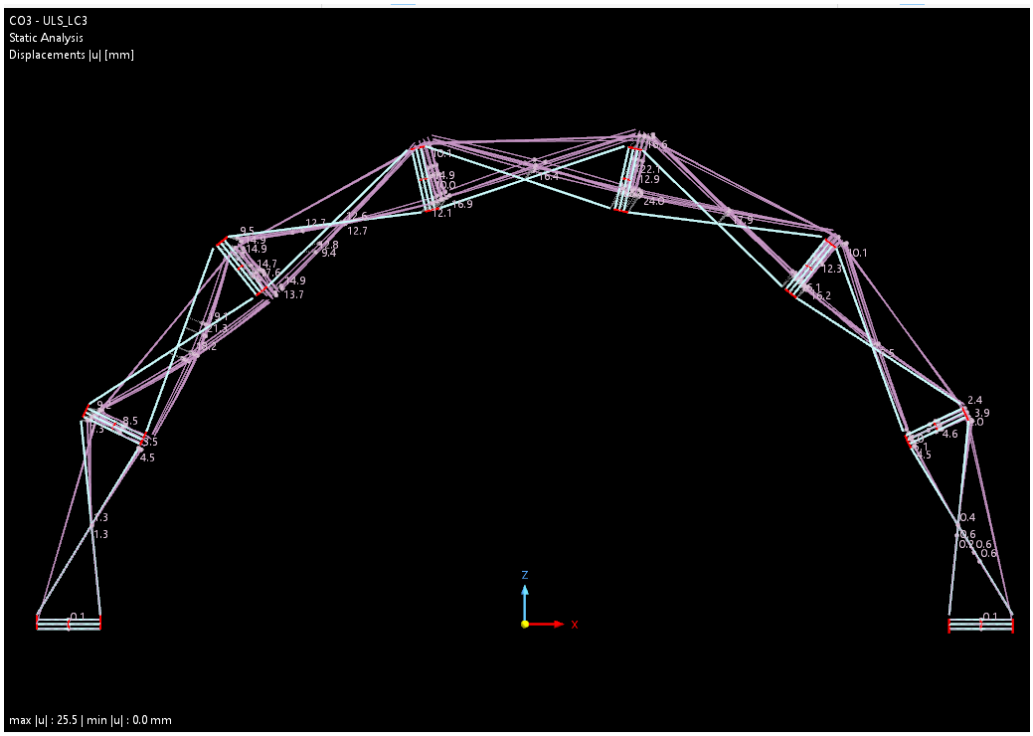

Figure 67. Deformed shape of the structure under transverse wind load as the leading live action (ULS_LC3).

Table 5-4 presents the maximum displacements of the shelter in the three principal directions for each load combination. Additionally, the ratio of displacement to the corresponding height or span of the structure is calculated in order to compare the results with the predefined limits for horizontal displacements and vertical deflection of the shelter, respectively.

Table 5-4. Maximum displacements of the shelter and corresponding displacement ratios for each load combination.

	Polar SLEs						**Translational SLEs**					
	Max. Disp. (mm)			**SLS Ratios for L = 5.72m, H = 3.45m**			**Max. Disp. (mm)**			**SLS Ratios for L = 5.72m, H = 3.45m**		
Load Combination	**x**	**y**	**z**	**ux/H**	**uy/H**	**w/L**	**x**	**y**	**z**	**ux/H**	**uy/H**	**w/L**
SLS_LC1	7.5	6	-18.4	**1/460**	**1/575**	**1/311**	5.6	6	-17.8	**1/616**	**1/575**	**1/321**
SLS_LC2	13.8	6.9	-21.3	**1/250**	**1/500**	**1/268**	12.4	6.8	-21.2	**1/278**	**1/507**	**1/270**
SLS_LC3	13.9	-4.1	15.6	**1/250**	**1/841**	**1/367**	11.4	-4.1	15.3	**1/303**	**1/841**	**1/374**
SLS_LC4	-4	15.7	4.8	**1/862**	**1/220**	**1/1192**	-3.6	15.6	-4.6	**1/958**	**1/221**	**1/1243**
SLS_LC5	14.9	-4.3	13.2	**1/231**	**1/802**	**1/433**	14.8	-4.2	12.3	**1/233**	**1/821**	**1/465**
SLS_LC6	8.5	17	-10.3	**1/406**	**1/203**	**1/555**	8	16.7	-10.3	**1/431**	**1/206**	**1/555**
SLS_LC7	16.3	4.6	-13.7	**1/212**	**1/750**	**1/417**	15.9	4.5	-13.2	**1/217**	**1/767**	**1/433**
SLS_LC8	14.9	15.8	-18.5	**1/232**	**1/218**	**1/309**	14.3	15.8	-18.5	**1/241**	**1/218**	**1/309**
SLS_LC9	9.1	-2.4	-7.3	**1/379**	**1/1437**	**1/784**	8.1	-2.4	-7.3	**1/426**	**1/1437**	**1/784**
SLS_LC10	8	14.9	-16.7	**1/431**	**1/231**	**1/342**	6.2	14.6	-16.2	**1/556**	**1/236**	**1/353**
SLS_LC11	6.4	-2.2	5.3	**1/539**	**1/1568**	**1/1079**	6.3	-2.1	4.8	**1/548**	**1/1643**	**1/1192**
SLS_LC12	4.5	11.6	-9.2	**1/767**	**1/298**	**1/622**	3.5	11.2	-8.9	**1/986**	**1/308**	**1/387**

5.2.2 Geometrically non-linear analysis

Since the cross sections are characterised as fully capable of bearing the loads applied to the structure, it was judged right to continue the study of the structure further by conducting geometrically non-linear analysis in order to highlight any different behaviour regarding the stresses developed in the members under the load combinations. Large displacements were assumed for the members, and the Newton-Raphson algorithm was used along with a maximum number of iterations of 100; the load was applied in a number of 50 load increments. Table 5-4 presents the maximum von Mises stresses identified for each of the five member types of the structure under all load combinations.

Table 5-4. Maximum Von Mises stresses for each member type.

	Polar SLEs		**Translational SLEs**		**Bracings (cables)**	
Load Combination	Max. Von Mises (MPa)	Ratio	Max. Von Mises (MPa)	Ratio	Max. Von Mises (MPa)	Ratio
ULS_LC1	121.20	**0.76**	60.50	**0.38**	22.11	**0.04**
ULS_LC2	124.22	**0.78**	89.05	**0.56**	74.65	**0.15**
ULS_LC3	150.54	**0.94**	97.17	**0.61**	106.49	**0.21**
ULS_LC4	59.48	**0.37**	72.58	**0.45**	228.73	**0.46**
ULS_LC5	112.84	**0.71**	91.31	**0.57**	94.86	**0.19**
ULS_LC6	96.44	**0.60**	95.55	**0.60**	249.08	**0.50**
ULS_LC7	91.77	**0.57**	67.27	**0.42**	73.60	**0.15**
ULS_LC8	144.12	**0.90**	121.64	**0.76**	180.71	**0.36**
ULS_LC9	84.18	**0.53**	51.65	**0.32**	29.97	**0.06**
ULS_LC10	134.69	**0.84**	94.21	**0.59**	161.91	**0.32**
ULS_LC11	102.60	**0.64**	78.30	**0.49**	84.13	**0.17**
ULS_LC12	90.43	**0.57**	90.60	**0.57**	240.18	**0.48**

The slight reduction in stresses observed in the geometrically nonlinear analysis can be attributed to the redistribution of internal forces resulting from large displacement effects. When geometric nonlinearity is considered, the structure is allowed to deform and adjust its load path, leading to a more realistic representation of the structural behavior [22]. In scissor-type deployable structures, this often results in increased membrane action and improved force redistribution among members, which may reduce peak stresses in certain elements. Consequently, the nonlinear analysis may predict slightly lower stresses compared to linear analysis, while providing a more accurate representation of the structural response.

5.2.3 Geometrically non-linear analysis with imperfections

Geometrical nonlinear analyses with imperfections (GNIA) were carried out for the most essential load combinations in order to examine the impact of initial flaws on the structural behaviour. The buckling mode shapes from the previous linear buckling analyses were used to define the first defect shapes as depicted in Figs. The literature states that all modes whose critical buckling load is less than twice that of the initial buckling mode should be included in order to calculate the number of buckling modes to be taken into consideration [15].

5.2.3.1 Linear buckling analysis results

In order to identify the first twelve buckling modes for every load combination, linear buckling studies were used to produce the initial defect shapes. The load multiplier for each mode, which is the factor by which the applied loads must be multiplied to meet the corresponding critical buckling load, is a crucial result of these assessments. In this instance, it was found that the structure would only approach the critical buckling load if the applied loads were increased by roughly 35 and 20 times, respectively, for load combinations ULS_LC3 and ULS_LC6. Below are depicted in Tabs 5-5 and 5-6 the load multipliers for the transversal and longitudinal wind load combinations of ULS_LC3 and ULS_LC6, respectively.

Table 5-5. Load multipliers for each of the twelve modes calculated (ULS_LC3).

Buckling Mode	**Load Factor LF_i**	**LFi/LF_1**
1	27.42	1
2	28.77	1
3	29.69	1.1
4	32.39	1.2
5	33.85	1.2
6	33.94	1.2
7	36.79	1.3
8	37.54	1.4
9	38.79	1.4
10	39.24	1.4
11	39.71	1.4
12	39.77	1.5

Table 5-6. Load multipliers for each of the twelve modes calculated (ULS_LC6).

Buckling Mode	Load Factor LF_i	LFi/LF_1
1	12.58	1
2	15.39	1.2
3	18.45	1.5
4	19.4	1.5
5	20.26	1.6
6	20.9	1.7
7	21.04	1.7
8	21.61	1.7
9	22.54	1.8
10	22.56	1.8
11	22.74	1.8
12	22.93	1.8

5.2.3.2 Selection of buckling modes for the initial imperfection scheme

The buckling modes of the two corresponding load combinations were investigated to determine which of the modes would be used as the initial imperfections scheme for the geometrically nonlinear analysis with imperfections. Multiple combinations were conducted so that the imperfections would not cancel each other out due to their orientation. The modes were combined equally and applied as an initial imperfection scheme to the structure. The chosen modes for each load combination are depicted below in Fig.63-64.

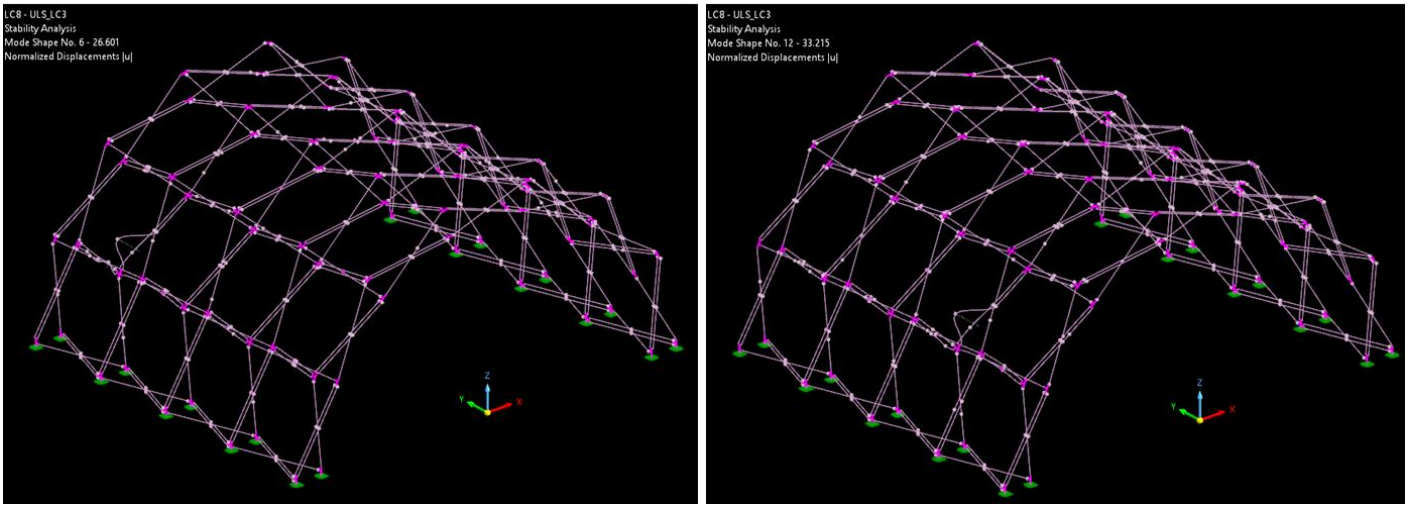

(a) **(b)**

Figure 68. Buckling mode shapes selected for the initial imperfection scheme of ULS_LC3: (a) 6th mode shape; (b) 12th mode shape.

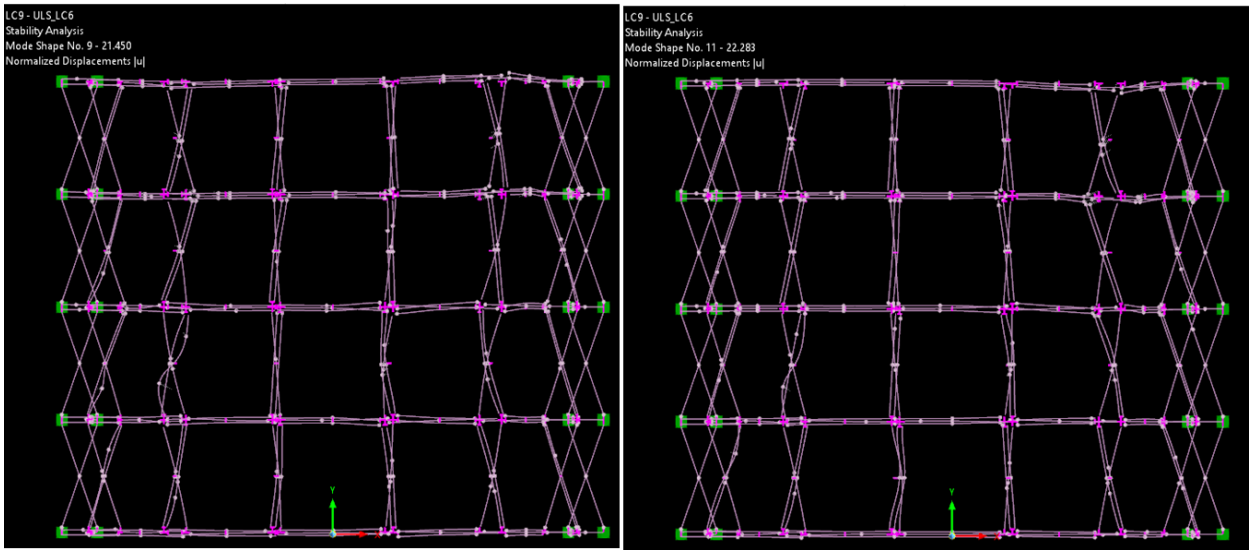

(a) **(b)**

Figure 69. Buckling mode shapes selected for the initial imperfection scheme of ULS_LC6: (a) 9th mode shape; (b) 11th mode shape.

The magnitude of the imperfections was chosen according to similar studies [15] and the corresponding regulations (EN755 [22]) at L/650, with L defined as the member length equal to 150cm. As an extreme case, the magnitude of L/100 was also implemented into the scheme. As a result, the final magnitude values are calculated as 2.31mm and 15mm, respectively.

5.2.3.3 Comparison of analysis results

The comparison between analyses with and without initial imperfections was carried out based on the maximum von Mises stresses of the polar and translational scissor-like elements, as well as the bracing members. The results, summarised in Tables 5-7 and 5-8, indicate that initial imperfections of magnitude L/650 have a negligible influence on the structural behaviour in terms of maximum stresses.

Table 5-7. Comparison of analysis results for ULS_LC3.

	Polar SLEs		**Translational SLEs**		**Bracings (cables)**	
Analysis type	Max. Von Mises (MPa)	Ratio	Max. Von Mises (MPa)	Ratio	Max. Von Mises (MPa)	Ratio
Linear	152.91	0.96	96.25	0.6	103.85	0.21
GNA	150.542	0.94	96.168	0.6	102.487	0.2
GNIA - L/650	153.094	0.96	98.928	0.62	102.792	0.21
GNIA - L/100	153.209	0.96	99.247	0.62	102.643	0.21

Table 5-8. Comparison of analysis results for ULS_LC6.

	Polar SLEs		**Translational SLEs**		**Bracings (cables)**	
Analysis type	Max. Von Mises (MPa)	Ratio	Max. Von Mises (MPa)	Ratio	Max. Von Mises (MPa)	Ratio
Linear	94.87	0.59	93.072	0.58	249.11	0.5
GNA	94.433	0.59	92.547	0.58	249.083	0.5
GNIA - L/650	96.26	0.6	95.586	0.6	249.083	0.5
GNIA - L/100	96.44	0.6	95.666	0.6	249.063	0.5

In conclusion, it was discovered that initial flaws had very little effect on the behaviour of the structure. Despite the fact that the linear analysis showed a near failure state for the polar SLEs, the implementation of imperfections to the nonlinear model showed minor changes. This may happen due to the redistribution of stresses mentioned before, due to the structure trying to follow the load path. Finally, initial flaws have a limited overall impact on the structural response since they primarily affect geometric nonlinearity.

6 DESIGN OF STRUCTURAL MEMBERS

By conducting multiple analysis methods, no reason for altering the cross sections was found. The regulatory process, though, defines a process different from the simple stress check conducted before, so before proceeding with the final adoption of the current cross sections, they need to be checked and designed according to the proper regulations of EN 1999 [23].

6.1 Design according to Eurocode 9

The section design is conducted according to EN 1999 [23] using the embedded designer of RFEM 6 [20]. The process involves both section proof and stability checks for the members. The corresponding checks are listed below in Tab 5-9.

Tab 5-9. Designs checks according to EN 1999

Description
Section Proof
Torsion acc. to 6.2.7.2(4)
Resulting shear and torsion acc. to 6.2.1(5)
Resulting shear acc. to 6.2.1(5)
Normal and shear stress acc. to 6.2.1(5)
Normal stress acc. to 6.2.1(5)
Stability
Flexural buckling about principal y-axis acc. to 6.3.1.1 and 6.3.1.2
Flexural buckling about principal z-axis acc. to 6.3.1.1 and 6.3.1.2

The following Eq. 5-7 shows the resulting shear and torsion check design ratio η according to paragraphs 6.2.1 and 6.2.7.2 of EN1999, which should be no greater than 1.

$$\eta = \frac{\sqrt{3} \cdot |\tau_{Ed}|}{\frac{f_o}{\gamma_{M1}}} \tag{5-7}$$

Where τ_{Ed} corresponds to the design shear stress, f_o is the characteristic value of 0.2% proof strength, and γ_{M1} corresponds to the partial factor equal to 1.1. The following Eq. 5-8;11 shows the normal and shear stress check design ratio η according to paragraph 6.2.1 of EN1999, which is also no greater than 1.

$$\eta_1 = \frac{\left(\frac{\sigma_{x,Ed}}{\frac{f_o}{\gamma_{M1}}}\right) + 3 \cdot \left(\frac{\tau_{Ed}}{\frac{f_o}{\gamma_{M1}}}\right)^2}{C} \tag{5-8}$$

$$\eta_2 = \frac{\sigma_{x,Ed}}{\frac{f_o}{\gamma_{M1}}} \tag{5-9}$$

$$\eta_3 = \frac{\sqrt{3} \cdot |\tau_{Ed}|}{\frac{f_o}{\gamma_{M1}}} \tag{5-10}$$

$$\eta = \max(n_1, n_2, n_3) \tag{5-11}$$

Where n_{1-3} correspond to the design ratios for combined normal and shear stresses, normal stresses, and shear stresses, respectively; $\sigma_{x,Ed}$ represents the design axial stress; and C is the yield criterion constant, taken equal to 1.2 in this case.

The stability flexural buckling about principal y-axis according to paragraphs 6.3.1.1 and 6.3.1.2 is defines as follows:

$$N_{cr,y} = \frac{(\pi)^2 \cdot E \cdot I_y}{\left(k_y\right)^2 \cdot \left(L_y\right)^2} \tag{5-12}$$

$$\bar{\lambda}_y = \sqrt{\frac{A_g \cdot f_o}{N_{cr,y}}} \tag{5-13}$$

Where $N_{cr,y}$ corresponds to the elastic critical axial force for flexural buckling; E is the modulus of elasticity; I_y is the moment of inertia about the y-axis; k_y is the buckling length factor, taken as 1.0; L_y is the reference length, equal to 637 cm; λy is the relative slenderness; A_g is the gross cross-sectional area; N_{Ed} is the design axial force; and λ0 is the horizontal plateau limit. Equations 5-12; 13 should satisfy the following Eq. 14.

$$N_{Ed} \leq \left(\bar{\lambda}_0\right)^2 \cdot N_{cr,y} \tag{5-14}$$

The stability flexural buckling about principal z-axis according to paragraphs 6.3.1.1 and 6.3.1.2 is defined as follows:

$$N_{cr,z} = \frac{(\pi)^2 \cdot E \cdot I_z}{(k_z)^2 \cdot (L_z)^2} \tag{5-15}$$

$$\bar{\lambda}_z = \sqrt{\frac{A_g \cdot f_o}{N_{cr,z}}} \tag{5-16}$$

$$N_{cr,z} = \frac{(\pi)^2 \cdot E \cdot I_z}{(k_z)^2 \cdot (L_z)^2} \tag{5-17}$$

$$\Phi = 0.5 \cdot \left(1 + \alpha \cdot \left(\bar{\lambda}_z - \bar{\lambda}_0\right) + \left(\bar{\lambda}_z\right)^2\right) \tag{5-18}$$

$$\chi_z = \frac{1}{\Phi + \sqrt{(\Phi)^2 - \left(\bar{\lambda}_z\right)^2}} \tag{5-19}$$

$$\omega_x = \frac{1}{\chi_z + (1 - \chi_z) \cdot \sin\left(\frac{\pi \cdot \chi_s}{L_{cr,z}}\right)} \tag{5-20}$$

$$N_{z,b,R_d} = \kappa \cdot \chi_z \cdot \omega_x \cdot A_g \cdot \frac{f_o}{\gamma_{M1}} \tag{5-21}$$

$$\eta = \frac{N_{Ed}}{N_{z,b,R_d}} \tag{5-22}$$

Where $N_{cr,z}$ is the elastic critical axial force for flexural buckling; I_z is the moment of inertia about the z-axis; k_z is the buckling length factor assumed 1.0; L_z is the reference length equal to 637cm; λ_z is the relative slenderness; A_g is the gross cross-sectional area; Φ is the parameter used to determine the buckling reduction factor χ; α is the imperfection factor assumed 0.2; $\lambda 0$ is the horizontal plateau limit; χ_z is the buckling reduction factor; ω_x is the factor related to the location of the design section; x_s is the distance to the simple support or point of contra flexure of the deflection curve calculated as 0.319m; $L_{cr,z}$ is the buckling length; $N_{z,b,Rd}$ is the design buckling resistance; κ is the factor accounting for the weakening effect of longitudinal welds equal to 1.0; γ_{M1} is the partial safety factor; N_{Ed} is the design axial force; and $N_{z,b}$ is the design buckling resistance. The corresponding design ratios for the assumed polar and translational cross-sections are presented in Tables 5-10 and 5-11.

Table 5-10. Corresponding design ratio for the assumed polar cross sections.

RHS 70x40x3		
Load Combination	**Design Check Ratio**	**Description**
		Section Proof
ULS_LC7	0.08	| Torsion acc. to 6.2.7.2(4)
ULS_LC7	0.09	| Resulting shear and torsion acc. to 6.2.1(5)
ULS_LC4	0.08	| Resulting shear acc. to 6.2.1(5)
ULS_LC4	1.05	| Normal and shear stress acc. to 6.2.1(5)
ULS_LC10	0.06	| Normal stress acc. to 6.2.1(5)
		Stability
ULS_LC2	0.17	| Flexural buckling about principal y-axis acc. to 6.3.1.1 and 6.3.1.2
ULS_LC7	0.18	| Flexural buckling about principal z-axis acc. to 6.3.1.1 and 6.3.1.2
RHS 60x20x3		
Load Combination	**Design Check Ratio**	**Description**
		Section Proof
ULS_LC7	0.05	| Torsion acc. to 6.2.7.2(4)
ULS_LC7	0.08	| Resulting shear and torsion acc. to 6.2.1(5)
ULS_LC2	0.04	| Resulting shear acc. to 6.2.1(5)
ULS_LC7	0.99	| Normal and shear stress acc. to 6.2.1(5)
ULS_LC11	0.06	| Normal stress acc. to 6.2.1(5)
		Stability
ULS_LC11	0.16	| Flexural buckling about principal y-axis acc. to 6.3.1.1 and 6.3.1.2
ULS_LC11	0.37	| Flexural buckling about principal z-axis acc. to 6.3.1.1 and 6.3.1.2

Table 5-11. Corresponding design ratio for the assumed translational cross sections.

RHS 35x30x3		
Load Combination	**Design Check Ratio**	**Description**
		Section Proof
ULS_LC4	0.23	| Torsion acc. to 6.2.7.2(4)
ULS_LC4	0.27	| Resulting shear and torsion acc. to 6.2.1(5)
ULS_LC7	0.04	| Resulting shear acc. to 6.2.1(5)
ULS_LC4	0.61	| Normal and shear stress acc. to 6.2.1(5)
ULS_LC4	0.03	| Normal stress acc. to 6.2.1(5)
		Stability
ULS_LC3	0.06	| Flexural buckling about principal y-axis acc. to 6.3.1.1 and 6.3.1.2
ULS_LC3	0.06	| Flexural buckling about principal z-axis acc. to 6.3.1.1 and 6.3.1.2
RHS 30x15x3		
Load Combination	**Design Check Ratio**	**Description**
		Section Proof
ULS_LC7	0.25	| Torsion acc. to 6.2.7.2(4)
ULS_LC7	0.27	| Resulting shear and torsion acc. to 6.2.1(5)
ULS_LC11	0.03	| Resulting shear acc. to 6.2.1(5)
ULS_LC7	0.91	| Normal and shear stress acc. to 6.2.1(5)
ULS_LC4	0.06	| Normal stress acc. to 6.2.1(5)
		Stability
ULS_LC7	0.11	| Flexural buckling about principal y-axis acc. to 6.3.1.1 and 6.3.1.2
ULS_LC7	0.28	| Flexural buckling about principal z-axis acc. to 6.3.1.1 and 6.3.1.2

For the polar members, the design ratios are generally satisfactory, with the exception of the single-member polar cross-section, which exhibits a slight exceedance under combined normal and shear stresses for load combination ULS_LC4. This load case corresponds to the application of longitudinal

wind load, indicating that the selected cross-section is marginally insufficient under these conditions. In contrast, the double-member polar cross-section satisfies the design requirements, with load combination ULS_LC7 governing and producing a design ratio of 0.99, which is considered acceptable despite being close to the limit. The same load combination is also critical for the double-member translational cross-section, where the combined normal and shear stress check yields a design ratio of 0.91. The apparent failure of the single-member polar cross-section demands the update of this cross-section. As a result, the updated cross-section is presented below in Fig.65.

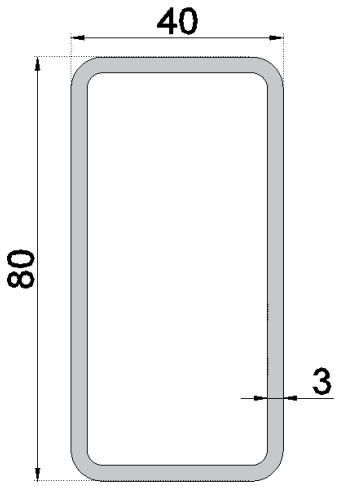

Figure 70. Updated single-member polar cross section.

As a result the updated design ratios for the assumed polar and translational cross-sections are presented in Tables 5-12 and 5-13.

Table 5-12. Corresponding design ratio for the assumed polar cross sections considering the updated single-member polar cross section.

RHS 80x40x3		
Load Combination	**Design Check Ratio**	**Description**
		Section Proof
ULS_LC8	0.07	| Torsion acc. to 6.2.7.2(4)
ULS_LC8	0.08	| Resulting shear and torsion acc. to 6.2.1(5)
ULS_LC3	0.08	| Resulting shear acc. to 6.2.1(5)
ULS_LC3	0.94	| Normal and shear stress acc. to 6.2.1(5)
ULS_LC9	0.06	| Normal stress acc. to 6.2.1(5)
		Stability
ULS_LC2	0.15	| Flexural buckling about principal y-axis acc. to 6.3.1.1 and 6.3.1.2
ULS_LC2	0.16	| Flexural buckling about principal z-axis acc. to 6.3.1.1 and 6.3.1.2
RHS 60x20x3		
Load Combination	**Design Check Ratio**	**Description**
		Section Proof
ULS_LC2	0.06	| Torsion acc. to 6.2.7.2(4)
ULS_LC8	0.08	| Resulting shear and torsion acc. to 6.2.1(5)
ULS_LC2	0.04	| Resulting shear acc. to 6.2.1(5)
ULS_LC8	0.96	| Normal and shear stress acc. to 6.2.1(5)
ULS_LC10	0.10	| Normal stress acc. to 6.2.1(5)
		Stability
ULS_LC12	0.17	| Flexural buckling about principal y-axis acc. to 6.3.1.1 and 6.3.1.2
ULS_LC12	0.37	| Flexural buckling about principal z-axis acc. to 6.3.1.1 and 6.3.1.2

Table 5-13. Corresponding design ratio for the assumed translational cross sections considering the updated single-member polar cross section.

RHS 60x20x3		
Load Combination	**Design Check Ratio**	**Description**
		Section Proof
ULS_LC2	0.06	| Torsion acc. to 6.2.7.2(4)
ULS_LC8	0.08	| Resulting shear and torsion acc. to 6.2.1(5)
ULS_LC2	0.04	| Resulting shear acc. to 6.2.1(5)
ULS_LC8	0.96	| Normal and shear stress acc. to 6.2.1(5)
ULS_LC10	0.10	| Normal stress acc. to 6.2.1(5)
		Stability
ULS_LC12	0.17	| Flexural buckling about principal y-axis acc. to 6.3.1.1 and 6.3.1.2
ULS_LC12	0.37	| Flexural buckling about principal z-axis acc. to 6.3.1.1 and 6.3.1.2
RHS 30x15x3		
Load Combination	**Design Check Ratio**	**Description**
		Section Proof
ULS_LC8	0.24	| Torsion acc. to 6.2.7.2(4)
ULS_LC8	0.26	| Resulting shear and torsion acc. to 6.2.1(5)
ULS_LC12	0.02	| Resulting shear acc. to 6.2.1(5)
ULS_LC8	0.89	| Normal and shear stress acc. to 6.2.1(5)
ULS_LC3	0.05	| Normal stress acc. to 6.2.1(5)
		Stability
ULS_LC8	0.11	| Flexural buckling about principal y-axis acc. to 6.3.1.1 and 6.3.1.2
ULS_LC8	0.29	| Flexural buckling about principal z-axis acc. to 6.3.1.1 and 6.3.1.2

While the single-member polar cross-section is updated, the corresponding design ratios are not changed significantly. The failure ceased to exist, and the rest of the cross-section design ratios were reduced slightly, but not significantly. The updated structural response of the structure with the new single-member polar cross section is depicted below in Tab. 5-14.

Table 5-14. Updated structural response of the structure with the new single-member polar cross section.

	Polar SLEs				**Translational SLEs**				**Bracings (cables)**	
	Single		**Double**		**Single**		**Double**			
Load Combination	Max. Von Mises (MPa)	Ratio	Max. Von Mises (MPa)	Ratio	Max. Von Mises (MPa)	Ratio	Max. Von Mises (MPa)	Ratio	Max. Von Mises (MPa)	Ratio
ULS_LC1	105.27	**0.66**	113.16	**0.71**	57.95	**0.31**	68.59	**0.37**	18.06	**0.04**
ULS_LC2	95.66	**0.6**	121.99	**0.76**	85.75	**0.46**	98.75	**0.53**	67.99	**0.14**
ULS_LC3	137.19	**0.86**	97.43	**0.61**	92.1	**0.5**	88.99	**0.48**	96.89	**0.19**
ULS_LC4	44.38	**0.28**	58.55	**0.37**	39.48	**0.21**	69.89	**0.38**	227.87	**0.46**
ULS_LC5	101.82	**0.64**	66.32	**0.41**	90.88	**0.49**	93.06	**0.5**	89.7	**0.18**
ULS_LC6	64.52	**0.4**	93.74	**0.59**	54.57	**0.29**	96.39	**0.52**	246.52	**0.49**
ULS_LC7	72.45	**0.45**	90.87	**0.57**	66.27	**0.36**	72.75	**0.39**	69.86	**0.14**
ULS_LC8	90.23	**0.56**	139.85	**0.87**	83.4	**0.45**	131.4	**0.71**	175.57	**0.35**
ULS_LC9	56.72	**0.35**	82.89	**0.52**	41.59	**0.22**	51.84	**0.28**	30.75	**0.06**
ULS_LC10	112.91	**0.71**	130.86	**0.82**	63	**0.34**	99.34	**0.54**	155.16	**0.31**
ULS_LC11	93.42	**0.58**	58.78	**0.37**	78.15	**0.42**	78.51	**0.42**	79.07	**0.16**
ULS_LC12	74.36	**0.46**	88.06	**0.55**	51.78	**0.28**	87.85	**0.47**	236.75	**0.47**

6.2 Design of joints

6.2.1 Maximum and minimum bolt spacing

Selection of edge distances e1 and e_2 for the polar elements:

From EN1999-1-1 Tab 8.2 assuming: Normal hole with d_0 = 13 mm and thickness t based on each of the four cross sections selected from the design.

For polar element RHS 80X40X3:

$$1.2 \cdot d_0 \leq e_1 \leq 4 \cdot t + 40$$

$$15.6 \leq e_1 \leq 52 \quad (5\text{-}23)$$

e_1=40mm is adopted

$$1.2 \cdot d_0 \leq e_2 \leq 4 \cdot t + 40$$

$$15.6 \leq e_2 \leq 52 \quad (5\text{-}24)$$

e_2=40mm is adopted

For polar element RHS 60X20X3

$$1.2 \cdot d_0 \leq e_1 \leq 4 \cdot t + 40$$

$$15.6 \leq e_1 \leq 52 \quad (5\text{-}25)$$

e_1=30mm is adopted

$$1.2 \cdot d_0 \leq e_2 \leq 4 \cdot t + 40$$

$$15.6 \leq e_2 \leq 52 \quad (5\text{-}26)$$

e_2=30mm is adopted

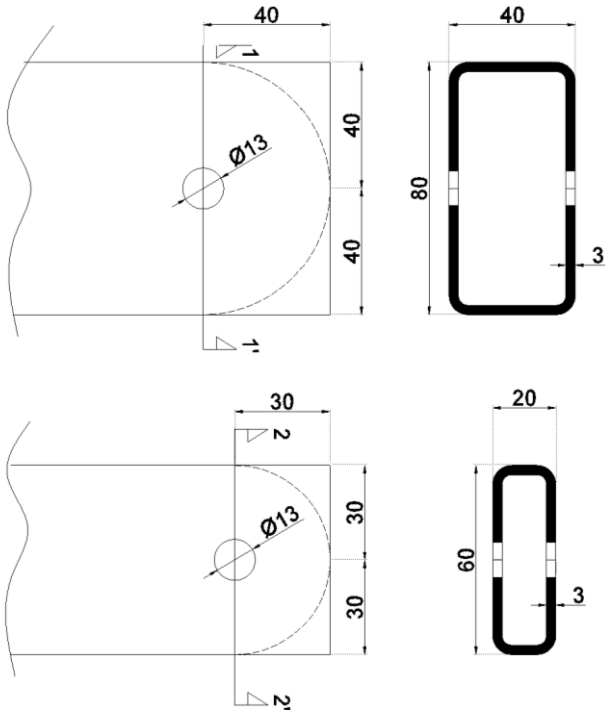

Figure 71. Edge distances e_1 and e_2 for the polar elements.

Selection of edge distances e1 and e_2 for the translational elements:

From EN1999-1-1 Tab 8.2 assuming: Normal hole with d_0 = 11 mm and thickness t based on each of the four cross sections selected from the design.

For polar element RHS 35X30X3

$$1.2 \cdot d_0 \leq e_1 \leq 4 \cdot t + 40$$

$$13.2 \leq e_1 \leq 52 \quad (5\text{-}27)$$

e_1=17.5mm is adopted

$$1.2 \cdot d_0 \leq e_2 \leq 4 \cdot t + 40$$

$$13.2 \leq e_2 \leq 52 \quad (5\text{-}28)$$

e_2=17.5mm is adopted

For polar element RHS 30X15X3

$$1.2 \cdot d_0 \leq e_1 \leq 4 \cdot t + 40$$

$$13.2 \leq e_1 \leq 52 \quad (5\text{-}29)$$

e_1=15mm is adopted

$$1.2 \cdot d_0 \leq e_2 \leq 4 \cdot t + 40$$

$$13.2 \leq e_2 \leq 52 \quad (5\text{-}30)$$

e_2=15mm is adopted

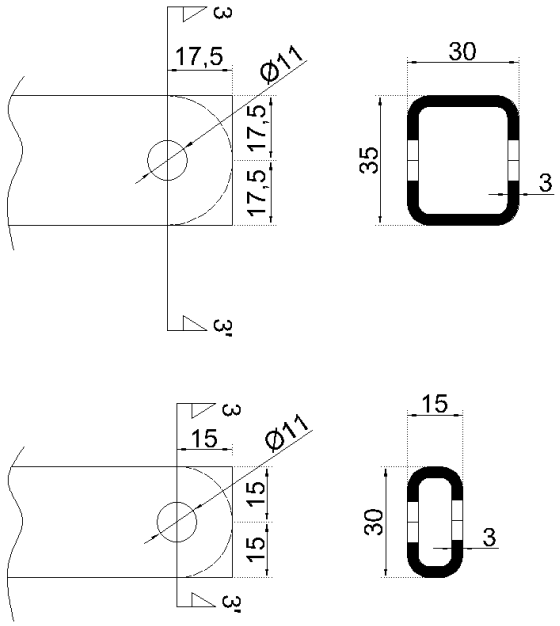

Figure 72. Edge distances e_1 and e_2 for the translational elements.

The material properties of the members considered in the design are summarized as follows:

- Steel yield strength: f_y = 235 MPa
- Steel ultimate strength: f_u = 360 MPa
- Aluminium yield strength: f_o = 160 MPa
- Aluminium ultimate strength: f_u = 195 MPa
- Polar bolt yield strength: f_{yb} = 300 MPa
- Bolt ultimate strength: f_{ub} = 500 MPa

The geometric characteristics of the examined members are summarized as follows:

- Thickness of steel plates: t = 8 mm
- Cross-sectional area of steel plates: A = 560 mm²
- Thickness of aluminium sections: t_{PO} = t_{TR} = 3 mm
- Cross-sectional area of aluminium sections: A_{PO_S} = 661 mm², A_{PO_D} = 421 mm², A_{TR_S} = 331 mm², A_{TR_D} = 211 mm²

- Bolt diameter: d_{PO} = 12 mm, d_{TR} = 10 mm
- Hole diameter: d_{0_PO} = 13 mm, d_{0_TR} = 11 mm
- Shear area of bolt shank: A = 113 mm²
- Shear area of threaded portion: As = 84.3 mm²

The partial safety factors adopted for building structures are:

- γM0 = 1.00
- γM1 = 1.00
- γM2 = 1.25

6.2.2 Bearing resistance

According to EN1999-1-1 the bearing resistance of the aluminum members is calculated as follows:

$$F_{b,Rd} = \frac{a_b \cdot f_u \cdot d \cdot t}{\gamma_{M2}}$$
$$a_b = min\left[\frac{e_1}{d_0}; 3 \cdot \frac{f_{ub}}{f_u}; 3\right] \quad (5\text{-}31)$$

According to EN1993 the bearing resistance of the steel joint is calculated as follows:

$$F_{b,Rd} = \frac{k_m \cdot a_b \cdot f_u \cdot d \cdot t}{\gamma_{M2}}$$
$$a_b = min\left[\frac{e_1}{d_0}; 3 \cdot \frac{f_{ub}}{f_u}; 3\right] \quad (5\text{-}32)$$

Where k_m=1 for steel grades up to S460.

6.2.3 Bolt shear resistance

According to EN1993-1-8 the bearing resistance of the polar and translational bolts is calculated as follows:

$$F_{v,Rd} = \frac{0.6 \cdot f_{ub} \cdot A}{\gamma_{M2}} \quad (5\text{-}33)$$

6.2.4 Tensile resistance of member cross-sections

According to EN1993 the tensile resistance of the steel joint is calculated as follows:

$$N_{t,Rd} = min\left[N_{pl,Rd}, N_{u,Rd}\right] \quad (5\text{-}34)$$

Where,

$$N_{pl,Rd} = \frac{A \cdot f_y}{\gamma_{M0}}, \qquad N_{pl,Rd} = \frac{k \cdot A_{net} \cdot f_y}{\gamma_{M2}}$$

$$A_{net} = A - d_0 \cdot t \quad and\ k=0.9$$

According to EN1999-1-1 the tensile resistance of the aluminum members is calculated as follows:

$$N_{t,Rd} = min\left[N_{o,Rd}, N_{net,Rd}\right] \quad (5\text{-}35)$$

Where,

$$N_{o,Rd} = \frac{A_{eff} \cdot f_0}{\gamma_{M1}}, \qquad N_{net,Rd} = \frac{0.9 \cdot A_{net} \cdot f_u}{\gamma_{M2}}$$

$$A_{net} = A - 2 \cdot d_0 \cdot t \quad and\ k=0.9$$

By substituting the material properties, geometric characteristics, and the partial safety factors adopted for the structures, the checks related to the joint plates and the shear resistance of the bolts were conducted, the results are depicted in Tab.5-15 with the governing action taken as the maximum axial force obtained from the initial model analysis for all ULS load combinations, equal to 13.50 kN. For the verification of the scissor-like elements, the design actions were defined as the maximum axial forces recorded in each member type, namely 13.58kN for the single-member polar elements, 8.98kN for the double-member polar elements, 2.01kN for the single-member translational elements, and 2.48kN for the double-member translational elements.

Table 5-15. Design connection checks and utilization ratios.

Check	**Resistance (kN)**	**Action (kN)**	**Utilisation ratio**
Bearing resistance of the steel joint plate (Single members)	85.16	13.58	0.16
Bearing resistance of the steel joint plate (Double members)	42.58	14.58	0.34
Bearing resistance of the polar SLE (Single-member)	16.85	13.58	0.81
Bearing resistance of the polar SLE (Double-member)	12.97	8.98	0.69
Bearing resistance of the translational SLE (Single-member)	7.49	2.01	0.27
Bearing resistance of the translational SLE (Double-member)	6.36	2.48	0.39
Shear resistance of the bolt (M12)	27.12	13.58	0.5
Shear resistance of the bolt (M10)	18.96	2.48	0.13
Tension resistance of members – steel joint plate	14.51	13.58	0.94
Tension resistance of the polar SLE (Single-member)	81.85	13.58	0.17
Tension resistance of the polar SLE (Double-member)	48.16	8.98	0.19
Tension resistance of the translational SLE (Single-member)	37.21	2.01	0.05
Tension resistance of the translational SLE (Double-member)	20.36	2.48	0.12

7 DEVELOPMENT OF A JOINT WITHOUT ECCENTRICITY

7.1 Conceptual design of the joint

The key objective of this study is the development of a joint without eccentricities to improve the structural behavior and efficiency of scissor-type deployable structures. The previous chapters described the process of generating the structures geometry developing the model and analyzing it with the ultimate purpose of obtaining the final member cross sections in order to start shaping the joint (Fig.68).

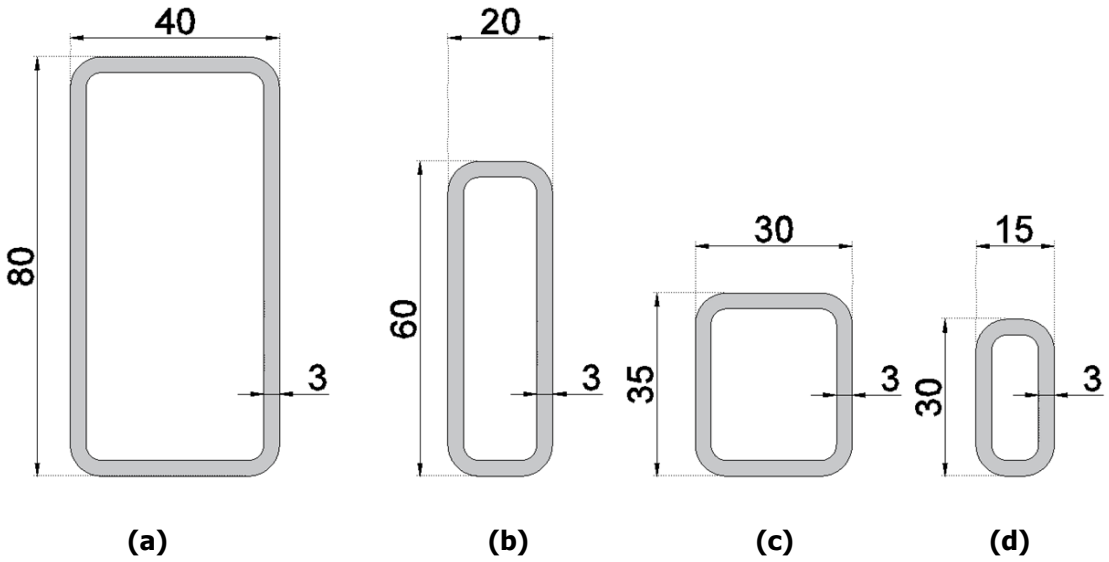

Figure 73. Final adopted cross-sections for the polar single-member (a), polar double-member (b), translational single-member (c), and translational double-member (d) elements.

To address this issue, a conceptual joint configuration was developed with the objective of minimising or eliminating eccentricities between the connected members. The design aims to ensure that the

centroidal axes of the scissor-like elements intersect at a common point, allowing forces to be transferred primarily through axial action. While the ideal geometrical conception involves perfect alignment between the forces, in reality, this can be achieved only by splitting one force per member group in two for the double-member SLEs. As a result, instead of each member group (polar, translational) asking the joint to apply two forces, they ask the joint to apply three forces, one of which corresponds to the axial force of the single member, denoted as N_S, and the other two correspond to N_D, as displayed in Fig.69.

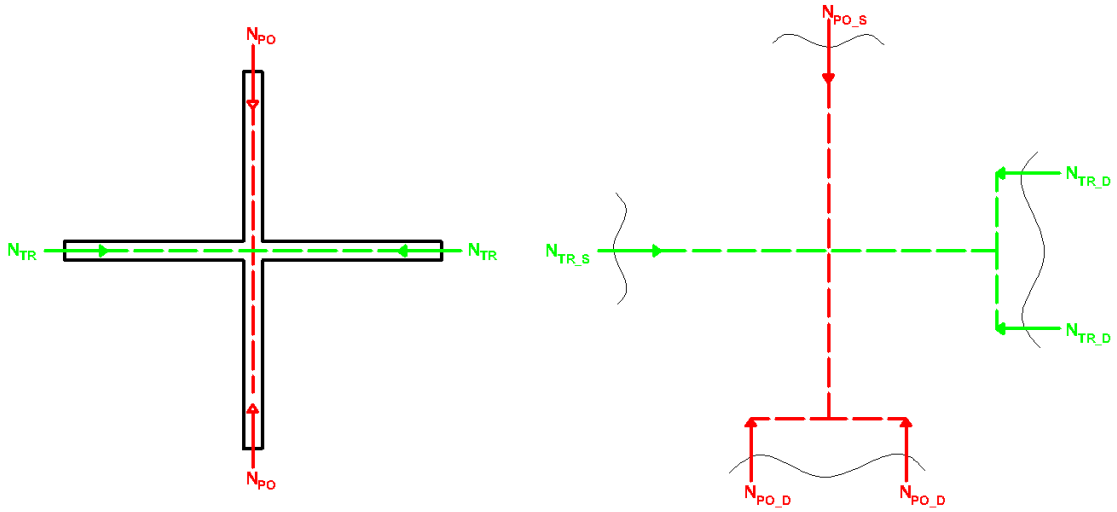

Figure 74. Force flow in the conceptual joint geometry generator (a) compared with the modeled configuration (b).

7.2 Design requirements

The proposed joint geometry aims to minimise the eccentricity between opposing pairs of connected members, which is reduced to the width of the cross-section of the members meeting at the joint.

In order to generate the geometry of the joint, the distances e1 and e2 according to EN1993-1-8 of the selected thread holes d_{0_PO}=13mm and d_{0_TR}=11mm of Chapter 5 should be calculated.

From EN1993-1-8 Tab. 3.3 assuming d_{0_PO}=13mm and d_{0_TR}=11mm:

$$1.2 \cdot d_0 \leq e_1 \leq 4 \cdot t + 40$$

$$13.2; 15.6 \leq e_1 \leq 72 \quad (6\text{-}1)$$

e_1=20mm is adopted

$$1.2 \cdot d_0 \leq e_2 \leq 4 \cdot t + 40$$

$$13.2; 15.6 \leq e_2 \leq 72 \quad (6\text{-}2)$$

e_2=16mm is adopted

As a result, the geometry of the joint is generated by simply placing all the members in the initial joint configuration according to their corresponding distances e1. Then the geometry is optimised according to these distances, as shown in Fig.70.

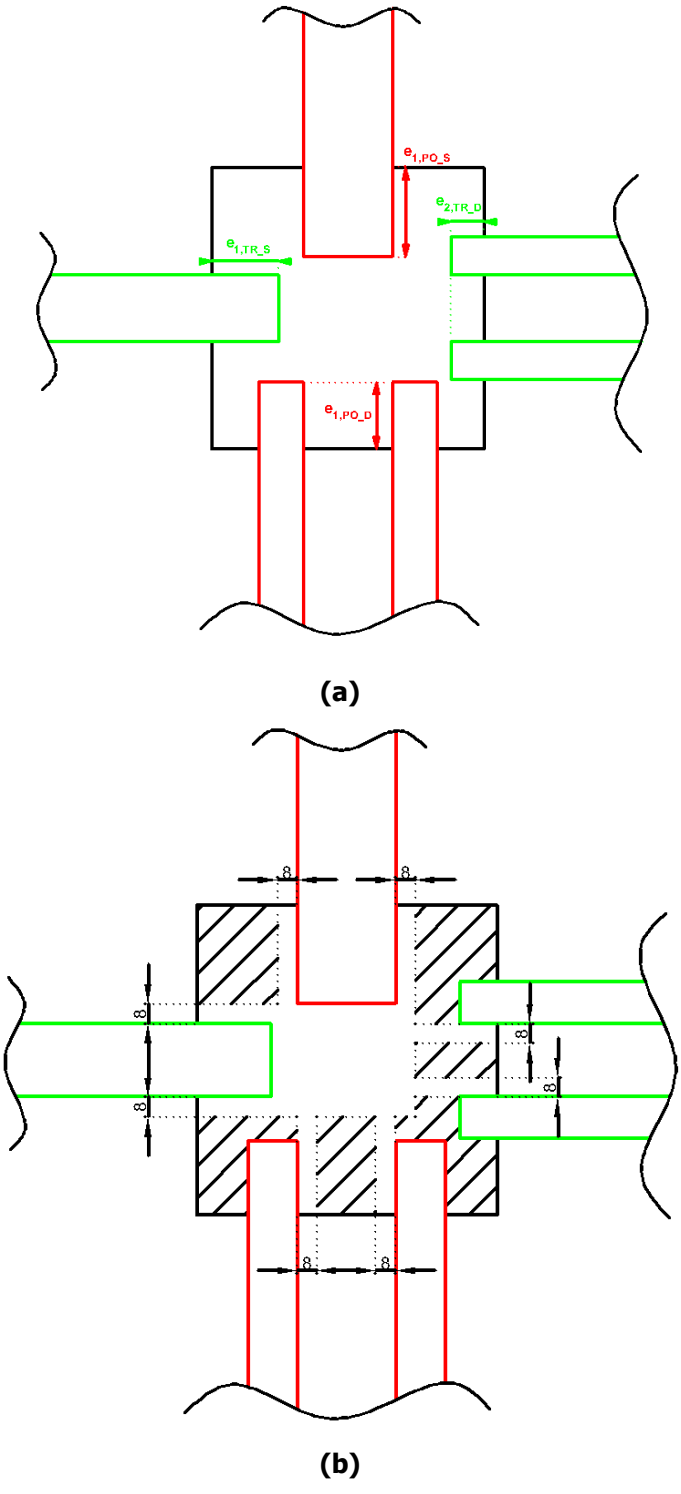

Figure 75. First and second steps of the joint geometry generation: implementation of the calculated member edge distances (a) and assumed joint thickness t (b).

The second step involves the implementation of the assumed joint thickness t equal to 8mm. The lines corresponding to the joint thickness were extended to reach the corresponding lines from the opposite

joint. The remainder was then subtracted from the rest of the line, resulting in Fig. 75 b). On the third step, the edge distances of the joint were added, and the unnecessary parts were removed, resulting in the fourth step (Fig. 76b).

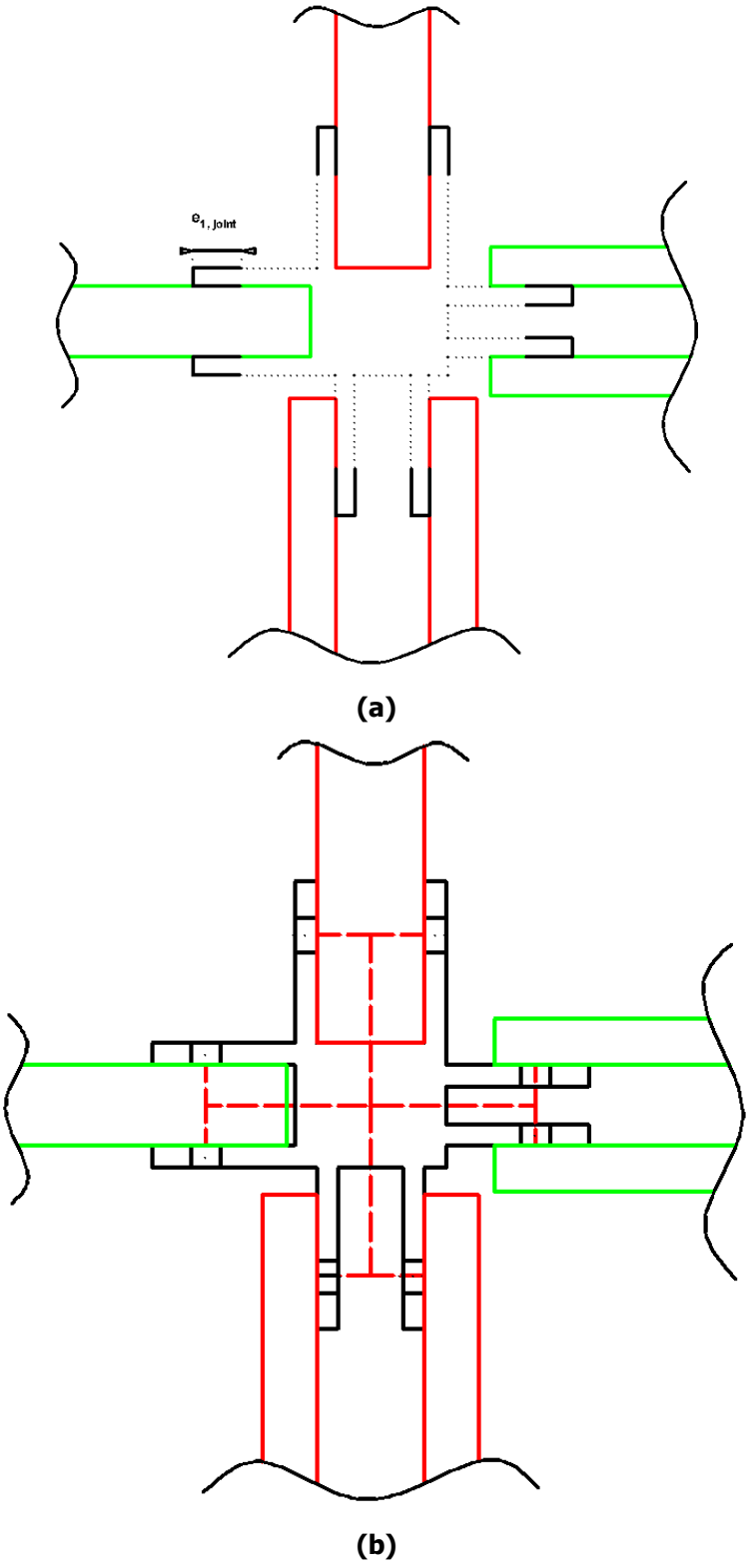

Figure 76. Third (a) and fourth (b) steps of the joint geometry generation: implementation of the joint edge distances and finalization of the joint geometry.

7.3 Final configuration of the joint

The final configuration of the joint involves the joint with all the edge distances implemented, as well as the thread holes and the geometric generator lines. The following Fig.72 depicts the full dimensions of the joint as it will be manufactured. For this reason and to avoid stress concentration on the edges, the joint edges have been filleted with a radius of 2mm. This will enable any possible CNC router machine or 3D printer to more easily manufacture it, along with the provided tolerances.

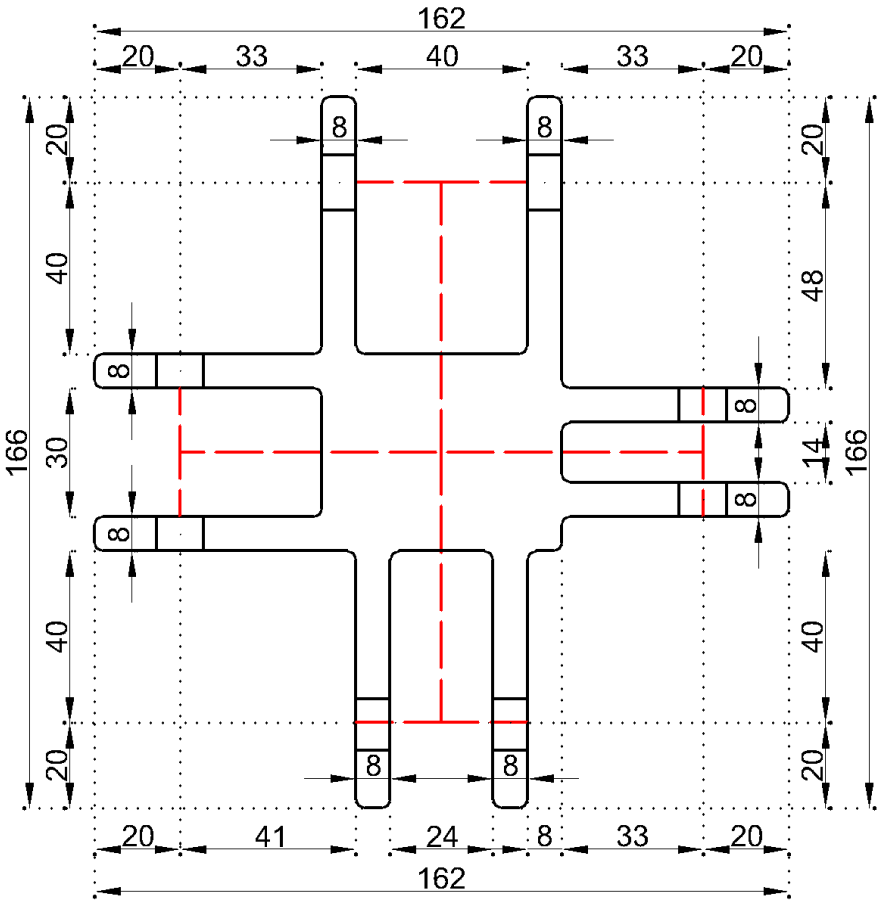

Figure 77. Final geometry of the joint in top view with all dimensions.

As seen above, the initial length and width of 170mm were slightly reduced to conserve as much space as possible, thereby minimising material consumption. This does not significantly affect the geometry of the structure. In the case of major changes, the members can also be shortened, and the overall geometry will remain the same. Below, in Fig.73, the front, rear, left, and right side views are displayed, showing the edge distances e_2 applied to the joints, as well as the thickness of 32mm, which finalises the geometry of the joint.

It is advised that a tolerance of ± 2mm should be applied to both the polar and translational "single" element sockets. This will allow for a clearer fit during the assembly process after manufacturing the joint and the entire structural elements.

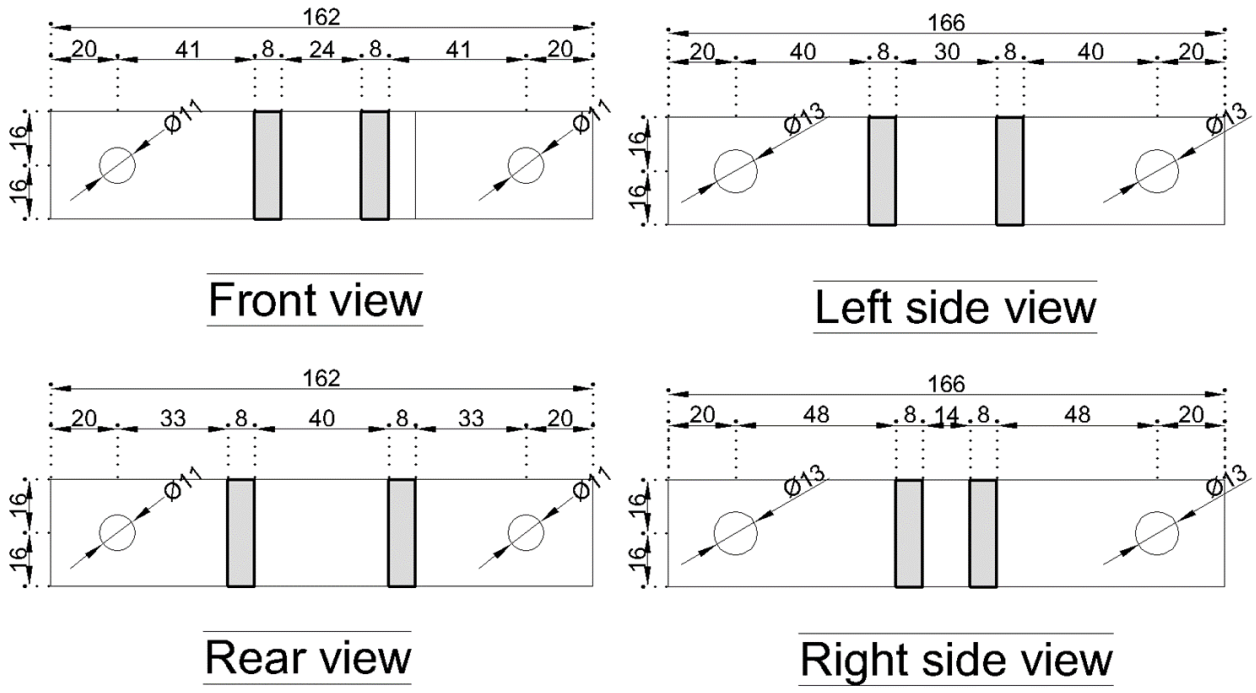

Figure 78. Final side views of the joint.

7.4 Integration with scissor elements

For the integration with the polar and translational scissor-like elements, common nuts, washers, and bolts were used, defining a pinned connection, enabling the members to rotate freely around the axis that goes through the thread. As shown in the Fig.74, the joint geometry defined the required lengths of the bolts. Then the bolts are selected from the catalogues of DIN 933 [24], the washers according to DIN6916 [25] , and the nuts according to DIN6915 [26].

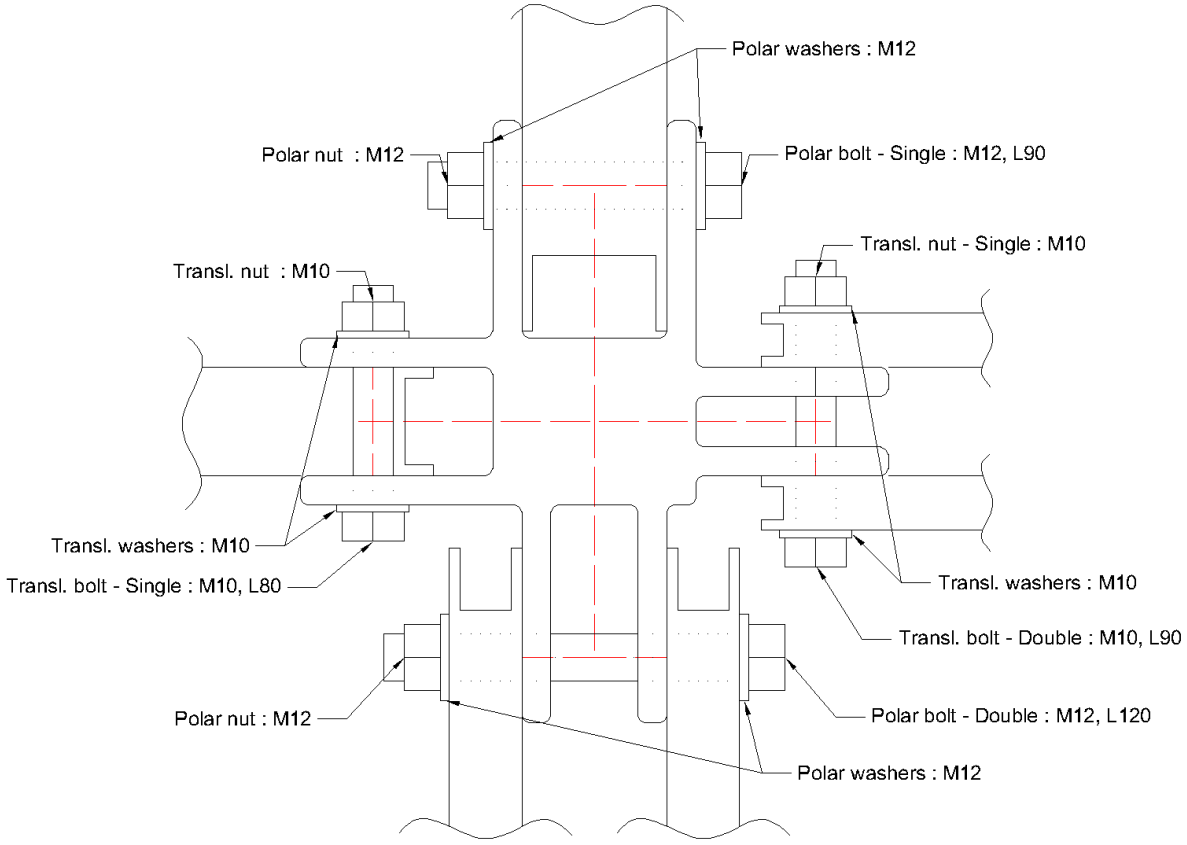

Figure 79. Connection layout of the scissor-like elements with the final joint configuration.

The joint was also modelled and 3D rendered in order to simulate the assembly process in a CAD environment. This way, precision and unexpected problems would have been pointed out in order to revise the drawings if needed. The modelling did not show any kind of problems or inaccuracies, and as a result, the geometry did not change. The top view, as well as an axonometric view of the rendered joint, is displayed in Fig.75.

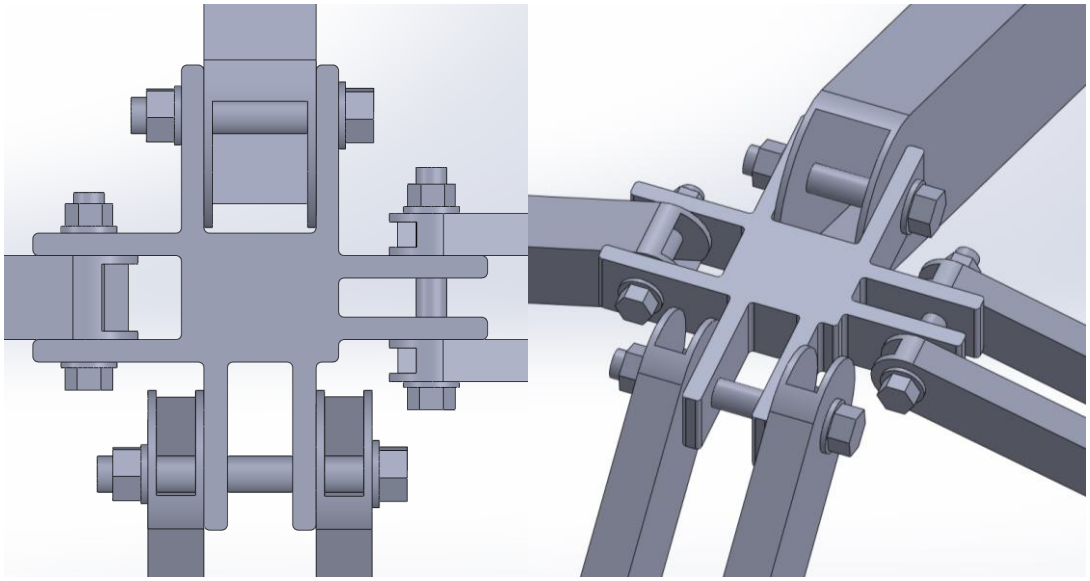

(a) **(b)**

Figure 80. Top view (a) and axonometric view (b) of the three-dimensional rendered joint.

7.5 Revision of the structural response considering the actual joint weight

After the finalisation of the geometry of the joint and the members, the structure is weighed in categories of members. The purpose of this process is to first compare the overall weight of the structure with the relative single-member scissor-like element structure that has been studied by Pantazis Georgios in his diploma thesis development [15], as well as to revise the joint weight assumed as a dead weight in Chapter 4. The material quantification and weight estimation of the structure are depicted in Tab. 6-1 and the Weight per component group expressed as a percentage of the total structural weight is displayed in Tab 6-2.

Table 6-1. Weight estimation of the structure.

Descripton	**Units**	**Weight per unit (kg)**	**Total weight per group (kg)**
Polar aluminum member 80X40X3	35	2.65	92.82
Polar aluminum member 60X20X3	70	1.70	119.00
Translational aluminum member 35X30X3	32	1.33	42.56
Translational aluminum member30X15X3	64	0.88	56.32
Joint	80	1.51	120.80
Bolt M12, L90	80	0.08	6.64
Bolt M12, L120	115	0.11	12.08
Bolt M10, L80	80	0.05	4.26
Bolt M10, L90	112	0.06	6.53
Washer M12	390	0.007	2.73
Washer M10	384	0.004	1.69
Nut M12	355	0.02	8.27
Nut M10	352	0.01	4.08
Cable 6.1mm	28	0.36	10.16
Cable tip 6.1mm	56	0.10	5.60
Covering membrane	1	100.93	100.93
Total			**594.48**

Table 6-2. Weight per component group expressed as a percentage of the total structural weight.

Descripton	Total weight per group (kg)	Weight per groupas a percentage of the total weight (%)
Polar aluminum member 80X40X3	92.82	18.15
Polar aluminum member 60X20X3	119.00	23.26
Translational aluminum member 35X30X3	42.56	8.32
Translational aluminum member30X15X3	56.32	11.01
Joint	120.80	23.62
Bolt M12, L90	8.00	1.56
Bolt M12, L120	14.95	2.92
Bolt M10, L80	4.16	0.81
Bolt M10, L90	6.50	1.27
Washer M12	2.73	0.53
Washer M10	1.69	0.33
Nut M12	8.27	1.62
Nut M10	4.08	0.80
Cable 6.1mm	10.16	1.99
Cable tip 6.1mm	5.60	1.09
Covering membrane	100.93	19.73

As seen in Tab. 6-2, the largest percentage of the overall weight of the structure belongs to the polar double-member scissor-like elements, with a percentage of 20%; a similar 18% belongs to the polar single-member scissor-like elements; the translational single and double-member scissor-like elements hold 8% and 10%, respectively. The most interesting of these is the percentage of the overall joint weight, which is around 13%. This means that the weight of the joint is equivalent to adding another aluminium member category. Tab. 6-3 displays the comparison between the overall joint weight without eccentricities and the overall weight of the polar and translational members of this structure, with the structure developed and studied under the development of the diploma thesis of Mr. Pantazis Georgios [15].

Table 6-3. Comparison of total weight per group for the single- and double-member SLE structures.

Descripton	**Total weight per group (kg) for the single-member SLE structure** [15]	**Total weight per group (kg) (single and double-member SLE structure)**
Polar members	188	212
Translational members	70	99
Joint	117	121
Total weight of the structure	540	595

The initial assumption regarding the joint weight G_{joint} has been obtained as 13.74 × 10^-3 kN. The variable parameter that defines the joint weight is its volume V_{con}, which has been assumed as 175cm^3. The final volume of the joint has been calculated through the CAD software as 198.14cm^3. This means that the G_{joint} needs to be revised as 15.55x10-3kN. The change is minor enough that the structural response of the deployable structure is slightly changed, as can be verified in Tab. 6-4.

Table 6-4. Revised structural response of the structure after joint implementation.

	Polar SLEs		**Translational SLEs**		**Bracings (cables)**	
Load Combination	Max. Von Mises (MPa)	Ratio	Max. Von Mises (MPa)	Ratio	Max. Von Mises (MPa)	Ratio
ULS_LC1	113.16	**0.71**	68.59	**0.43**	18.60	**0.04**
ULS_LC2	121.99	**0.76**	98.75	**0.62**	67.99	**0.14**
ULS_LC3	137.19	**0.86**	92.10	**0.58**	96.89	**0.19**
ULS_LC4	58.55	**0.37**	69.89	**0.44**	227.87	**0.46**
ULS_LC5	101.82	**0.64**	93.06	**0.58**	89.70	**0.18**
ULS_LC6	93.74	**0.59**	96.39	**0.60**	246.52	**0.49**
ULS_LC7	90.87	**0.57**	72.75	**0.45**	69.86	**0.14**
ULS_LC8	139.85	**0.87**	131.40	**0.82**	17.57	**0.04**
ULS_LC9	82.89	**0.52**	51.84	**0.32**	30.75	**0.06**
ULS_LC10	130.86	**0.82**	99.34	**0.62**	155.16	**0.31**
ULS_LC11	93.42	**0.58**	78.51	**0.49**	79.07	**0.16**
ULS_LC12	88.06	**0.55**	87.53	**0.55**	236.75	**0.47**

8 NUMERICAL INVESTIGATION OF THE JOINT

8.1 Numerical simulation of the joint with its corresponding elements

The design checks and the structural analyses from previous chapters cannot verify the structural integrity of the proposed joint outlay. Therefore, a numerical simulation of the joint with its corresponding elements in both polar and translational directions is conducted. The analysis scheme involves a simple stress analysis using a pressure load at the center of the joint, as would be done in a laboratory experiment. The simulation results can be verified through an experimental process. This verification would confirm the trustworthiness of the results and the overall simulation. Figure 81 below shows the simulation of the joint and its corresponding members.

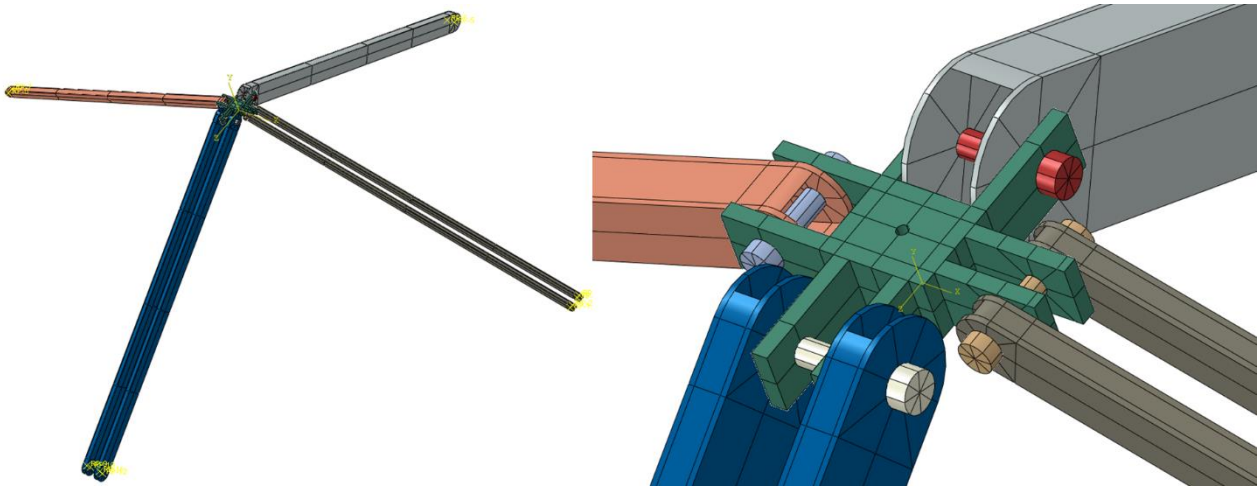

Figure 81. Numerical model of the joint and its corresponding members.

8.2 Material input in the numerical model

8.2.1 Polar and translational members

The material used for both polar and translational members, as mentioned in the previous chapters, is the EN-AW 6063-T5 aluminum alloy, which features a characteristic yield strength of f_y=160 MPa and behaves as an isotropic material. The material law, and consequently the plastic branch used for the simulation, is bilinear without a hardening branch (perfectly plastic), with a yield strength equal to 130 MPa. The Young's modulus considered is E=70 GPa, while Poisson's ratio is v=0.33.

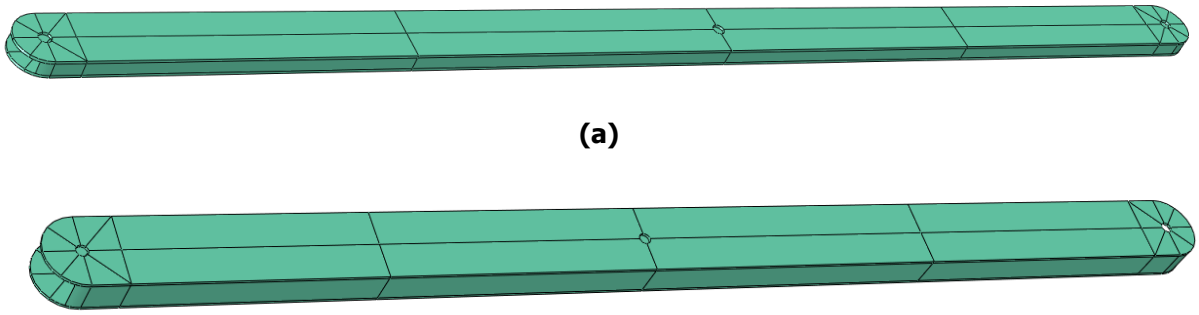

(a)

(b)

Figure 82. Numerical models of the polar elements: (a) single-member and (b) double-member configurations.

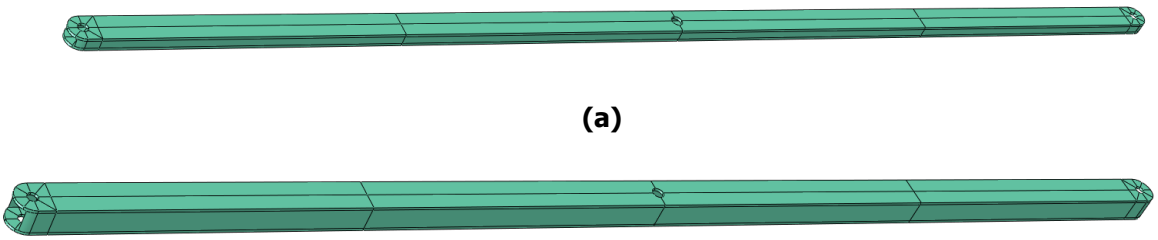

(a)

(b)

Figure 83. Numerical models of the translational elements: (a) single-member and (b) double-member configurations.

8.2.2 Steel bolts

The material used for the steel bolts is grade 8.8, with a nominal yield strength of fyb=640 MPa. The bolts are modeled as an isotropic material using a bilinear plastic law without hardening (perfectly plastic behavior), maintaining a constant stress equal to the yield strength of 640 MPa in the plastic range. The Young's modulus is taken as E=210 GPa, and the Poisson's ratio is v=0.3.

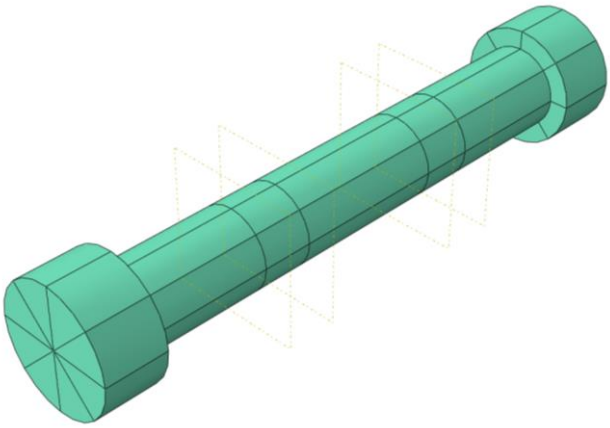

(a)

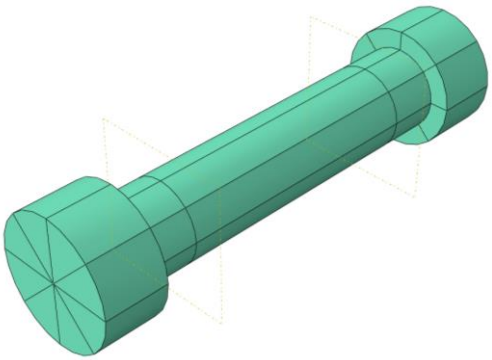

(b)

Figure 84. Numerical models of the bolts used in the polar elements: (a) double-member and (b) single-member configurations.

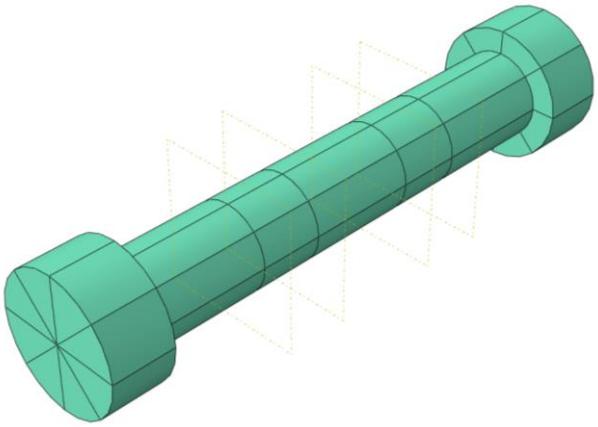

(a)

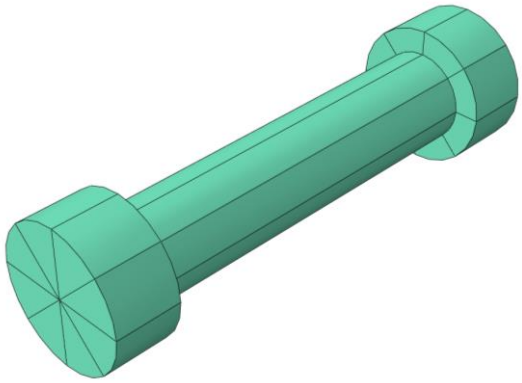

(b)

Figure 85. Numerical models of the bolts used in the translational elements: (a) double-member and (b) single-member configurations.

8.2.3 Steel joint

The material used for the joint is S235 structural steel, with a characteristic yield strength of fy=235 MPa. The joint is modeled as an isotropic material following a bilinear plastic law without hardening (perfectly plastic), where the stress remains constant at 235 MPa after reaching the yield point. The Young's modulus is E=210 GPa, and the Poisson's ratio is v=0.3.

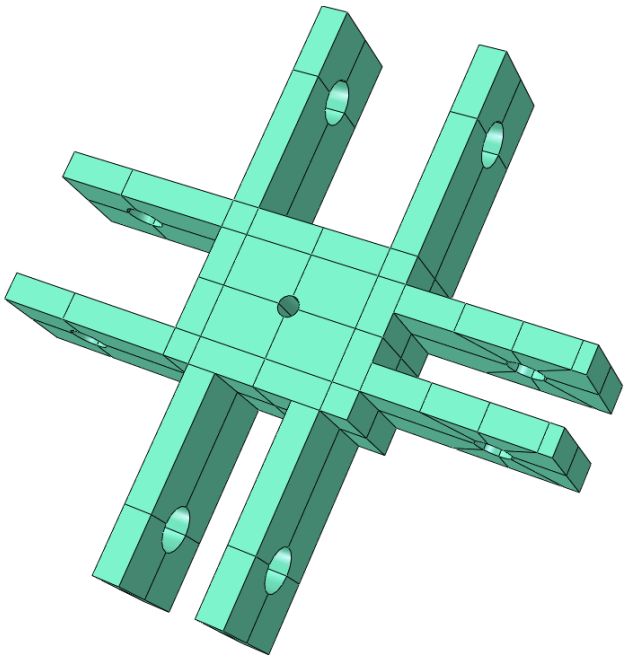

Figure 86. Numerical models of the joint.

8.3 Discretization and finite elements

8.3.1 Member discretization (mesh)

Each part should be decided on whether it would use a free meshing type of mesh generation or be "partitioned" into discrete meshing areas, as Abaqus [27] allows. This enables the user to mesh each partitioned area independently and to use different, case-appropriate meshing techniques in each. For easier application of these techniques, the original geometry of the joint was adopted with some minor changes. Specifically, the fillets present at the edges, as shown in Fig. 72, were neglected. This adjustment made it easier for the meshing algorithm to form undistorted elements. Using the same approach, the parts were partitioned mostly at their thread holes and at the areas that would later serve as interaction master and slave surfaces, such as those for the interactions between the members and the joint.

8.3.2 Finite elements

The element types used are both first-order solid finite elements. For the members, the C3D6 solid finite element was used, while for the joint and the bolts, the C3D8R solid finite element was used. The C3D6 consists of a solid finite element using linear regression for the calculation of displacements in each direction of its 6 nodes. The element is a triangular prism element, as shown in Fig. 87, which is considered easier to solve for large geometries, where accuracy is not the key element of the analysis.

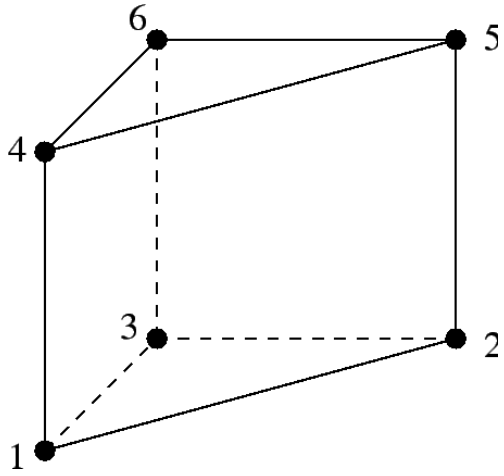

Figure 87. Six-node wedge element C3D6 [27].

The C3D8R consists of a solid finite element using linear regression for the calculation of displacements in each direction of its 8 nodes. The element is a rectangular cubic element, as shown in Fig. 88, which is the appropriate one for the accuracy demanded in the calculation of stresses in the joint. The element is appropriate for complex geometries and for the calculation of stresses. In comparison with the full integration element C3D8, the C3D8R allows for lower computational cost, making the analysis process more feasible.

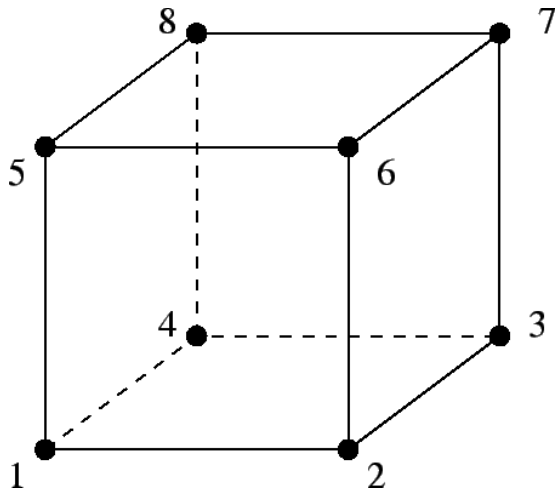

Figure 88. Eight-node brick element C3D8 [27].

The meshing technique involved the sweep method of meshing using the median axis algorithm. The sweep method allows for better control of the local density of the mesh and the ability to instantaneously generate certain types of elements. The sweep meshing also allows for a smoother mesh based on the geometry, and it uses as its base the two-dimensional initial surface. The algorithm used for the mesh generation was the median axis algorithm. This algorithm is applied for the generation of high-precision meshing. The process involves the division of the surface into distinct subsurfaces that are appropriate for the application of hexaedral elements. The division process ceases when the geometry is simple enough; the algorithm generates the mesh faster than other algorithms, such as the "advancing front" algorithm. The results are defined as more trustworthy and reliable. An example of the difference between the advancing front algorithm and the median axis is depicted in Fig. 89 from the Abaqus manual.

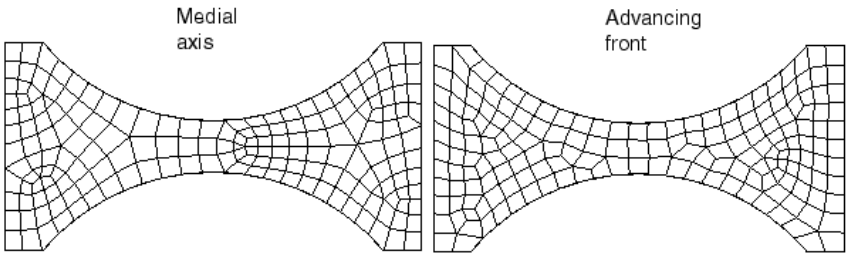

Figure 89. Medial axis algorithm (left), and the advancing front algorithm (right).

The mesh in the joint and the bolts used an approximate seed size of 1.5mm as shown in Fig. 90-92, trying to ensure no converging issues as well as meshing errors.

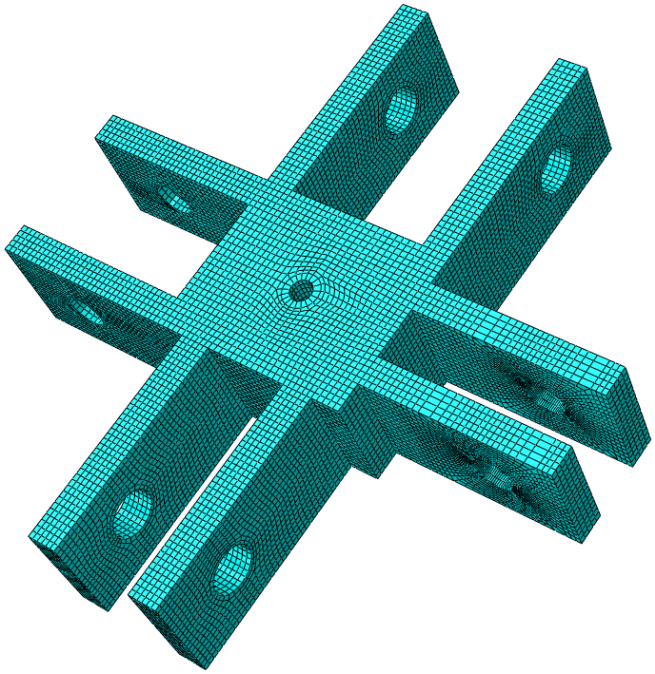

Figure 90. Finite element mesh of the joint.

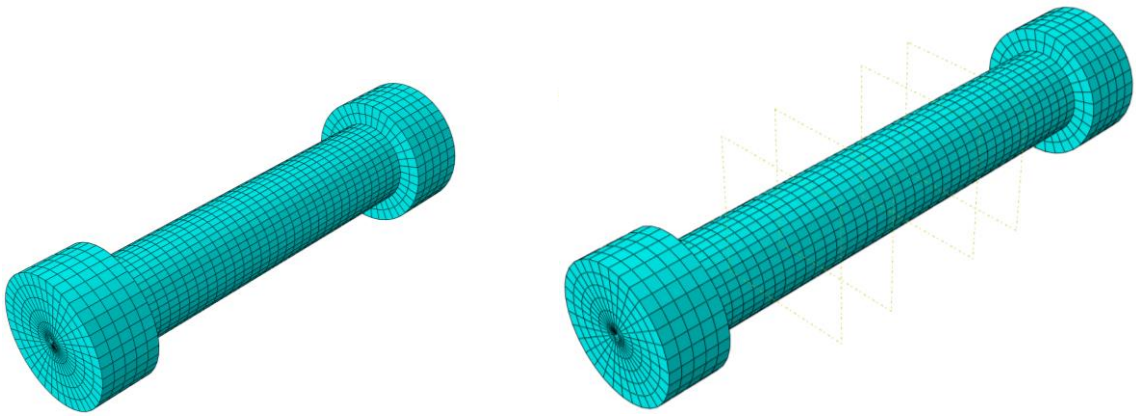

Figure 91. Finite element mesh of single-member (left) and double-member (right) translational SLE bolts.

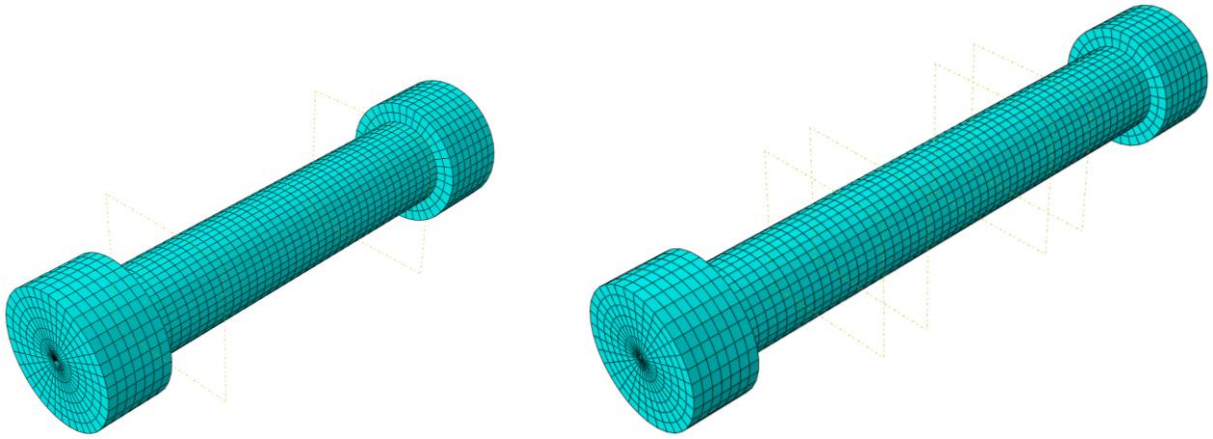

Figure 92. Finite element mesh of single-member (left) and double-member (right) polar SLE bolts.

The same sweep meshing technique was used for the polar and translational elements, assigning the C3D6 element to the parts. All the parts have a seed length of 5mm, creating a dense mesh relative to their size. Figs 93-94 depict the meshed parts.

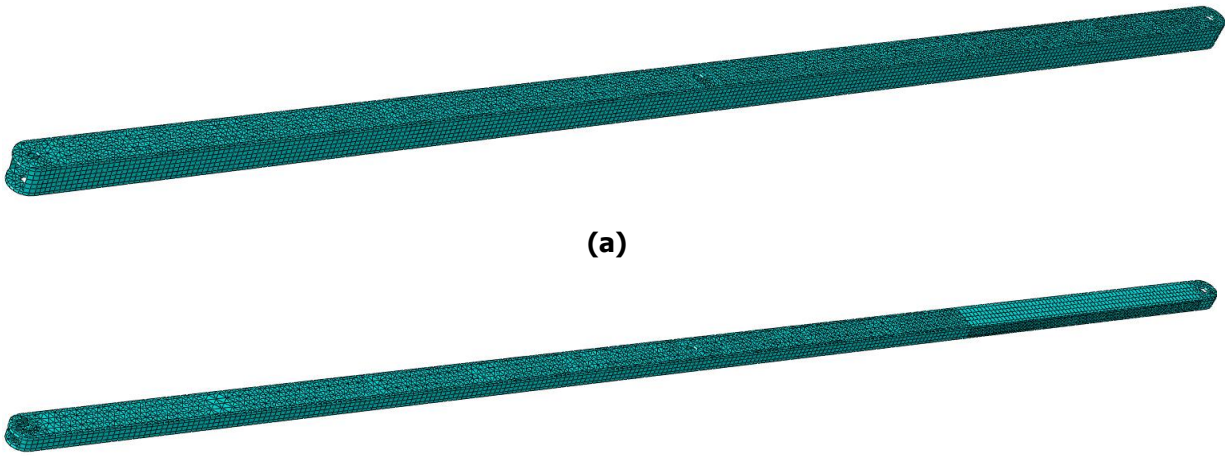

(a)

(b)

Figure 93. Finite element mesh of single-member (a) and double-member (b) translational SLE elements.

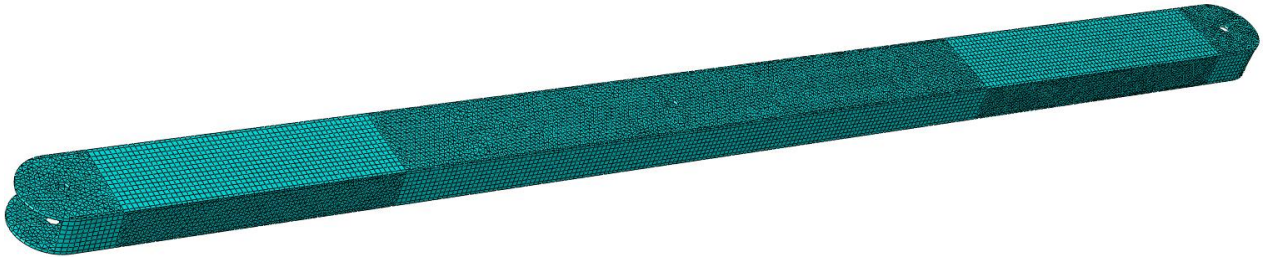

(a)

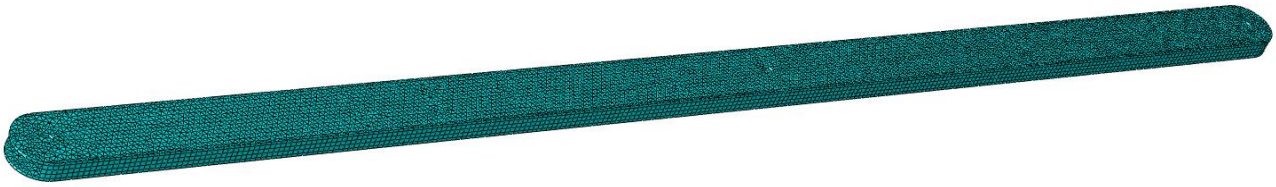

(b)

Figure 94. Finite element mesh of single-member (a) and double-member (b) polar SLE elements.

8.4 Boundary conditions

To simulate the rotation of each bar around the pin axis of each corresponding joint in the structure, a hinge (pin) connection was utilized. This connection allows rotation around the respective X and Y axes, specifically, rotation of the Y-direction bars about the X-axis and X-direction bars about the Y-axis, while constraining all other degrees of freedom. The boundary conditions were applied at the center of the hole of each bar by linking the rotation surface to a reference point via a rigid body constraint (pin type). Only half of the thread hole length is utilized because in the structure, the member will never exceed this limit, as shown in Figs 95-96.

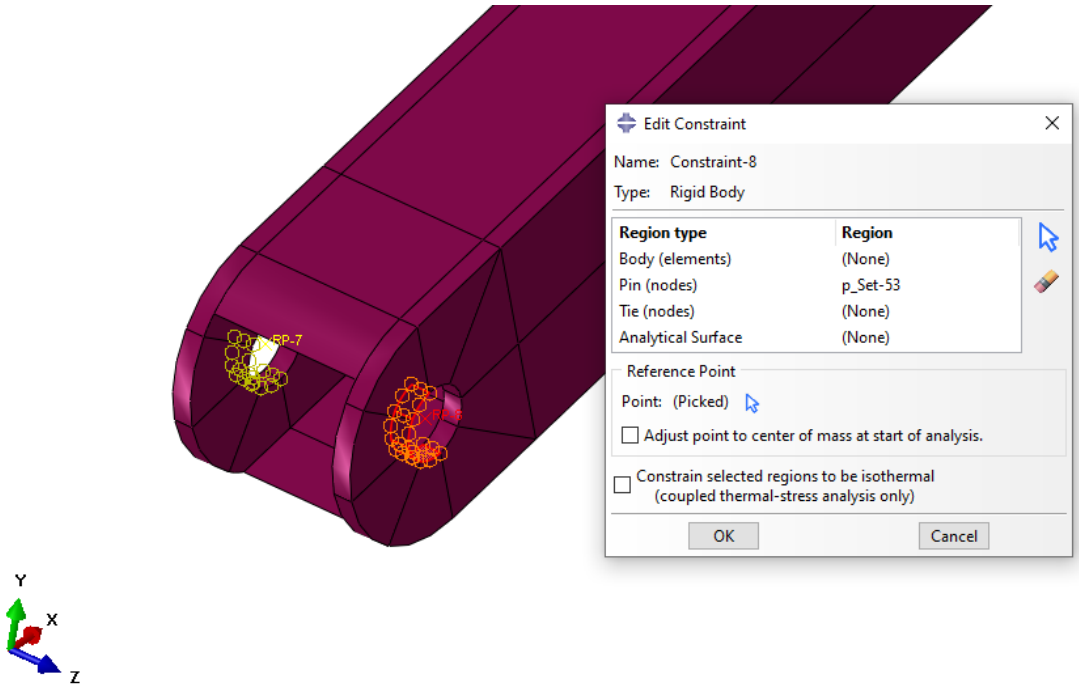

Figure 95. Rigid body constraint of the thread holes.

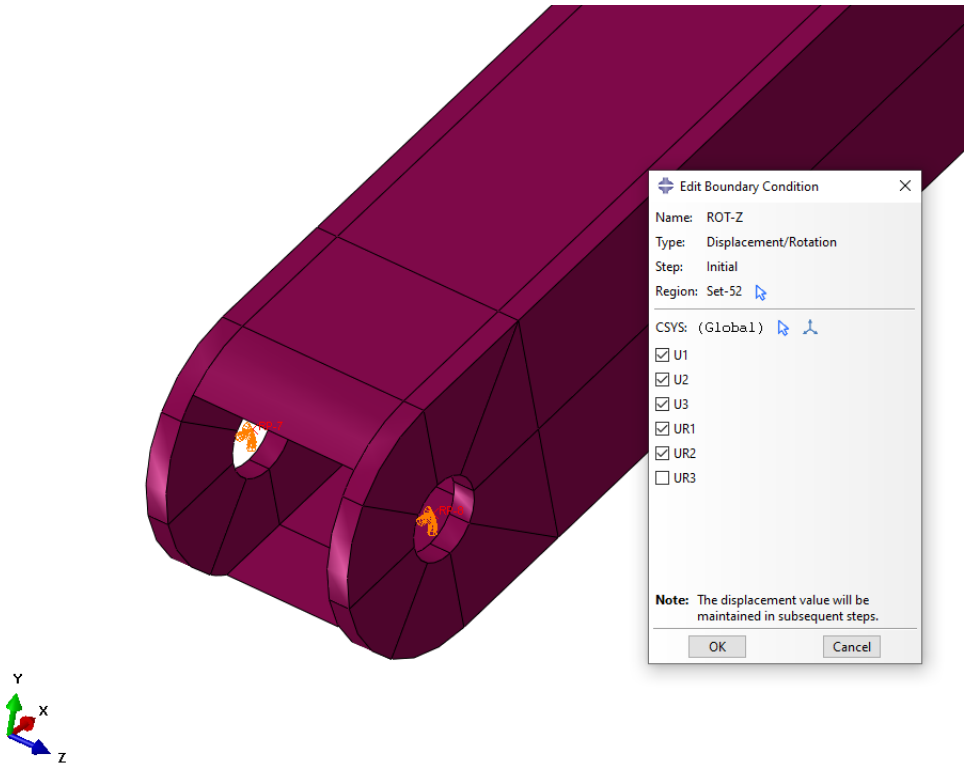

Figure 96. Boundary conditions at the edges of the elements.

8.5 Contact definitions

The interactions between the elements were fully simulated using two corresponding surfaces each time. The first consists of the master surface, which is the stiffer surface and the slave surface, which corresponds to the less stiff surface. The full contact definitions are described in Tab. 7-1 and depicted in Fig. 97.

Table 7-1. Surface interaction definition.

	Master	**Slave**
a	Member surface	Bolt head surface
b	Member thread holes	Bolt surface
c	Joint thread holes	Bolt surface
d	Member surface	External joint surface
e	Member surface	Internal joint surface

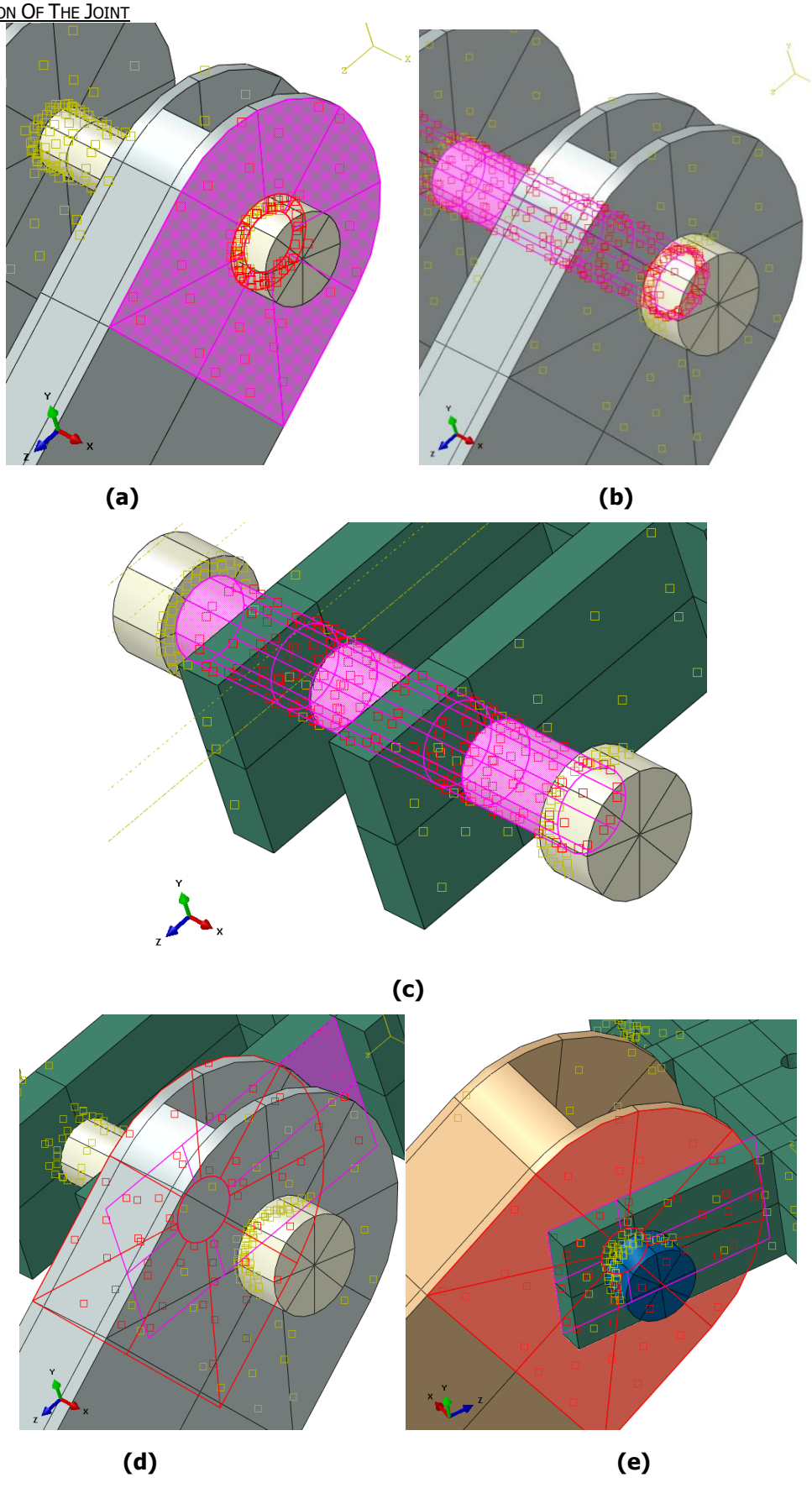

Figure 97. Contact definitions between the parts.

Regarding the contact properties, the coefficient of friction proposed in the literature is 0.61 for static friction and 0.47 for kinetic (sliding) friction under drying conditions. However, in this case, due to the tolerances advised in Chapter 6, a much lower coefficient of friction of 0.1 was selected as shown in Fig. 98 as well as a penalty friction that allows for some elastic slip after the contact.

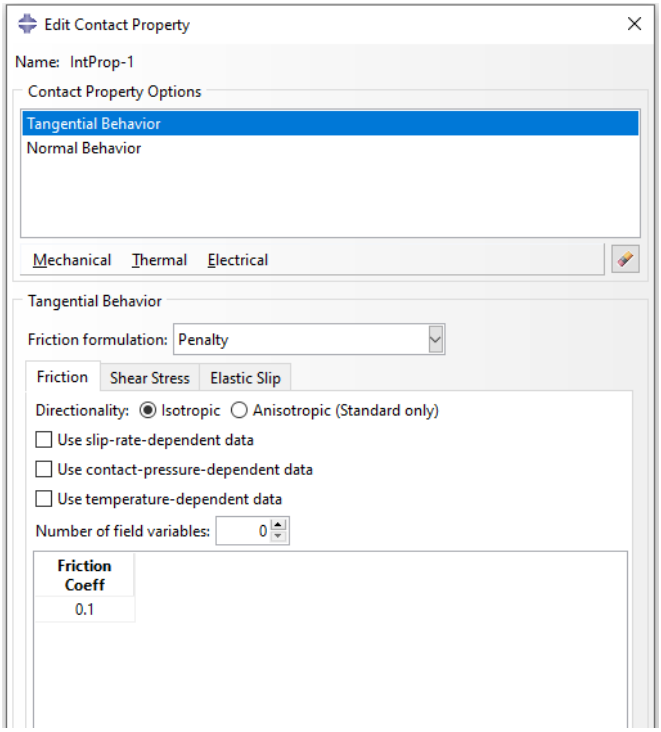

Figure 98. Tangential behavior contact property definition.

The normal behaviour was simulated as a hard contact. This means that the parts cannot penetrate each other while allowing their separation after contact.

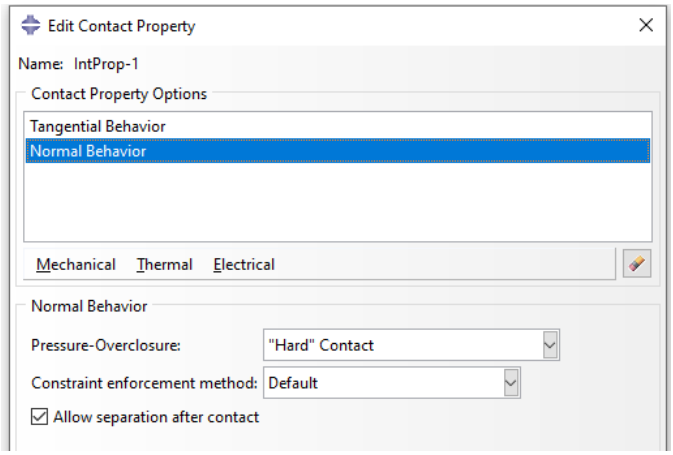

Figure 99. Normal behavior contact property definition.

8.6 Load application

To simulate an experimental process as performed by similar tests in joints of deployable structures [13], the point of load application was simulated as a concentric surface with a diameter of 6mm to the bottom of the central thread hole of the joint that would originally house the hook of anchoring the braces. The direction of the loading is the +Y as shown in Fig. 100 in order to provide tension to the members and bend the joint. The load applied to the joint was such that it would significantly exceed its yield point of 235 MPa, and it was chosen at 500 MPa in order to drive into yield as many parts as possible to extract the most realistic load path.

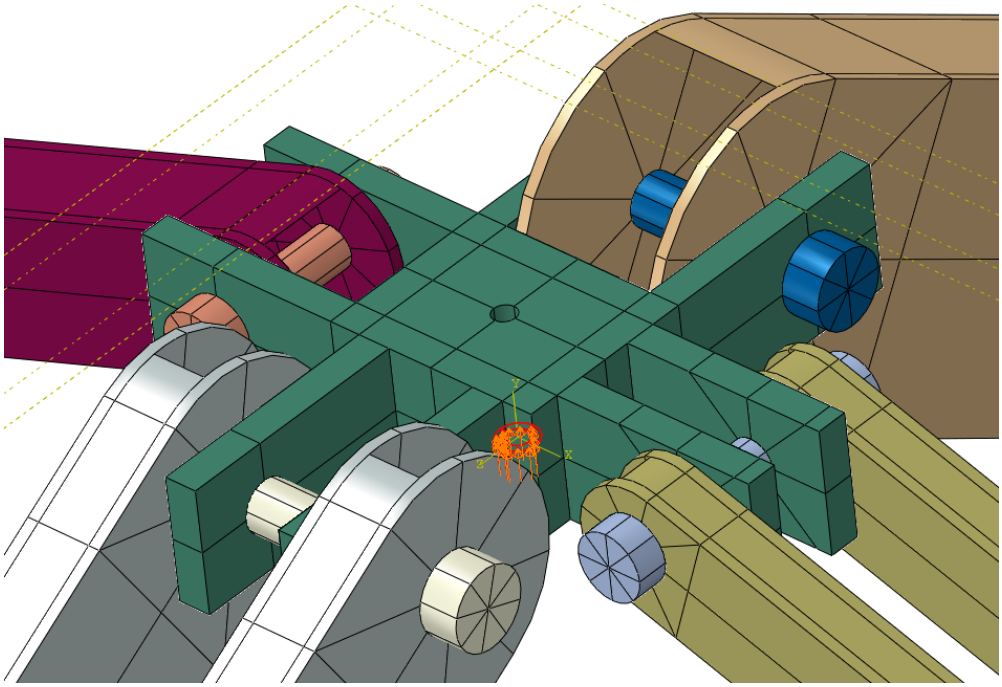

Figure 100. Load application to the joint.

8.7 Analysis type and solution method

The simulation took advantage of the static, general type of analysis provided by Abaqus, where it is applied, where both linear and nonlinear analyses can be conducted, depending on the nature of the simulation. According to the Abaqus manual [27], this type of analysis ignores all time-dependent properties of the materials and can implement properties such as complex plasticity and hysteretic behaviour of elastic-plastic materials. Regarding the non-linear analysis, the common full instead of a modified Newton-Raphson load controlled was implemented in order to take advantage of the faster convergence time in comparison with the modified and the quasi-Newton Raphson non-linear schemes. The full Newton-Raphson process is described in Fig. 101.

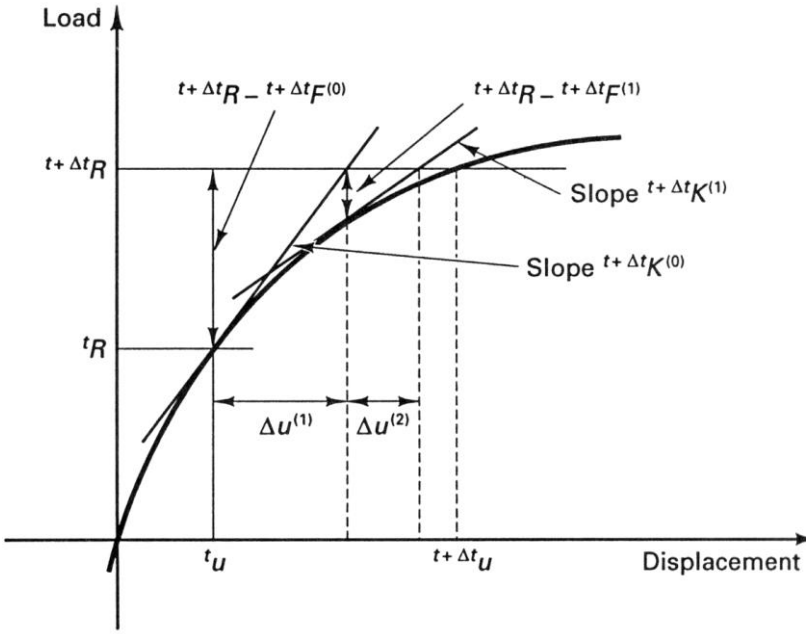

Figure 101. The Newton-Raphson method [28].

8.8 Numerical results of the geometrically and material non-linear analysis

The analysis that was selected is the geometric and material nonlinear analysis (GMNA) due to the nature of the structure. The purpose is to extract a load path that describes the behaviour of the assembly under extreme loading. The load path extraction is described in Tab. 7-2.

Table 7-2. Summary of load calculation parameters.

Term	**Formula**	**Meaning**
Magnitude	$P(GPa) \cdot A(mm^2) \cdot 1000$	The 100% force capacity of the setup.
Current Load	$Time \cdot P(GPa) \cdot A(mm^2) \cdot 1000$	The actual force applied at a specific increment.

Where P indicates the pressure applied to the concentric surface, time is the analysis step time, and A refers to the area of the concentric surface where pressure occurs. Fig. 102 illustrates imposed load over the displacement at the direction of the application, showing where yielding initiates at the load application point, where local bearing yielding occurs for both single and double-member SLE sockets in the joint, and where local yielding begins at the steel plates of the joint, highlighting the sequential yielding process within the joint.

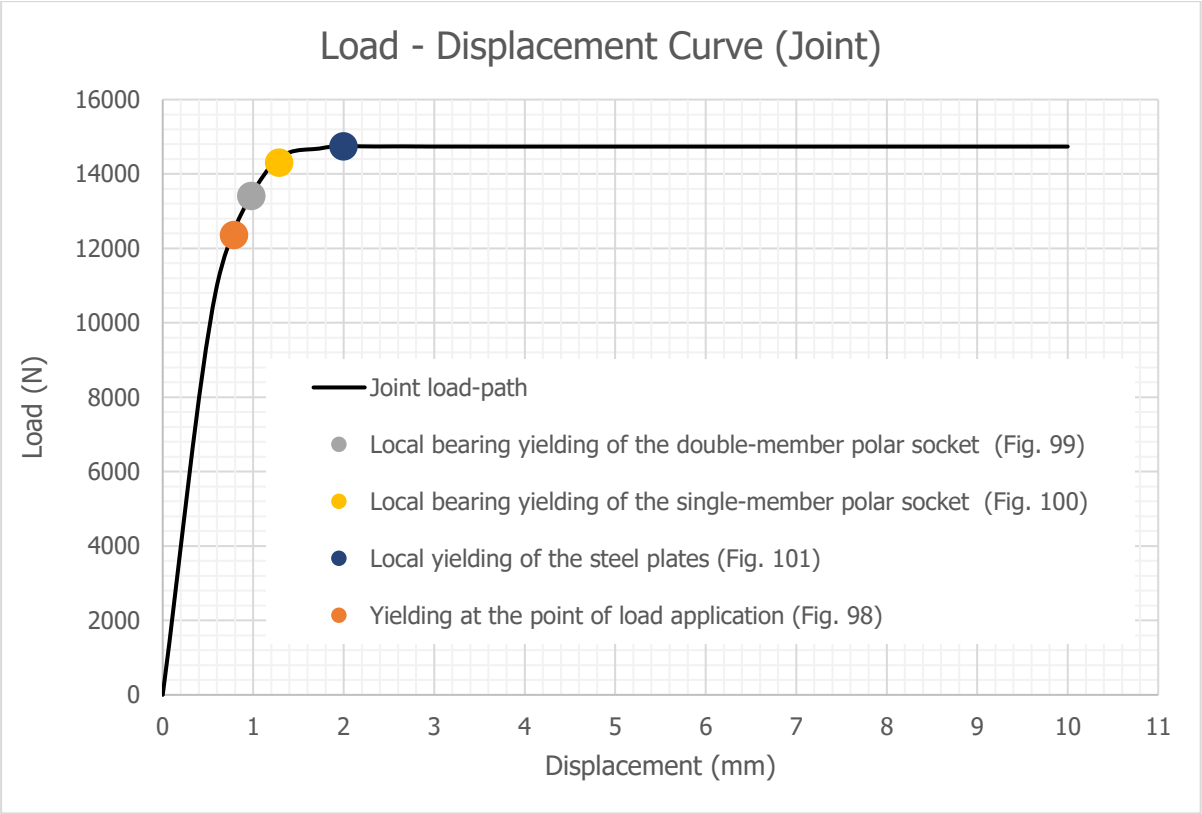

Figure 102. Load displacement curve of the joint.

The yielding of the joint starts at the point of load application on the bottom side of the joint (Fig. 103). At a displacement of 0.63mm while the load applied to the assembly at the time corresponds to about 12400N.

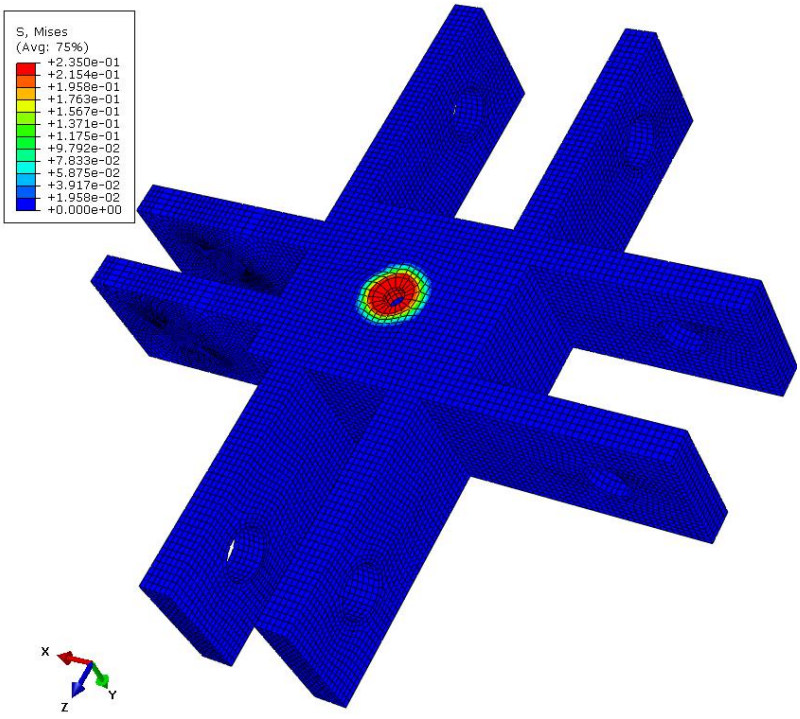

(a)

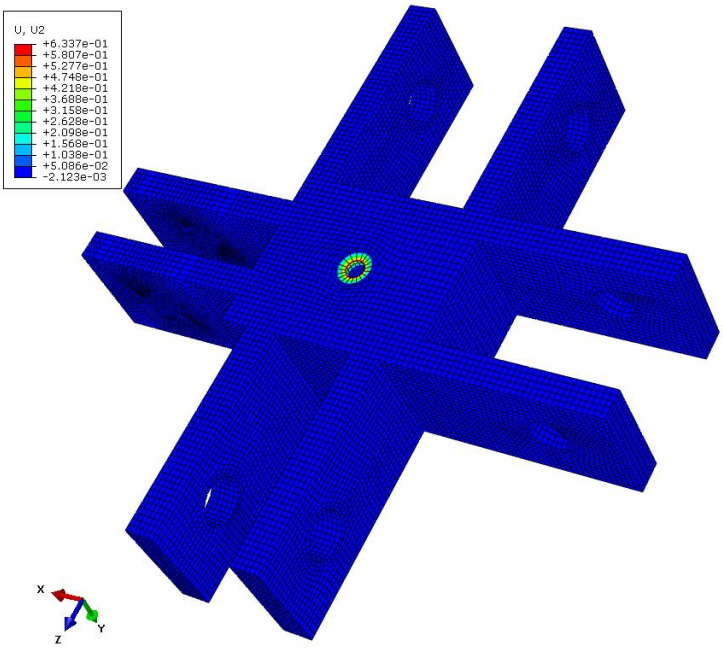

(b)

Figure 103. Yielding at the point of load application: (a) Von Mises stress distribution, and (b) displacements in the direction of the load application.

As the application of the load progresses the bearings of the double-member polar sockets of the joint start to yield (Fig. 99) at a displacement of 0.99mm while the load applied to the joint at the time corresponds to 13400N.

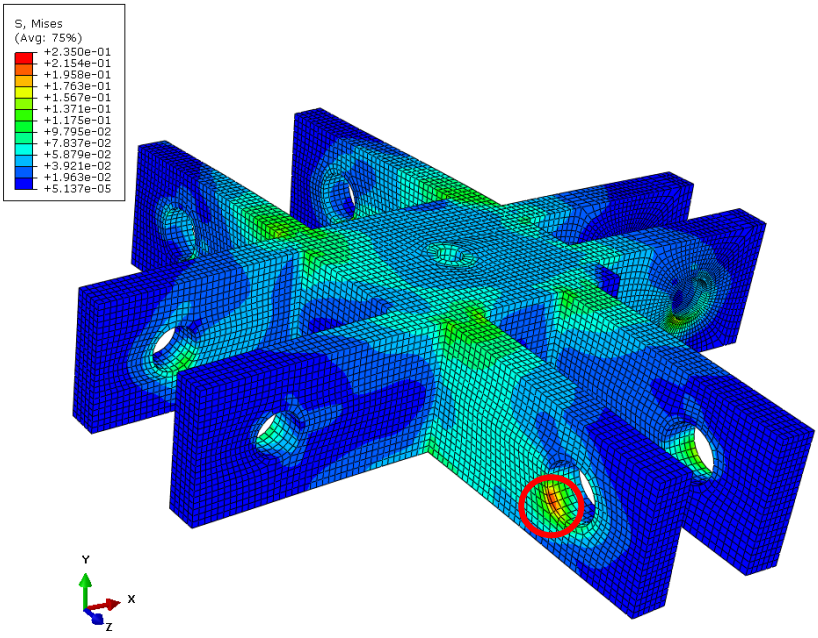

(a)

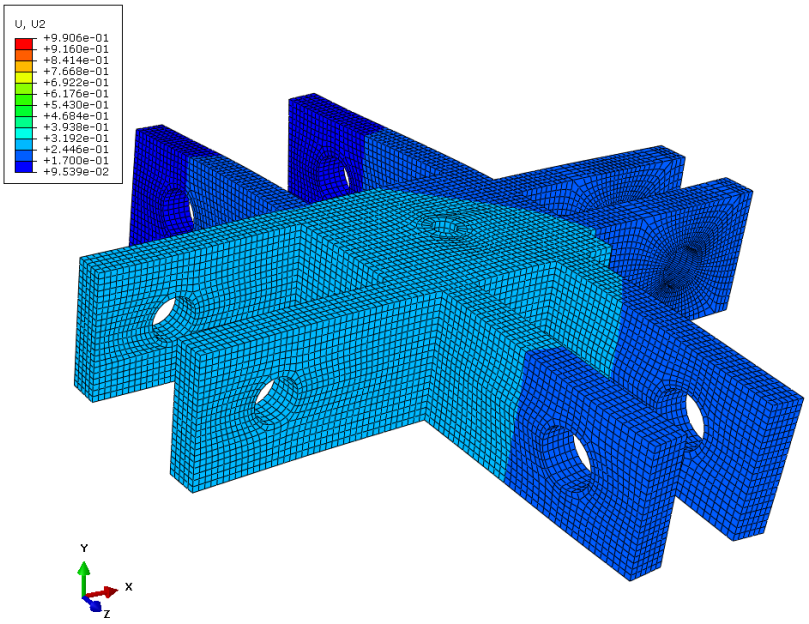

(b)

Figure 104. Local bearing yielding of the double-member polar socket: (a) Von Mises stress distribution, and (b) displacements in the direction of the load application.

The bearing of the single-member polar socket at the joint starts to yield in the same way (Fig. 100). The yielding starts at the bearing at a displacement of about 1.24mm while the load applied at the time is about 14400N.

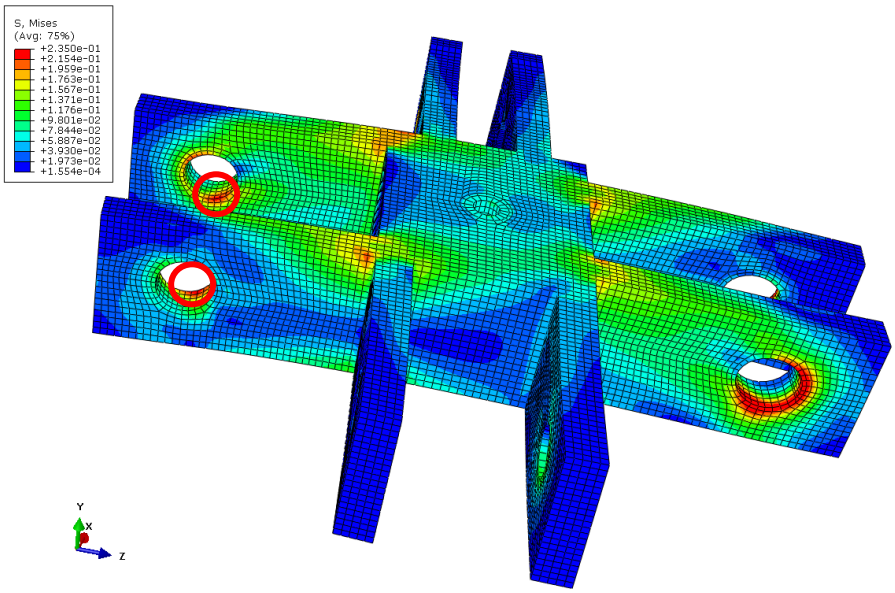

(a)

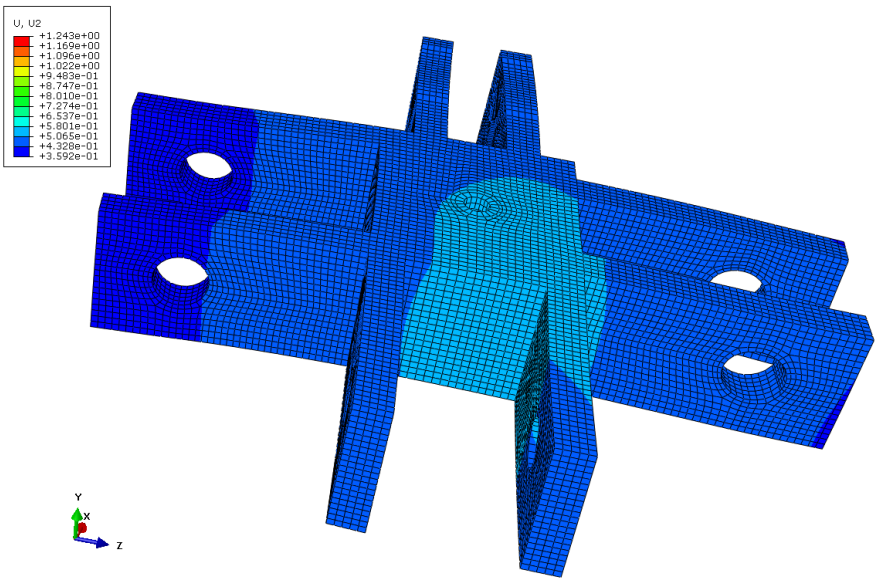

(b)

Figure 105. Local bearing yielding of the single-member polar socket: (a) Von Mises stress distribution, and (b) displacements in the direction of the load application.

Fig. 106a displays a concentration of stresses into the steel plates' connection to the main body of the joint, which progresses into a yielding zone (Fig. 101) at a vertical displacement of 2.01mm, reaching the maximum force capacity of the joint of 14800N.

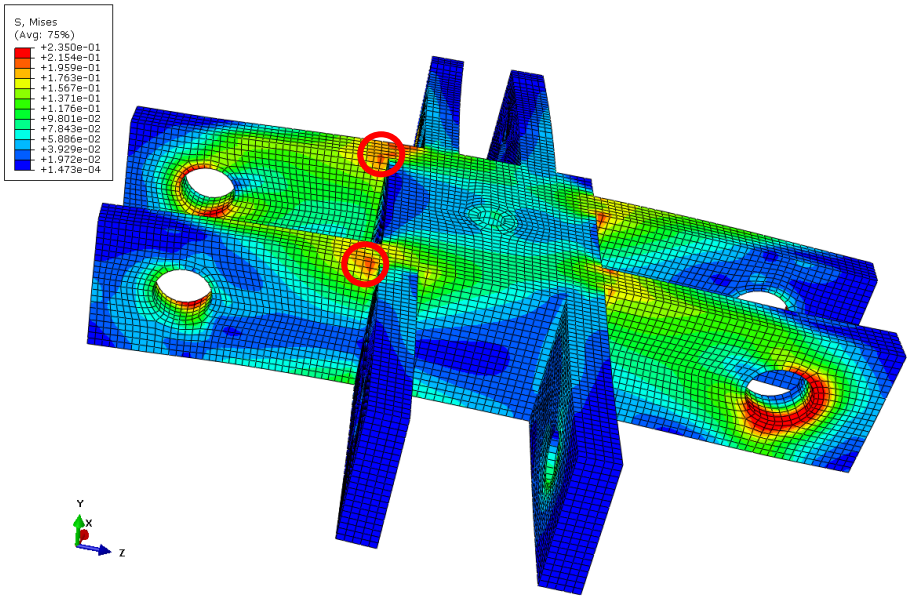

(a)

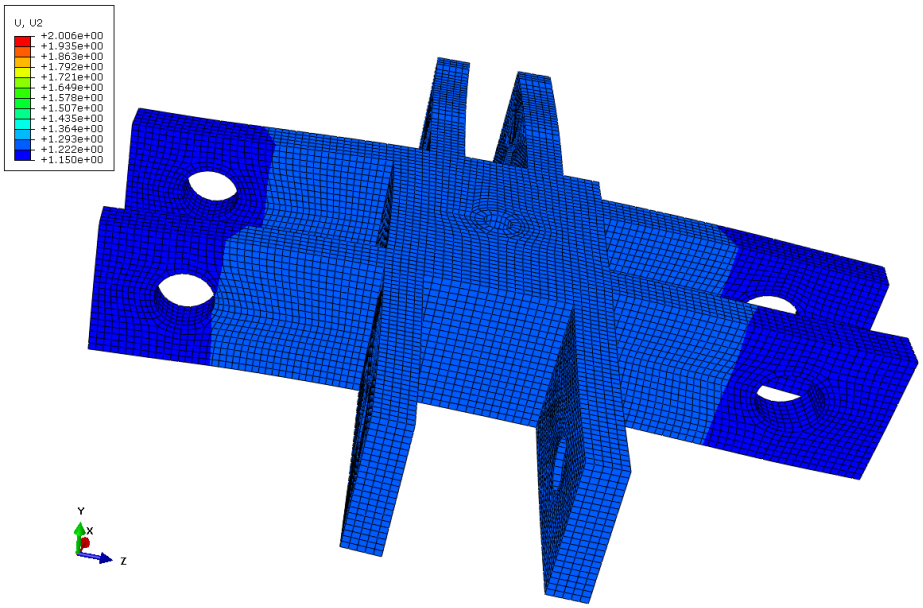

(b)

Figure 106. Local yielding of the steel plates: (a) Von Mises stress distribution, and (b) displacements in the direction of the load application.

Apart from the load path of the joint, the behaviour of the members can be described as follows. While none of the translational members yield or fail, the single-member-SLE polar element yields at its bearings while the analysis progresses, as shown in Fig. 106. The same yielding pattern is observed in the double-member-SLE polar elements, where their thread-hole bearings yield as well (Fig. 107).

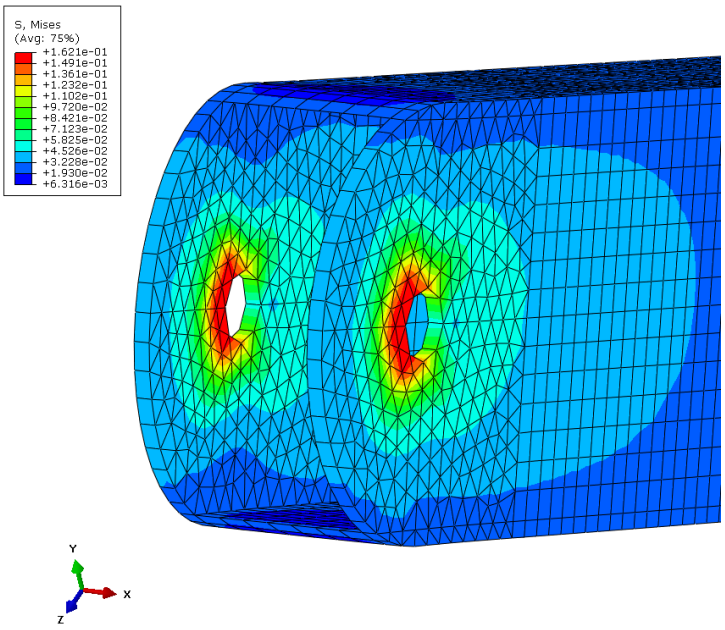

Figure 107. Von Mises stress distribution of the single-member-SLE polar element, indicating yielding at the bearings of the thread holes.

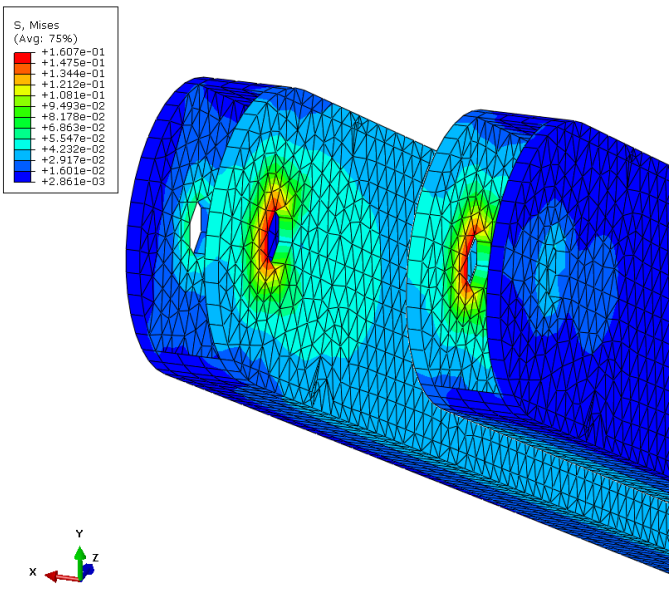

Figure 108. Von Mises stress distribution of the double-member-SLE polar elements, indicating yielding at the bearings of their thread holes.

9 CONCLUSIONS

9.1 Conclusions

This graduate thesis investigates the development of a joint without eccentricities for a scissor-type deployable structure. The main conclusion is that the double-member scissor-like elements, as defined here, should be implemented in both translational and polar directions to achieve the desired structural response. This implementation significantly influences the overall structural performance.

During load application to the structure, it was observed that using double-member SLEs did not yield as symmetric a response under relatively symmetric loading as expected. The live loads from transverse and longitudinal winds most affected the structure. Specifically, the transverse wind load brought the polar elements to their limit during linear analysis, which later proved crucial when they were found to be insufficient in the design process and required replacement with a larger cross-section. The translational elements were affected by the longitudinal wind load, but their replacement was deemed unnecessary. For this reason, the structure was braced with cables and designed in accordance with European design regulations. Geometrically non-linear analysis with imperfections showed no need for further changes to the cross-section.

During the development of the joint geometry, one of the key findings was that there were specific limitations that could have made the geometry significantly larger, thus affecting the structural response significantly due to its cumulative weight. The joint was optimised in a way to reduce the material as much as possible. The relative connection parts needed to have specific geometry matching the market availability. The final joint geometry consumed a significant percentage of 13% of the structure, while the application of double-member SLEs has increased the overall weight of the members by another 10% comparing to relative studies of structures with single-member SLEs.

Finally, the numerical simulation of the joint with the members showed an unexpected early onset of bearing stress at the joint and member thread holes. While the extreme loading applied to the assembly drove both joint and polar elements to reach their yield strength, the translational elements did not experience yielding during the loading process. The premature bearing stress at the thread holes limits the load capacity of the assembly.

9.2 Recommendations for future research

The main future research that would be incredibly useful for deployable structure applications is the development of a universal joint for double-member SLE applications. This means that this joint would not be dependent on the geometry of the cross sections and would rather be applicable to a variety of cross sections. By developing such a joint, the application of it in scissor-type deployable structures will become very practical. In terms of investigating more of the current geometry of the joint, it would be very interesting to implement this geometry into the finite element model of the whole structure, thus exploring its response and behaviour. Another suggestion is the investigation of the deployment phases and the analysis of the structure under deployment loads in various situations.

10 REFERENCES

[1] Gantes C.J. (2001), Deployable Structures: Analysis and Design, Southampton, Boston: WIT Press.

[2] Walmart Inc. (2026). [Online]. Available: https://www.walmart.com/ip/Efavormart-Expandable-Lattice-Fence-Artificial-Ivy-Trellis-Privacy-Hedge-Backdrop-Accordion-Fencing-17-H-X-95-L-Ideal-Garden-Patio-Balcony-Deck-Backy/609184587.

[3] Roovers K. (2017), "Deployable Scissor Grids. Geometry and Kinematics", PhD Thesis, Brussels: Vrije Universiteit.

[4] Roovers K. and De Temmerman N. (2017), "Deployable scissor grids consisting of translational units," International Journal of Solids and Structures, vol. 121, pp. 45-61.

[5] Escrig F., Perez Valcarcel J., Sanchez J. (1996), "Deployable cover on a swimming pool in Seville," Journal of the International Association for Shell and Spatial Structures, vol. 37, pp. 39-70.

[6] "www.pro-tent.com," Pro-Tent Switzerland, [Online]. Available: https://www.pro-tent.com/application-areas/racing-tent/.

[7] "www.drewexmachina.com," Drew ex machina, [Online]. Available: https://www.drewexmachina.com/2024/08/14/first-pictures-view-of-the-earth-from-nasas-explorer-6-august-14-1959.

[8] "www.ntrs.nasa.gov," National Administration of Space and Aeronautics, [Online]. Available: https://ntrs.nasa.gov/citations/19750053963.

[9] "www.science.jpl.nasa.gov," Jet Propulsion Laboratory, [Online]. Available: https://science.jpl.nasa.gov/projects/srtm/.

[10] Duan B., Zhang y., Du J. (2020), "Introduction. In: Large Deployable Satellite Antennas," in Large Deployable Satellite Antennas, Singapore, Springer, pp. 1-33.

[11] "www.jpl.nasa.gov," Jet Propulsion Laboratory, 13 June 2012. [Online]. Available: https://www.jpl.nasa.gov/missions/nuclear-spectroscopic-telescope-array-nustar/.

[12] "www.science.nasa.gov," National Aeronautics and Space Administration, [Online]. Available: https://science.nasa.gov/mission/webb/deployment/#Unfolding-Webb.

[13] Pantazis G. (2025), "Report, drawings and 3D printed prototypes WP5 Case Study: 3D printing and testing of scaled prototype deployable shelter," ADDOPTML, Optimized 3D printed structures, Athens.

[14] Gantes C., Connor J. J., Logcher R. D. (1993), "Simple Friction Model for Scissor-Type Mobile Structures," Journal of Engineering Mechanics, vol. 119, no. 3.

[15] Pantazis G. (2022), "Design of Deployable Shelters for Emergency Response," Diploma Thesis ΕΜΚ ΔΕ 8.

[16] EN 1990 (2002), Eurocode - Basis of structural design, European Committee for Standardization.

[17] EN 1991 (2002), Eurocode 1 - Actions on structures, European Committee for Standardization.

[18] Koumar A. (2016), Deployable Scissor Structures for Disaster Relief: Multi – Criteria . PhD Thesis, Vrije Universiteit Brussel: Brussels.

[19] Pellegrino S. (2001), "Matrices for Deployable Structures," in Deployable Structures, Vienna, Springer-Verlag, pp. 174-178.

[20] Dlubal Software GmbH (2026), "RFEM 6 – Finite Element Analysis Software," Dlubal Software GmbH, Tiefenbach, Germany.

[21] EN 1993 (2022), Eurocode 3 – Design of steel structures, European Committee for Standardization.

[22] Bathe K. J. (1996), Finite Element Procedures, New Jersey: Prentice Hall.

[23] EN 1999 (2021), "Eurocode 9 – Design of aluninium structures", European Committee for Standardization.

[24] DIN 933 (1989), Sechskantschrauben mit Gewinde bis Kopf, Deutsches Institut für Normung.

[25] DIN 6916 (1989), "Round washers for high – strength structural steel bolting", Deutsches Institut für Normung.

[26] DIN 6915 (1989), "High – strength hexagon nuts with large widths across flats for, Deutsches Institut für Normung.

[27] ABAQUS (2021), Analysis User's Manual, Version 6.6., Dassault Systemes Simulia, Inc.

[28] Fragiadakis M. (2020), Nonlinear Analysis of Frame Structures under Seismic Loading, Athens: Class notes, National Technical University of Athens.

[29] Pantazis G. (2025), Report, drawings and 3D printed prototypes WP5 Case Study: 3D printing and testing of scaled prototype deployable shelter, WP5 Report – D5.2.

[30] EN 755 (1998), Aluminium and aluminium alloys – Extruded rod/bar, tube and profiles Part 7: Seamless tubes, tolerances on dimensions and form, European Committee for Standardization.